

Υ production at $\sqrt{s_{NN}} = 200$ GeV in p+p and Au+Au collisions at STAR

By

Rosi J Reed

B.S. (San Jose State University) 2005

M.S. (University of California at Davis) 2008

DISSERTATION

Submitted in partial satisfaction of the requirements for the degree of

DOCTOR OF PHILOSOPHY

in

Physics

in the

OFFICE OF GRADUATE STUDIES

of the

UNIVERSITY OF CALIFORNIA,

DAVIS

Approved:

Manuel Calderón de la Barca Sánchez, Chair

Daniel Cebra

Ramona Vogt

Committee in Charge

2011

Abstract

Υ production at $\sqrt{s_{NN}} = 200$ GeV in p+p and Au+Au collisions at STAR

by

Rosi J. Reed

Quarkonia suppression, caused by the Debye screening of the Quantum Chromo-Dynamic (QCD) potential between the two heavy quarks, was originally claimed to be an unambiguous signal of the formation of a Quark-Gluon Plasma (QGP) [1]. J/ψ suppression has been observed in heavy ion collisions at both SPS and RHIC, however, the magnitude of the suppression in both systems was similar despite the differing energy densities [2]. This indicates that Quarkonia suppression isn't as unambiguous a signal as previously supposed because there are many competing processes that affect the yield of quarkonia in heavy ion collisions. Some of these effects enhance the quarkonia yield, such as the statistical recombination of the $Q\bar{Q}$ pairs, while others reduce it, such as co-mover absorption [3]. These processes affect the Υ family less than the J/ψ family at 200 GeV, and it is believed that color screening should be the dominant process that contributes to any observed suppression of the Υ . In order to measure the suppression of the Υ , it was necessary to measure the cross section of the bottomonia states in $p + p$. This was measured to be 114 ± 38 (stat. + fit) $^{+23}_{-24}$ (sys.) pb [4]. The same trigger algorithm and experimental procedures developed for this measurement were applied to the Au+Au measurement, with the

exception of a slight increase in trigger thresholds. This algorithm was applied to 4 Million triggered events taken during run 7 (2007) and combined with the $p + p$ cross section, an $R_{AA}(0-60\%)$ of $0.80 \pm 0.34(\text{stat.})$ was calculated. The mass resolution was improved with the removal of the SVT and its support structure from the center of STAR. A modified trigger algorithm was applied to 50 Millions triggers taken during run 10 (2010) and this yielded an $R_{AA}(0-60\%)$ of $0.55 \pm 0.23(\text{stat.})_{-0.13}^{+0.07}(\text{sys.})$ when combined with the $p + p$ cross section.

I would like to dedicate this thesis to my husband, Ed.

Acknowledgements

First and foremost, I want to thank my husband, Ed, who supported me as I followed my dream, brought me food while I was working and put up with me when I was stressed. Without him, this would not be possible.

I also want to thank Manuel Calderón de la Barca Sánchez for interesting me in the field of Heavy Ion collisions, answering all of my questions and for his general enthusiasm and inspiration. I would also like to thank Daniel Cebra for his support and for pushing me to think for myself. I'd like to thank Sevil Salur for the many discussions we've had, as well as for the endless supply of chocolate.

I want to thank my parents for raising me to believe that anything I want to do, I can do and for instilling in me a great love of mathematics and science at an early age.

I would like to thank Patrick Hamill and Alejandro Garcia for making physics fun while I was a young and distracted undergraduate. And of course, I also have to extend my thanks to Michael Kaufman for introducing me to research!

Contents

List of Figures	viii
List of Tables	xvi
1 Introduction	1
1.1 Quark-Gluon Plasma	8
1.1.1 QGP Signatures	10
1.1.2 Heavy-Ion Collisions	16
2 Quarkonia	26
2.1 Production	27
2.2 Color Singlet Model	28
2.3 NRQCD	29
2.4 Color Evaporation Model	31
2.5 Cold Nuclear Matter Effects	32
2.6 Quarkonia in Heavy Ion Collisions	34
2.7 $\Upsilon(1S + 2S + 3S)$ Family as a probe	40
3 Experimental Facilities	42
3.1 STAR	42
3.2 Beam-Beam Counter	43
3.3 Vertex Position Detector	44
3.4 Barrel Electromagnetic Calorimeter	44
3.5 Time Projection Chamber	46
3.5.1 Track Reconstruction	48
3.5.2 Vertex Reconstruction	49
4 Υ in p+p collisions at $\sqrt{s} = 200$ GeV	51
4.1 Data Set and QA	51
4.2 STAR Υ Trigger	52
4.2.1 Υ L2 Trigger	54
4.2.2 Trigger Performance	57
4.2.3 Υ Acceptance and Trigger Efficiency	62

4.3	Υ Analysis	67
4.3.1	Track Selection	67
4.3.2	PID	69
5	Υ in Au+Au at 200 GeV	75
5.1	Analysis of 2007 Data	76
5.1.1	Glauber Model	77
5.1.2	PID	81
5.1.3	Υ Reconstruction Efficiency	84
5.1.4	R_{AA}	86
5.2	Analysis of 2010 Data	87
5.2.1	PID	89
5.2.2	Υ Reconstruction Efficiency	95
5.2.3	Centrality Selection	97
6	Results	99
6.1	Results for Υ in $p + p$	99
6.1.1	Υ Line-Shape in p - p collisions	100
6.1.2	Υ yield and cross-section	105
6.2	Υ in Au+Au: Results from 2007	114
6.2.1	Line-Shape	114
6.2.2	Υ yield	117
6.3	Υ in Au+Au: Results from 2010	122
6.3.1	Υ yield and R_{AA}	122
6.3.2	Systematics	125
7	Discussion	136
7.1	Experiment	136
7.2	Theory	144
8	Conclusion	150
8.1	Υ cross-section	150
8.2	ΥR_{AA}	151
	Bibliography	152

List of Figures

1.1	The elementary particles of the Standard Model [5].	2
1.2	Measurements of the QCD coupling constant, α_s versus energy. The value of $\alpha_s(M_Z)$ is the world average for α_s at the mass of the Z^0 [6].	6
1.3	The relationship between the strong coupling constant $\alpha_s(\alpha_{qq}(r, T))$ vs r at different temperatures [7]. The thin black line is α_s at a temperature of zero. The thick black line and dashed lines are the results from a pure gauge theory. For further details, see Reference [7].	8
1.4	The QCD Phase diagram [8]. This shows the relationship between the QGP, and hadronic states of nuclear matter. It is currently believed that at high μ_B and low temperature, the phase transition is first order, and at low μ_B the phase transition is a crossover. A critical point should exist between the two transitions. However, at the time of this writing, this has not been experimentally verified.	12
1.5	Degrees of freedom versus temperature from a Lattice QCD calculation given in reference [9]. The arrows indicate the ideal gas values. . . .	13
1.6	Elliptic flow predictions for various particle species versus p_T [10]. . .	13
1.7	Comparison of the experimental data on different particle ratios measured at RHIC at $\sqrt{s_{NN}} = 130$ and 200 GeV with statistical model calculations. [11].	14
1.8	The picture on the left is a cartoon of two heavy ions prior to their collision with impact parameter b . The picture on the right shows what may occur after the collision, with some particle production coming from those nucleons that participated in the collision and some spectator nucleons continuing on after the collision. [12]	15
1.9	Picture of a peripheral collision, with the initial spatial anisotropy shown in red and the spectators in blue. [12]	17
1.10	Number of quark (n_q) scaled v_2 as a function of scaled p_T . Once we scale the baryons and the mesons, they fall on the same curve, indicating that the flow originated prior to hadronization. [13]	19
1.11	Nuclear modification factors of γ, π^0 , and η in central Au-Au collisions at $\sqrt{s_{NN}} = 200$ GeV from reference [13]	20

1.12	Dihadron azimuthal correlations from reference [14]. In black is the reference $p + p$ result, in red is the d+Au result and in blue is the central Au+Au result.	23
1.13	The top graph is a PHENIX measure of the R_{AA} of electrons from heavy flavor decays in blue. In open circles the R_{AA} of the π^0 is shown again. The lines are from model calculations. The lower graph is the v_2 for the same particle species. Note that these are not scaled by n_q , the interesting result here is simply that the heavy mesons seems to flow. This graphs come from reference [15].	25
2.1	The top graph is a comparison of the PHENIX J/ψ results multiplied by an estimate of the fraction that are direct compared to the CSM at LO, NLO and NLO+ cg fusion model. The cg stands for the fusion of a gluon with an intrinsic charm quark in the nucleon sea. The lower graph shows the PHENIX Υ results and the STAR Υ results (that will be discussed in Chapter 4 of this thesis) also multiplied by an estimate of the percentage that come from direct production. These are compared to LO and NLO CSM calculations. These graphs come from Ref. [16].	29
2.2	Results for $\Upsilon + X$ at LO, full NLO and for NNLO* compared to results from $\sqrt{s} = 1.8$ TeV measured by CDF. This calculation comes from Reference [17]. The theoretical uncertainty comes from uncertainties in the choice of scale and the mass of the b quark. See the Reference for further details.	30
2.3	This is the EPS09 gluon-shadowing parameterization at $Q = m_b$ versus $\log_{10} x$. The shaded bands are the uncertainty in the calculation. At $\sqrt{s_{NN}} = 200$ GeV, the shadowing results are consistent with 1 for the Υ as the Feynman x region for Υ production is ~ 0.05 (or $\log_{10} x = -1.3$), though it's possible that this measurement could be in the anti-shadowing region. See reference [18].	33
2.4	The graph on the left shows the bottomonium spectral functions if only the real part of the potential is used. On the right the is the spectral function if both the real and imaginary part of the potential are used [19].	37
2.5	Measured J/ψ production yields shown as a function of the collisional energy density. These yields are normalized to the expected yield assuming the only source of suppression is the ordinary absorption by the nuclear medium. The expected yield was determined by proton-ion collisions [2].	37
2.6	J/ψ R_{AA} versus the number of participants at mid-rapidity for the SPS and RHIC energies. Despite the differing energies, the nuclear modification factors appear to be the same for all data sets [20]. . .	38
2.7	This shows the spectrum and transitions of the bottomonium family with masses below the $B\bar{B}$ threshold [21].	40

3.1	Schematic of STAR's BBC East and BBC West. [22]	43
3.2	STAR's BEMC shown with the magnet and the TPC. The SVT in the center was removed after 2007. [23]	45
3.3	STAR TPC shown with a person for comparison [24]. The high voltage membrane is the plane that defines $z = 0$	48
3.4	One TPC sector[24], of which there are 24. This schematic shows the differing schemes for the inner section and outer section.	48
4.1	The p_T distribution for simulated Υ daughter electrons in filled circles and positrons in open squares, with the highest p_T . Only those daughters with a parent Υ which falls in the STAR BEMC geometrical acceptance are shown. The solid histogram is the sum of the two distributions [4].	54
4.2	The L0 DSM-ADC distribution for simulated Υ daughter electrons (filled circle) or positrons (open square) with the highest ADC. The histogram is the sum. The threshold for Trigger II is shown as a vertical dotted line. [4].	55
4.3	Trigger scheme.	57
4.4	The L0 DSM-ADC distribution for the highest BEMC tower of a candidate pair, the same as the black histogram shown in 4.2. We show Trigger I data after applying Trigger II thresholds (red circles) to the data, and Trigger II data (black squares). All yields are normalized by the integrated luminosity. The blue histograms are the distributions of the daughters from simulated $\Upsilon(1S)$ that have passed acceptance. The dotted line has the additional requirement that it has passed both L0 trigger requirements. The simulation histograms are normalized assuming $BR \times d\sigma/dy=100$ pb times a factor of 500. The threshold for Trigger II is shown as a vertical solid line. [4].	58
4.5	The L2 Cluster-1 energy distribution (EL21) for all towers above the HT threshold in a trigger patch above the TP threshold. The L2 trigger requires $EL21 \geq 4.0$ GeV. The solid-line histogram shows the accepted Upsilon (from simulation) after acceptance requirements, while the spectrum shown by the dashed-line includes all trigger requirements. Normalization and scaling factors are done as for Fig. 3.[4].	60
4.6	The L2 invariant mass M_{L2}^{12} distribution for accepted events. The histogram shows the M_{L2}^{12} distribution for simulated $\Upsilon(1S)$ s after acceptance, L0 trigger, L2 cluster and L2 opening angle selection on the e^+e^- daughters. Vertical lines show location of the trigger thresholds. Normalization and scaling factors are done as for Fig. 3 [4].	61
4.7	The cosine of the L2 opening angle $L212$ distribution for accepted events. The histogram shows the distribution for simulated Upsilon after acceptance, L0 trigger and L2 Cluster selection. The vertical line shows the location of the trigger threshold. Normalization and scaling factors are done as for Fig. 3. [4].	62

4.8	Combined acceptance efficiency as a function of rapidity y_{Upsilon} for the decay $\text{Upsilon} \rightarrow e^+e^-$ in STAR. Circles: BEMC acceptance only; squares: adding L0 requirement; upright triangles: adding L2 requirement; down triangles: adding TPC acceptance+TPC tracking cuts and TPC-BEMC matching. [4].	63
4.9	The line histogram shows the η - ϕ radial distance $R = \sqrt{\Delta\eta^2 + \Delta\phi^2}$ between the TPC track and the 3-tower BEMC electron cluster for simulated Upsilon daughters. The black squares show this distribution from data. We reject candidate tracks with $R > 0.04$ [4].	68
4.10	The E/p distribution for reconstructed positrons from simulated Upsilon decays is the dashed line. Positrons selected from Upsilon triggered data events selected using dE/dx are the red points. The solid line is simulated $\pi^0 \rightarrow \gamma\gamma \rightarrow e^+e^-$ R/p . The dot-dashed line is a fit to the data using a combination of the two simulated distributions [4].	71
5.1	The reconstructed V_z distribution for the highest ranked vertex in those events that satisfied the 2007 Upsilon trigger. The dotted lines indicate the VPD V_z window for this data set.	76
5.2	Reference multiplicity for 4 categories of events. In black is the reference multiplicity associated with the highest ranked vertex from the Upsilon minimum-bias trigger. In red is the multiplicity generated from the Glauber model calculation explained in Section 5.1.1. This distribution had a parameter, k , chosen so that it matched the minimum-bias distribution from $\text{RefMult} > 100$. Below that, the inefficiency of triggering on these low multiplicity events can be seen. The purple curve is the reference multiplicity from the highest ranked vertex from Upsilon triggered events. It is biased towards central events, with the low reference multiplicity tail coming from those events where the vertexer ranked an out-of-time pile-up vertex ahead of the proper vertex. In blue is the reference multiplicity for those events that had a track associated with each L2 energy cluster.	79
5.3	The distribution, $n\sigma_{\text{electron}}$, a normalized distribution of electron dE/dx for tracks with $6.0 < p < 7.0$ which extrapolate to a trigger cluster. This distribution is simultaneously fit with three gaussians to determine the mean of the electron distribution.	82
5.4	The means (labeled as μ) of $n\sigma_{\text{electron}}$ versus momentum for tracks which extrapolate to trigger clusters.	83
5.5	The three-cluster energy over the momentum for TPC tracks which extrapolate to a trigger cluster. This distribution is calculated from those tracks with $6 < p < 7$ and has the same width as the distribution calculated in the baseline p+p measurement.	84

5.6	Efficiency versus refMult from the 2007 Υ embedding with the 2007 Υ trigger conditions applied. The efficiency appears to be flat versus centrality as the decreased tracking efficiency in the most central events is balanced by the increased trigger efficiency due to the underlying event increasing the probability that a trigger will fire for a given Υ	85
5.7	The number of towers satisfying the L0 trigger requirement for the 2010 data set.	88
5.8	The 3 tower energy cluster formed for those towers that met the L0 trigger requirement. The red dotted line indicates the online energy value for the adc of 18.	89
5.9	The single tower energy for secondary tracks that are in HT trigger events with a requirement that the energy in the tower based on the offline calibration be greater than 0. The tracks had a loose selection on the normalized ionization energy loss of $-2 < n\sigma_{electron} < 3$ in order to remove some of the pion background.	90
5.10	In solid is the distribution for opposite sign track pairs and in the red dotted line for same sign pairs with $ 1 - E/p < 3$ and $-2 < n\sigma_{electron} < 3$. The kinematic peak is far removed from our region of interest of $7 < M_{ee} < 12 \text{ GeV}/c^2$	91
5.11	E/p distributions for the two Υ candidate daughters. In black is the distribution using the three tower cluster associated with the L0 trigger tower. In red is the single tower value for the secondary daughter. The dotted lines are the offline analysis cuts used to select electrons.	92
5.12	E/p versus E for the triggered daughters on the left and the secondary daughters on the right.	92
5.13	The kinematic distributions of the two different electron embedding data sets. In red is the monte carlo distribution from the electrons coming from $\Upsilon(1S)$ as embedded into the 2007 geometry. In black is the distribution from the monte carlo distribution of the electrons embedded into the 2010 geometry.	93
5.14	The difference between the MC and reconstructed momentum versus the MC momentum for electrons which were accepted, reconstructed and passed the track quality cuts.	93
5.15	The difference between the MC and reconstructed momentum for electrons which were accepted, reconstructed and met the track quality cuts. In black is the distribution coming from $\Upsilon(1S) \rightarrow e^+e^-$ embedded into the 2007 geometry. In red is the pure electron sample, weighted by the expected momentum distribution from Υ decays, embedded into the 2010 geometry.	94
5.16	Reconstructed track efficiency for 2007 versus 2010 embedding samples. Black is the sample from the single electron sample from 2010, with the proper kinematic weighting for the Υ kinematics folded in and red is the $\Upsilon(1S)$ 2007 sample.	95

6.1	The invariant mass spectrum for the like-sign in red and the unlike-sign in blue from the Υ triggered data set in $p + p$. The black dotted line is a fit to the like-sign distribution explained in the text.	100
6.2	The correlation between the Drell-Yan and $b\bar{b}$ continuum cross-sections in the phase space region of $ y < 0.5$ and $8 < m_{ee} < 11$ GeV/ c^2 at the 1σ and 2σ level. The prediction from an NLO calculation of the Drell-Yan cross section [25] is shown as the vertical line at 38.6 pb.	104
6.3	The blue data points are the result from subtracting the like-sign yield in Figure 6.1 from the unlike-sign on a bin-by-bin basis. The error bars on these points are statistical only. The solid red curve is the parameterization of the $\Upsilon(1S + 2S + 3S)$ states plus the contribution from the Drell-Yan and $b\bar{b}$ continuum as described in the text. The dashed red histogram is the integral of the fit function in each bin. The black dot-dashed line is the total of the Drell-Yan and $b\bar{b}$ continuum.	106
6.4	The STAR measurement of the $\Upsilon(1S + 2S + 3S)_{ y < 0.5}$ cross-section times branching ratio into electrons. The error bars are statistical, the shaded box shows the systematic uncertainty with the scale given by left axis. The raw Υ yield vs. y is shown by the histogram at the bottom, with scale on the right axis. The cross-section was calculated from the yield between the vertical dot-dashed lines. The open squares are from a NLO CEM calculation, and the area between the dotted lines is the prediction from a NLO CSM calculation of the Υ cross-section (see text).	112
6.5	Measurements of the $\Upsilon(1S + 2S + 3S)$ cross-section versus center-of-mass energy for the world data compared to a NLO CEM calculation. The error bars on the STAR point are statistical and the box is systematic.	113
6.6	The number of towers that satisfied the L0 trigger condition for the 2007 Au+Au Υ trigger is in black. The number that satisfy the L2 trigger condition are in red. Every event has at least 1 tower that satisfies the L0 condition, and at least 2 that satisfy the L2 trigger condition since every tower that satisfies L0 also satisfies L2.	114
6.7	The unlike-sign di-electron spectrum for 0-60% central events is shown as the blue circles. The sum of the like-sign spectra is shown as the red histogram. The solid line is a fit to the like-sign background. . . .	115
6.8	The unlike-sign subtracted background for 0-60% central events. . . .	116
6.9	The unlike-sign di-electron spectrum for 0-10% central events is shown as the blue circles. The sum of the like-sign spectrums is shown as the red histogram. The solid line is a fit to the like-sign background. . . .	117
6.10	The unlike-sign subtracted background for 0-10% central events. . . .	118
6.11	The di-electron spectrum from 0-60% fit with the assumption that there was no Υ 's in this data-set. The fit had a χ^2/DOF of 5.6, indicating this scenario is unlikely.	119

6.12	The correlation between the raw $\Upsilon(1S + 2S + 3S)$ yield and the raw Drell-Yan and $b\bar{b}$ yield in 0-60% centrality from the 2007 data-set. The Υ yield is calculated directly from the fit.	120
6.13	The like-sign spectrum as shown in Figure 6.8 fit with a functional form that had two free-parameters, the total yield of the $\Upsilon(1S + 2S + 3S)$ and the total yield of the Drell-Yan and $b\bar{b}$ continuum.	121
6.14	The like-sign spectrum as shown in Figure 6.10 fit with a functional form that had two free-parameters, the total yield of the $\Upsilon(1S + 2S + 3S)$ and the total yield of the Drell-Yan and $b\bar{b}$ continuum.	122
6.15	This is Figure 6.12 with the additional bands showing what we would expect for the yields of the $\Upsilon(1S + 2S + 3S)$ and the Drell-Yan and $b\bar{b}$ background if we simply scaled the $p + p$ results from Chapter 3 by N_{bin} . This shows that we are consistent with an $R_{AA}^{\Upsilon+DY+b\bar{b}} = 1$. However the uncertainty is large enough that almost any suppression model is not excluded.	124
6.16	Shown here is the R_{AA} from the 2007 data set. The error bars are statistical only. The point on the right for 0-10% centrality is a subset of the point for 0-60% centrality.	125
6.17	The unlike-sign di-electron spectrum for 0-60% central events is shown as the blue circles. The sum of the like-sign spectra is shown as the red histogram.	126
6.18	The unlike-sign di-electron spectrum for 0-10% central events is shown as the blue circles. The sum of the like-sign spectra is shown as the red histogram.	127
6.19	The unlike-sign di-electron spectrum for 10-30% central events is shown as the blue circles. The sum of the like-sign spectra is shown as the red histogram.	128
6.20	The unlike-sign di-electron spectrum for 30-60% central events is shown as the blue circles. The sum of the like-sign spectra is shown as the red histogram.	129
6.21	The unlike-sign subtracted di-electron spectrum for 0-60% central events is shown with the line-shape fit.	130
6.22	The unlike-sign subtracted di-electron spectrum for 0-10% central events is shown with the line-shape fit.	132
6.23	The unlike-sign subtracted di-electron spectrum for 10-30% central events is shown with the line-shape fit.	133
6.24	The unlike-sign subtracted di-electron spectrum for 30-60% central events is shown with the line-shape fit.	134

6.25	R_{AA} for $\Upsilon(1S + 2S + 3S)_{ y <0.5}$ versus centrality. The solid black points are the Υ results from Tabletab:RAA2010. The red solid square is the value for 0-60% centrality from Section 6.2. The solid blue box is the systematic uncertainty from the p+p cross-section, resulting from the uncertainty in the luminosity and the trigger efficiency. The grey boxes around the three Υ points are the systematic uncertainties of those points resulting from the uncertainty in N_{bin} and the $\Upsilon(1S + 2S + 3S)$ line-shape. The red dotted line is the ratio of the total cross-section of $\Upsilon(1S)/\Upsilon(1S + 2S + 3S)$. The purple dashed line is the ratio of only the direct $\Upsilon(1S)$ cross-section over the total $\Upsilon(1S + 2S + 3S)$ cross-section.	135
7.1	The points are from Figure 6.25. They are fit with a constant, in dashed red, and a linear function, in dotted purple.	139
7.2	The red square is the 0-60% R_{AA} for $\Upsilon(1S + 2S + 3S)_{ y <0.5} \rightarrow e^+e^-$ from the 2007 run, the blue triangle is the same point from the 2010 run. The purple line shows the 0-100% $R_{AA}^{\Upsilon(1S + 2S + 3S)_{+DY+b\bar{b}}}$ for the $\Upsilon(1S + 2S + 3S)_{ y <0.35} \rightarrow e^+e^-$ result from PHENIX run 2007 at 90% CL [26].	140
7.3	CMS R_{AA} results for inclusive $\Upsilon(1S)$ and the prompt and non-prompt J/ψ . The solid points are a subset of the open points [27]. The decay used to reconstruct them is $\Upsilon(J/\psi) \rightarrow \mu^+\mu^-$ and $ y_\Upsilon < 2.4$	142
7.4	CMS R_{AA} results [27] in green triangles. The STAR results from 2010 are in black. The blue boxes are the $p + p$ normalization for the STAR point, the solid green box is the $p + p$ normalization for the CMS points. The red small dashed lines indicate an estimate for the CMS $R_{AA}^{\Upsilon(1S + 2S + 3S)}$ result given Equation 7.1. The large purple dashed line indicates an estimate for $R_{AA}^{\Upsilon(1S + 2S + 3S)}$ if only the $\Upsilon(1S)$ state survives, based on the relative cross sections of the direct and indirect Υ 's	143
7.5	The blue dashed line is a calculation from [28] assuming a central temperature of $T_0 = 504$ MeV. The black points are our $\Upsilon(1S + 2S + 3S)$ analysis from 2010.	146
7.6	This is the case where the potential was set to the internal energy ($V = U$). The blue dot-dashed line is the calculation for the directly $\Upsilon(1S)$. The red dashed line is the R_{AA} for the total $\Upsilon(1S)$. And the green dot-dashed line is the R_{AA} for the direct $\Upsilon(2S)$ [29]. Our 2010 points are in black.	147
7.7	This is the case where the potential was set to the Free energy ($V = F$). The blue dot-dashed line is the calculation for the directly $\Upsilon(1S)$. The red dashed line is the R_{AA} for the total $\Upsilon(1S)$. And the green dot-dashed line is the R_{AA} for the direct $\Upsilon(2S)$ [29]. Our 2010 points are in black..	148

List of Tables

4.1	Acceptance, trigger efficiency, and tracking efficiency for reconstructing $\Upsilon \rightarrow e^+e^-$ in STAR in the kinematic region $ y_\Upsilon < 0.5$. The first 4 rows are for the 1S and the last row is for the cross section-weighted 1S+2S+3S combination. All systematic uncertainties are listed in Table 6.1.2.	65
4.2	Branching fractions for $\Upsilon(nS) \rightarrow e^+e^-$ [30] and total cross sections at $\sqrt{s} = 200$ GeV from an NLO CEM model [31].	66
5.1	L0 and L2 parameters for the 2007 STAR Υ trigger	77
5.2	Efficiency from 2007 Υ embedding with 2007 Υ trigger conditions applied.	86
5.3	Efficiency from 2010.	97
5.4	Centrality cuts and uncertainties	98
6.1	Extraction of $\Upsilon(1S+2S+3S)$ yield by bin counting and fitting. The sums are done in the range $8 < m < 11$ GeV/ c^2	107
6.2	Systematic uncertainties on the measurement of the Υ cross section.	111
6.3	The results in this table are from the the 2007 run. Total number of counts in the unlike-sign (N_{+-}), like-sign positive (N_{++}), and like-sign negative (N_{--}) di-electron invariant mass distributions in the region between $8 < m < 12$ GeV/ c^2 . The background, B , is calculated as the sum of the two like-sign distributions and the signal, S , is the background subtracted unlike-sign distribution. The distributions for this numbers are shown in Figure 6.7–6.10. The $\Upsilon(1S + 2S + 3S)$ yield as extracted by the fits shown in Figures 6.13 and 6.14 are also shown.	123
6.4	The results in this table are from the the 2010 run. Total number of counts in the unlike-sign (N_{+-}), like-sign positive (N_{++}), and like-sign negative (N_{--}) di-electron invariant mass distributions in the region between $8 < m < 12$ GeV/ c^2 . The background, B , is calculated as the sum of the two like-sign distributions and the signal, S , is the background subtracted unlike-sign distribution. The significance is the significance of the signal, S , which is the sum of the $\Upsilon(1S + 2S + 3S)$ and the Drell-Yan and $b\bar{b}$ continuum yields.	123

6.5	Systematics for the 2010 analysis. The first row is the total Υ yield if we assume that only the $\Upsilon(1S)$ survives. The second row is the percent uncertainty of this effect and including the 5% difference in the efficiency. The third row is the percent uncertainty due to N_{bin}	131
6.6	The first four rows of each centrality are all the values need to calculate R_{AA} . The fifth row is the calculation of R_{AA} given these values, only using the uncertainty from the Au+Au analysis. Since the $p + p$ uncertainties apply to all points, it is useful to break them out separately. The sixth row has the $p + p$ uncertainties added in quadrature. The results are displayed in Figure 6.25	131
7.1	Quarkonium Dissociation Temperature relative to T_c [20].	137
7.2	Branching ratios of the $\Upsilon(nS) \rightarrow e^+e^-$ [30] and the total cross sections from a NLO CEM model [32].	141
7.3	144

Chapter 1

Introduction

At its most basic, the field of physics is a study of how the universe works. Our current understanding is that all interactions are governed by four forces: the Electromagnetic force, the Weak force, the Strong force and Gravity. It is also understood that all matter is formed from just a few elementary particles. Three of the forces, the Strong force, the Weak force and the Electromagnetic force, have been combined into a single theory, the Standard Model. The modern formalism of the electromagnetic force is called Quantum Electrodynamics (QED) and that of the strong force is Quantum Chromodynamics (QCD). Much effort has been made to create a single theory that combines the Standard Model with gravity into a Theory of Everything (TOE). However, this has not yet happened, and may not be possible.

All elementary particles can be divided into two groups: fermions and bosons. Bosons have integer spin, while fermions have spins that are multiples of $\frac{1}{2}$. The spin-statistics theorem formulated by Wolfgang Pauli states that the wave function of a system of bosons remains the same if the positions of any two particles are

Three Generations of Matter (Fermions)				
	I	II	III	
mass→	2.4 MeV	1.27 GeV	171.2 GeV	0
charge→	$\frac{2}{3}$	$\frac{2}{3}$	$\frac{2}{3}$	0
spin→	$\frac{1}{2}$	$\frac{1}{2}$	$\frac{1}{2}$	1
name→	u up	c charm	t top	γ photon
Quarks	4.8 MeV $-\frac{1}{3}$ d down	104 MeV $-\frac{1}{3}$ s strange	4.2 GeV $-\frac{1}{3}$ b bottom	0 0 1 g gluon
	<2.2 eV 0 $\frac{1}{2}$ ν_e electron neutrino	<0.17 MeV 0 $\frac{1}{2}$ ν_μ muon neutrino	<15.5 MeV 0 $\frac{1}{2}$ ν_τ tau neutrino	91.2 GeV 0 1 Z^0 weak force
	0.511 MeV -1 $\frac{1}{2}$ e electron	105.7 MeV -1 $\frac{1}{2}$ μ muon	1.777 GeV -1 $\frac{1}{2}$ τ tau	80.4 GeV ± 1 1 W^\pm weak force
Leptons				Bosons (Forces)

Figure 1.1. The elementary particles of the Standard Model [5].

swapped. The wave-function of a system of fermions will change sign if two fermions are swapped. This leads to the Pauli exclusion principle, which states that two identical fermions cannot have the same quantum numbers. The fundamental fermions include the leptons: $e^{-(+)}$, $\mu^{-(+)}$, $\tau^{-(+)}$ and their associated neutrinos. This group also contains the quarks: up (u), down (d), strange (s), charm (c), bottom (b) and top (t). The group of fundamental bosons is made up of all of the force carriers, which includes the photon (γ), $W^{+(-)}$, Z^0 , gluons (g) and the as yet undiscovered Higgs.

All these Standard Model particles are shown in Figure 1.1.

The electromagnetic force was first put into a modern formalism in 1873 by James Maxwell when he unified the electric and magnetic force in his paper *Treatise on Electricity and Magnetism* [33]. This force is the most familiar of the three fundamental forces in the Standard Model as it governs most of the interactions observed in every day experiences. Any charged particle can interact via the electromagnetic force by an exchange of photons. However, since the photon has no electromagnetic charge, it cannot interact with itself. This simplifies calculations of electromagnetic interactions. Also, the coupling constant that governs the strength of the electromagnetic interaction is small, $\alpha = 1/137$, which allows calculations to be done perturbatively.

The weak force is more complicated than the electromagnetic force as it is carried by the heavy bosons Z^0 , W^+ and W^- . It was given the label “weak” because the field strength for the weak force was 10^{-11} times that of the electromagnetic force. The weak force is interesting because it allows the flavor of a quark to change by interacting with a $W^{+(-)}$. However, it appears that interactions that change flavor by emitting a Z^0 are not possible as they have not been observed. The weak force was eventually unified with the electromagnetic force into a single force called the electroweak force [34, 35, 36].

The strong force was first hypothesized to exist after the discovery that the center of an atom is made up exclusively of positively charged and neutral particles. Another force was required to overcome the Coulombic repulsion of these positively-charged particles. This force had to have a short range, roughly 1 fm, the same size as a nucleon, as the size of the nucleons naturally sets the distance over which this force

can interact. A pattern was observed in the masses and charges of various particles discovered in the mid-20th century. This pattern was explained by Murray Gell-Mann in the quark model, which hypothesized that hadrons such as the proton or neutron were not fundamental particles [37]. Rather they were made up of fermions, called quarks. Quarks had spin $\frac{1}{2}$ and could have an electromagnetic charge of either $+\frac{2}{3}$ or $-\frac{1}{3}$. The quark model required the addition of another quantum number besides spin and charge to describe the quarks within a hadron because the Pauli Exclusion Principle would be violated by the spin $\frac{3}{2}$ Δ^{++} particle. Without this extra quantum number, this particle would have three spin up quarks with a positive $\frac{2}{3}$ charge, which would indicate that these otherwise identical quarks all had the same quantum numbers with respect to spin and angular momentum. It was hypothesized that this effect could be explained if an additional quantum number, called color, existed. This new quantum number required three degrees of freedom, labeled red, blue and green. These are the charges of the strong force similar to the positive and negative charges of the electromagnetic force. But having 3 charges (and thus 3 anti-charges) results in a much more complicated scenario. All hadrons are colorless. Valence quarks are those quarks which determine the quantum number of their parent hadron, which can have any number of sea quarks and gluons. A baryon, containing 3 valence quarks, has to have one of each color. A meson, containing two valence quarks, will have a quark anti-quark pair, and these valence quarks can have color quantum numbers that are, for example, red and anti-red. The vector gauge bosons that carry the strong force are called gluons. Unlike photons, gluons carry color charge. Every gluon has a color charge and an anti-color charge. This means that there are 8 different gluons (since

gluons cannot exist in the color singlet state). An added complication is that the gluon's color charge means that gluons can interact with each other, unlike photons. The Quark Model predicted the existence of several undiscovered particles, including a spin $\frac{3}{2}$ Ω^- baryon. This particle was discovered at Brookhaven National Laboratory, verifying the theory and earning Murray Gell-Mann a Nobel prize for the quark model [38].

Gell-Mann's original model only proposed three quarks, the up, down and strange. Shortly after this, the charm quark was proposed because the additional quark better explained the weak interactions known at the time [39]. The existence of the charm quark was verified with the discovery of the first charmed meson, the J/ψ in 1974 [40]. In 1973 the number of quark flavors grew to the currently accepted value of 6 when Markoto Kobayashi and Toshihide Maskawa explained the experimental CP violation results by the addition of another pair of quarks: bottom and top [41]. CP violation is a violation of the conjugation and parity symmetry. This symmetry states that the laws of physics should be unchanged if particles were swapped with their anti-particles and mirror imaged.

After the additional quarks were added to the quark model, and the Standard Model was in its currently accepted form, there were several more important experimental verifications. The bottom quark was experimentally verified with the discovery of bottomonium in 1977 [42]. The existence of gluons was verified in three-jet events at PETRA in 1979. The last experimental piece of this puzzle was verified in 1995 with the discovery of the top quark at Fermilab [43, 44]. The only required standard model particle that has not been found is the Higgs boson. Much of the possible

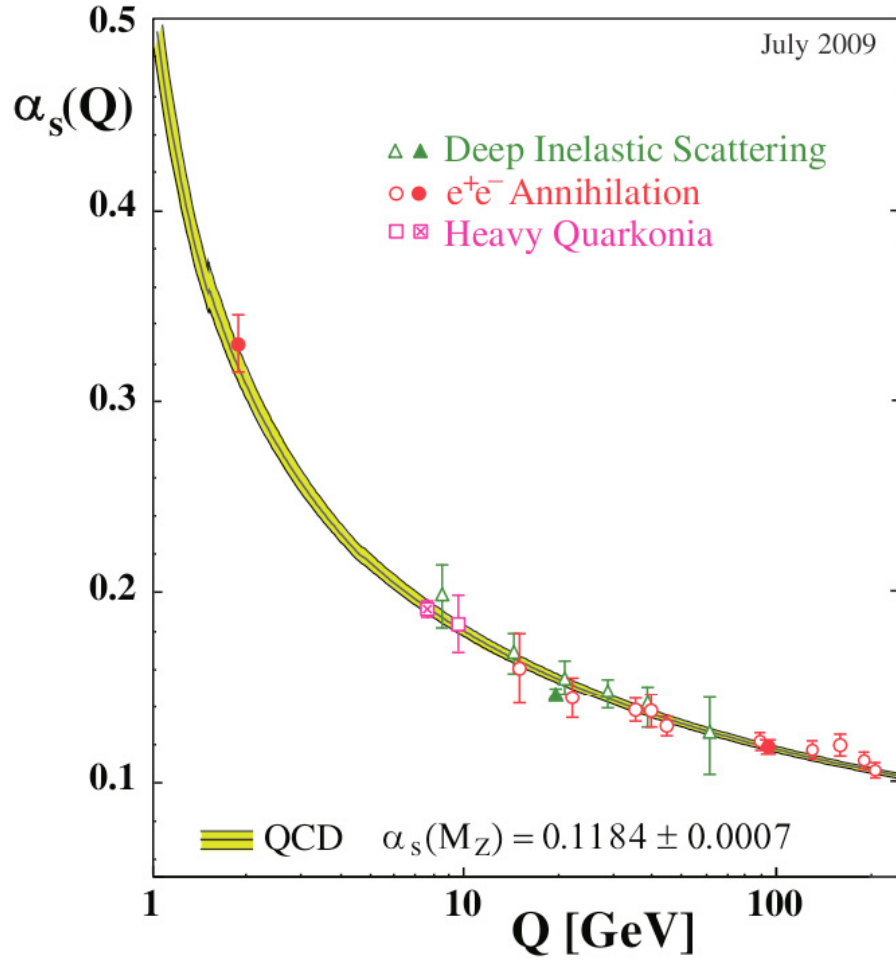


Figure 1.2. Measurements of the QCD coupling constant, α_s versus energy. The value of $\alpha_s(M_Z)$ is the world average for α_s at the mass of the Z^0 [6].

mass range for the Higgs boson has been excluded by Fermilab (FNAL), but they have not been able to confirm or deny its existence. The search for the Higgs boson is underway at the Large Hadron Collider (LHC).

Unlike the coupling constant that governs the strength of the electromagnetic interaction, the coupling constant for QCD, α_s , has an energy-dependent value as shown in Figure 1.2. Though it is important to note that at large enough energy scales, the electromagnetic coupling constant also changes. At low energies, $\alpha_s \sim 1$, which means that QCD calculations at these energies cannot be done perturbatively because

their higher order terms are not small compared to the leading order terms. This leads to an important aspect of QCD, asymptotic freedom, which was proposed by David Gross, David Politzer and Frank Wilczek in 1973 [45]. Asymptotic freedom means that at large energy scales, or short distance scales, the force between two colored objects becomes very weak. For QCD, this happens when the momentum of the parton in question is close to the same value as the Z^0 mass. At this momentum, $\alpha_s = 0.1184 \pm 0.0007$ [6] which is small enough that calculations can be done perturbatively.

No bare quark has been observed, which led people to believe that the quark model might simply be a convenient mathematical tool. The existence of quarks was verified by deep-inelastic scattering experiments carried out at SLAC in 1968 [46]. The absence of bare quarks was explained by quark confinement, which means that quarks are “confined” to mesons or baryons. Unlike the electromagnetic force, when two quarks are separated, the color field between them does not decrease with the distance. In fact, it becomes stronger, pulling them back together to stay confined within their hadron. If enough energy is applied, at a particle accelerator for instance, as they separate, it becomes energetically more favorable for a new quark-antiquark pair to appear out of the vacuum than for the two quarks to further separate. The quarks that pop out of the vacuum eventually hadronize into color-neutral mesons and baryons, along with the original separating quarks. This produces a spray of hadrons which we call a “jet”, with every hadron having its constituent quarks hidden away.

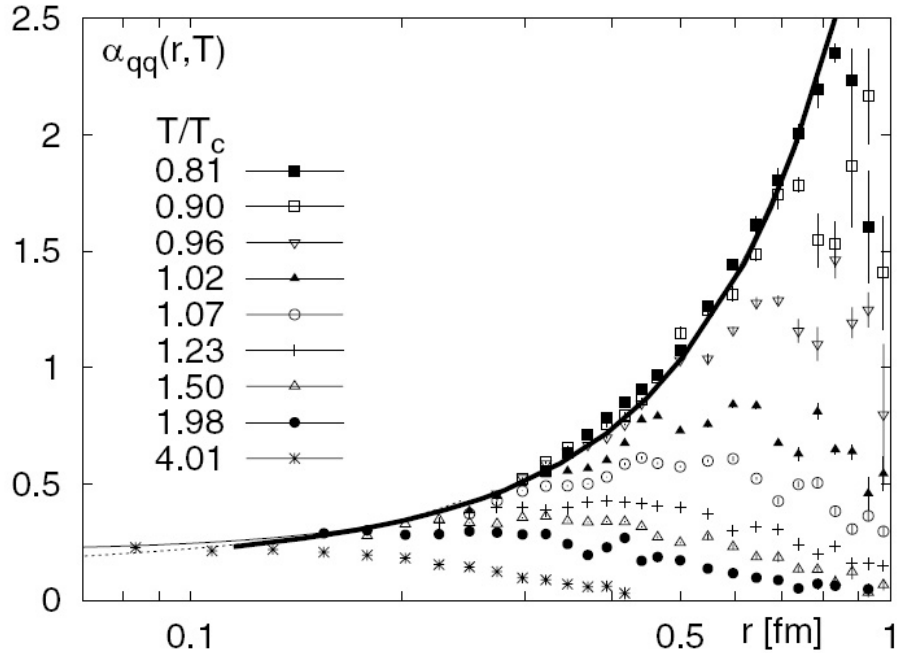


Figure 1.3. The relationship between the strong coupling constant $\alpha_s(\alpha_{qq}(r, T))$ vs r at different temperatures [7]. The thin black line is α_s at a temperature of zero. The thick black line and dashed lines are the results from a pure gauge theory. For further details, see Reference [7].

1.1 Quark-Gluon Plasma

The strong coupling constant, α_s , also is modified when a hot colored medium exists. In Figure 1.2, we see that asymptotic freedom is not reached until the quarks in question have a momentum near that of the Z^0 mass, well above the predicted temperature of the matter that is reached at RHIC. However, the existence of the color field makes it easier to pop quark-antiquark pairs out of the medium, which in turn lowers the magnitude of the force and thus is a modification of the strong coupling constant. We can see this in Figure 1.3 which shows a calculation from a potential model constrained by 2-flavor lattice QCD calculations. The details can be found in Reference [7]. This shows that at temperature $T > T_c$ the magnitude of

the strong force at a distance $\sim 0.2-0.5$ fm is greatly reduced in magnitude. Since this is the size of a typical heavy quarkonia meson, this indicates that at a certain temperature the force between the heavy quarks is sufficiently reduced that they are no longer bound.

This modification of the strong coupling at high temperatures will allow quarks to no longer be confined to their hadrons, but instead exist in a deconfined medium that we call the Quark Gluon Plasma (QGP). However, this simple idea needs to be further expanded if we are going to be able to quantify what a QGP is, what its signatures could be, and whether we do indeed see a QGP in heavy-ion collisions. Let's start with the first question, the definition of the QGP.

In 2005, the STAR collaboration along with the other experiments at RHIC, tried to determine whether evidence for a QGP existed in the data from the first three years of RHIC running. The definition used for QGP in this case was that the QGP is a state of matter in local thermal equilibrium, in which quarks and gluons are deconfined from hadrons, so that color degrees of freedom become manifest over nuclear, rather than merely nucleonic, volumes [47]. There are several important assumptions here. The first is the idea of local thermalization. The concept of temperature only has meaning when thermalization has occurred, since temperature is a bulk matter quantity that is a measure of the average kinetic energy of the associated particles. Deconfinement of the quarks from their hadrons has always been considered an important aspect of QGP. The difference between what the RHIC experiments claimed in 2005 versus what had been historically assumed is that there is no demand that quarks and gluons be non-interacting. This is based on two different ideas. One is that lattice QCD

calculations show that the temperature at which deconfinement sets in is much lower than the temperature needed for the quarks to be non-interacting. The second is that if the quarks and gluons were non-interacting, it would be very difficult for the resulting medium to thermalize in the time-scales necessary [47]. Models that have attempted to describe the QGP as a gas of hadrons have failed. Models that have attempted to describe the QGP as a weakly-coupled gas of quarks and gluons have also failed, but for some observables, such as light hadron v_2 at $< \sim p_T 2 \text{ GeV}/c$, treating the system as an ideal fluid works reasonably well. Some have given the label sQGP to this type of matter, where the s stands for strongly-coupled. However, I will continue to use the term QGP as the label for this matter in this thesis.

1.1.1 QGP Signatures

Given this definition of QGP, what would we expect the signatures to be? One signature would be the evidence of a phase transition between normal hadronic matter and the QGP. One model used to calculate the temperature of this phase transition is lattice QCD, where space-time points are discretized on a lattice, which results in a mathematically well-defined model. However, this model is computationally expensive as ideally we would want very small lattice spacing, $a \rightarrow 0$. Lattice QCD can only be used directly at a baryon chemical potential (μ_B) of zero. At values of $\mu_B \neq 0$ the expectation value of any observable that is a function of μ , m or T is not calculable [48]. An important Lattice QCD result at $\mu_B = 0$, shown in Figure 1.5, is that at T_c the number of degrees of freedom is much higher than for normal

hadronic matter. However, they do not reach the Stephan-Boltzmann limit shown by the arrows, which is a good theory indication that ideal gas models do not describe the QGP. Lattice QCD calculations at $\mu_B = 0$ indicate that a phase transition should occur somewhere between $T = 160$ and 190 MeV and depends greatly on the details of the calculation used to derive it [49]. This temperature is called T_c , and is defined as the point where deconfinement sets in. At $\mu_B = 0$, the phase transition is a crossover transition, so we can say that T_c is the crossover temperature. Since it is now believed that the phase transition at $\mu_B = 0$ is a crossover phase transition, it is experimentally difficult to determine [50]. At higher μ_B , the phase transition is first order and T_c is called the critical temperature.

The Lattice predictions for $\mu_B = 0$ can be seen in Figure 1.4, which is a phase diagram of nuclear matter with respect to the thermodynamic variables T and μ_B . There are quite a few models that have made predictions for the $T = 0$ axis of the QCD phase diagram. One such model is the MIT bag model, which predicts that a first order phase transition should exist [51]. These two predictions require that a critical point exist on the line between the hadronic matter phase and the QGP phase. A search for this critical point is underway in the RHIC beam energy scan program.

Hydrodynamic models give us another set of predicted signatures of the QGP. As stated in Section 1.1, given that the quarks still interact with each other even after the onset of deconfinement, a more appropriate model for the QGP than the ideal gas model would be to assume that a relativistic fluid exists. However, for this model to make sense, local thermalization is required. Any parton that has

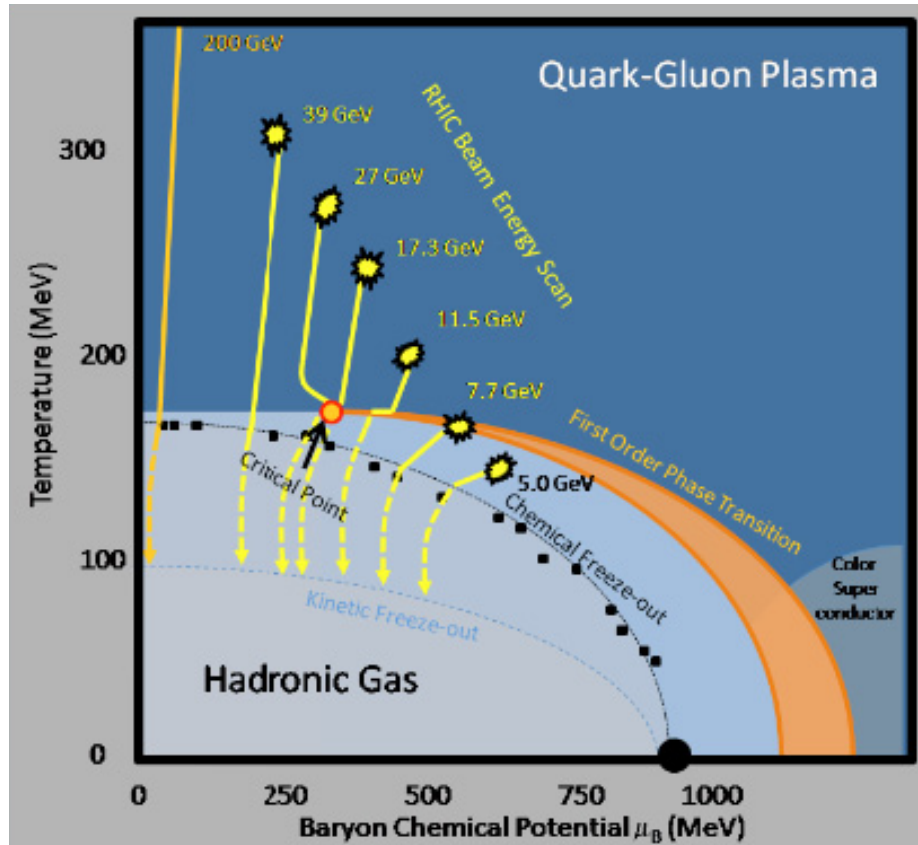


Figure 1.4. The QCD Phase diagram [8]. This shows the relationship between the QGP, and hadronic states of nuclear matter. It is currently believed that at high μ_B and low temperature, the phase transition is first order, and at low μ_B the phase transition is a crossover. A critical point should exist between the two transitions. However, at the time of this writing, this has not been experimentally verified.

had a hard scatter and gains a high transverse momentum will not interact enough with the medium to be thermalized. So hydrodynamic models are really only applicable for soft physics. These models predict that in non-central collisions (see 1.1.2 for further details) there will be an anisotropic pressure gradient resulting from the anisotropic spatial distribution of the matter left behind after the collision. This pressure gradient will cause an anisotropic momentum pattern, which we call elliptic flow. We can attempt to measure the flow by taking a Fourier decomposition of the azimuthal distribution and dividing the flow from the non-flow. One important

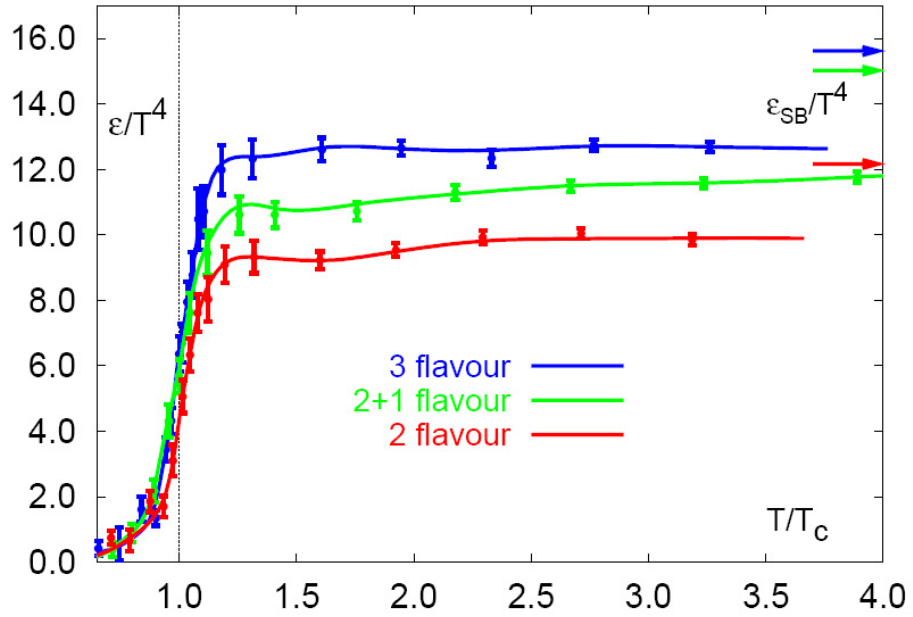


Figure 1.5. Degrees of freedom versus temperature from a Lattice QCD calculation given in reference [9]. The arrows indicate the ideal gas values.

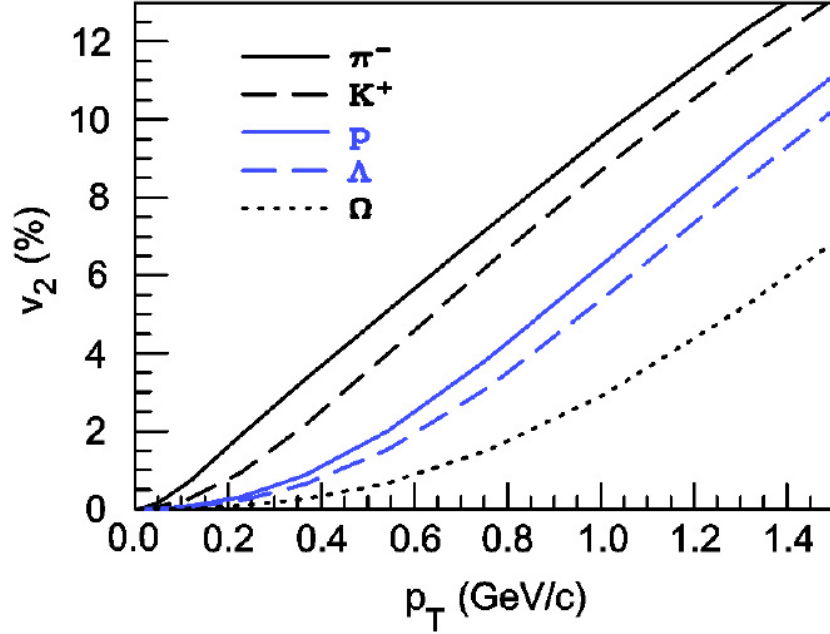


Figure 1.6. Elliptic flow predictions for various particle species versus p_T [10].

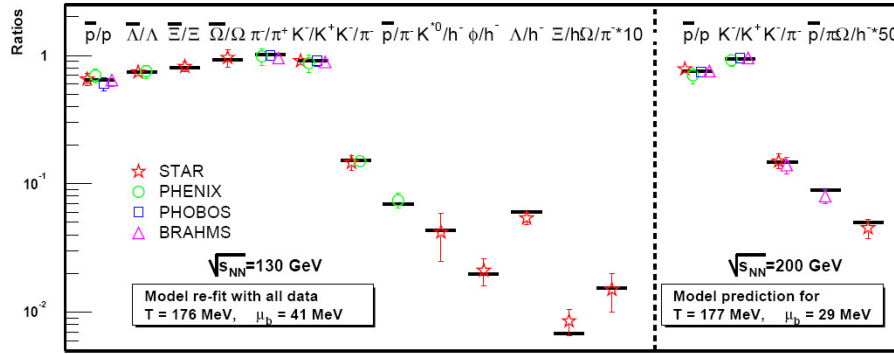


Figure 1.7. Comparison of the experimental data on different particle ratios measured at RHIC at $\sqrt{s_{NN}} = 130$ and 200 GeV with statistical model calculations. [11].

variable from this analysis is v_2 , which is the second coefficient in the decomposition.

A prediction from hydrodynamic models of the v_2 for various particle species can be seen in Figure 1.6. One key prediction is that it would be “self-quenching” as the anisotropic momentum flow will cause the pressure gradient to become more even, which means that the flow pattern is sensitive to the very earliest stages of the collision [10]. Further details on this measurement can be found in Section 1.1.2.

Statistical models introduce a third set of predicted signatures. What a statistical model does is derive the thermal equilibrium properties of a macroscopic system from the measured yields of the constituent particles. Basically, by applying a statistical model to the measured particle yields, one can determine whether our assumption of thermal (and chemical) equilibrium is valid. Statistical models are based on the use of a grand canonical ensemble to describe the partition function. There are only two free parameters in the model, temperature and baryon chemical potential (μ_B) [52]. If the assumption regarding thermal equilibrium is correct, it would be possible to fit a multitude of particle yields simultaneously. The result of such a fit can be seen in

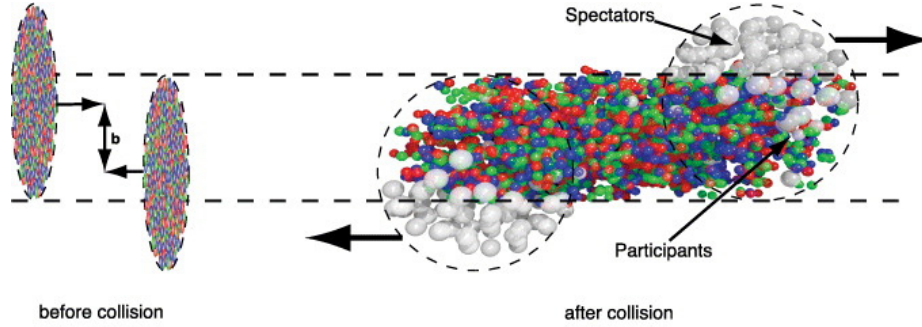


Figure 1.8. The picture on the left is a cartoon of two heavy ions prior to their collision with impact parameter b . The picture on the right shows what may occur after the collision, with some particle production coming from those nucleons that participated in the collision and some spectator nucleons continuing on after the collision. [12]

Figure 1.7, which shows very good agreement at $\sqrt{s_{NN}} = 200$ and 130 GeV. These fits indicate that as \sqrt{s} increases, $\mu_B \rightarrow 0$.

Up until this point, the QGP signatures discussed were from soft probes of the matter. These are probes where the momentum transferred during the initial scatters is small, so they involve measurements of the bulk as a whole. Another class of probes are hard probes, where the momentum transfer is large. Some of these signatures are jet quenching, parton energy loss and suppression of heavy quarkonia. A “jet” is the group of hadrons that have fragmented from an initial parton. The jets we are interested in are those that came from an initial hard scatter. When a parton transverses through a colored medium, it should lose energy via gluon radiation. This will result in “quenching” of the resulting jet where the jet has lost energy to the medium and may be completely suppressed. This is discussed in more detail in 1.12. The last predicted signature is the suppression of heavy quarkonia, which is the subject of this thesis. Further details can be found in Chapter 2.

1.1.2 Heavy-Ion Collisions

The only way to experimentally access the QGP is through heavy-ion collisions. The difficulty in measuring QGP effects is that these effects need to be disentangled from nonQGP effects that will also modify measurements made in a heavy-ion collision with respect to $p + p$ collisions. For instance, we need to disentangle QGP signatures from any initial and final state effects that are not the result of a QGP. In order to create a QGP, a large amount of energy needs to be deposited into a very small space. This is done by colliding heavy-ions, such as Au ions in the case of RHIC or Pb in the case of the LHC, at speeds very close to that of the speed of light. These ions were chosen due to their large size ($A = 197$ for Au and $A = 208$ for Pb), and their very nearly spherical shape. The latter is important because it adds a symmetry to the resulting collision that simplifies our analysis. The ions collide with a given impact parameter, b , as shown in Figure 1.8, which can not be experimentally measured. However, this impact parameter is important as it determines the centrality of the collision. A central collision is one where $b \rightarrow 0$, and should have the most nucleon-nucleon collisions and thus have the highest energy density. Since many analyses look at how much a heavy-ion event differs from a collection of independent $p+p$ collisions, this information is determined in a model-dependent way from multiplicity measurements. The details are given in Chapter 5. The following sections will discuss some experimental measurements that have been made which are consistent with some of the expected signatures of QGP formation outlined in the previous section.

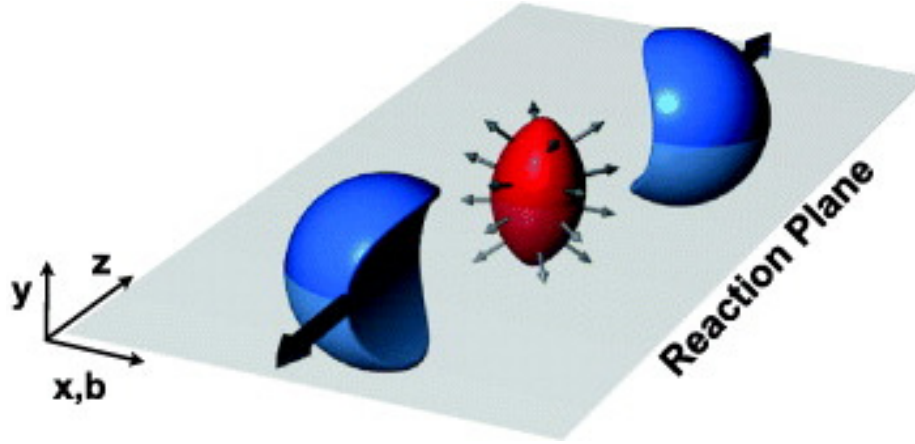


Figure 1.9. Picture of a peripheral collision, with the initial spatial anisotropy shown in red and the spectators in blue. [12]

Elliptic Flow

In order to determine whether a QGP has formed, it is necessary to determine both whether the medium formed in heavy-ion collisions is thermalized and whether it displays quark degrees of freedom. For a thermalized medium, we would expect to see bulk medium properties such as flow. All non-central collisions begin with an initial spatial anisotropy, which results in an anisotropy in the pressure gradient. This anisotropic pressure gradient translates to an anisotropy in the particle momentum distributions. [12]

In order to determine the flow, the reaction plane is defined by the z axis (which is itself is defined as the beam direction) and the impact parameter b as shown in Figure 1.9. A Fourier expansion of the invariant yield with respect to the reaction plane is then,

$$E \frac{d^3 N}{d\mathbf{p}^3} = \frac{1}{2\pi} \frac{d^2 N}{p_T dp_T dy} \left(1 + 2 \sum_{n=1}^{\infty} v_n \cos[n(\phi - \Psi_{RP})] \right), \quad (1.1)$$

where E is the energy of the particle, \mathbf{p} is the momentum vector, p_T is the transverse momentum, ϕ is the azimuthal angle, y is the rapidity, and Ψ_{RP} is the reaction plane angle. The $\sin[n(\phi - \Psi_{RP})]$ terms of this expansion were neglected in Equation 1.1 because it was assumed that they disappear due to the symmetry of the system with respect to the reaction plane. So we can define the Fourier coefficients as in Equation 1.2.

$$v_n(p_T, y) = \langle \cos[n(\phi - \Psi_{RP})] \rangle \quad (1.2)$$

The first component, v_1 , is known as directed flow. The second component, v_2 , is known as elliptic flow. The experimental method for determining flow is complicated as the reaction plane can not be directly measured. Rather it is estimated from the particle distributions directly, and to do this properly non-flow correlations must be subtracted. For instance, hard scatters and correlations due to resonances are some of the non-flow contributions. This estimation of the reaction plane is called the event plane.

Quark coalescence or recombination models predict a universal scaling of v_2 and p_T with n_q , where n_q is the number of valence quarks in a given hadron, because there should be no difference in collectivity among the u , d and s quarks near hadronization [53]. This can be seen in Figure 1.10. The large v_2 of the multi-strange baryons shown in this figure is also evidence for partonic collectivity.

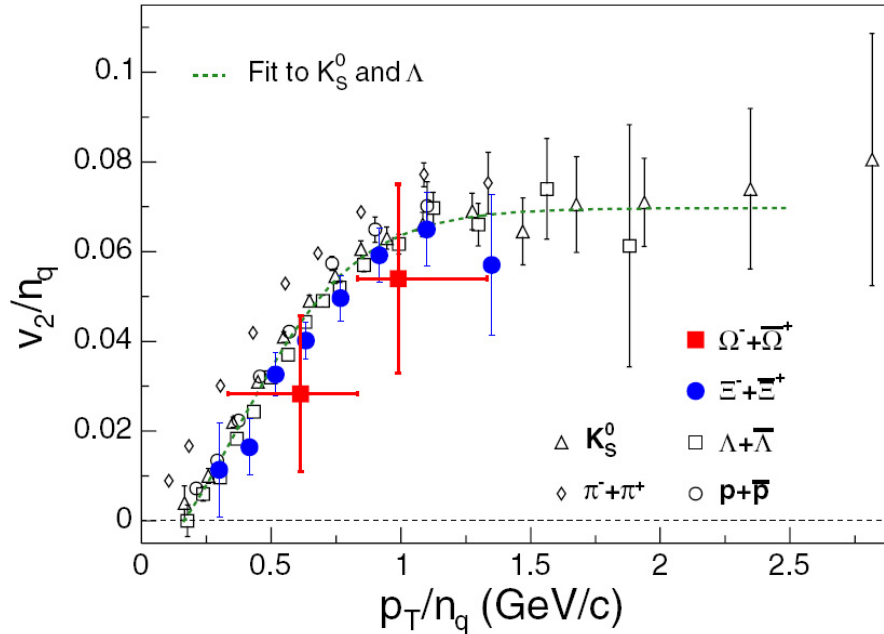


Figure 1.10. Number of quark (n_q) scaled v_2 as a function of scaled p_T . Once we scale the baryons and the mesons, they fall on the same curve, indicating that the flow originated prior to hadronization. [13]

Suppression of High p_T Hadrons

One way to determine the properties of the medium formed in heavy-ion collisions is to look at some process in $p + p$ collisions and $A + A$ collisions and determine whether the $A + A$ collision deviates from what we would expect if the $A + A$ collision could be treated as a simple superposition of independent $p + p$ collisions. This deviation is quantified with the nuclear modification factor (R_{AA}), which is the ratio of the yield in heavy-ion collisions over the yield in $p + p$ collisions, scaled by a model of the nuclear geometry of the collision such that $R_{AA} = 1$ indicates no modification due to the medium. If R_{AA} is < 1 , we can say that the probe of interest is suppressed in heavy-ion collisions. This does not necessarily mean that the suppression comes from the QGP, other factors such as Cold Nuclear Matter (CNM) effects can modify

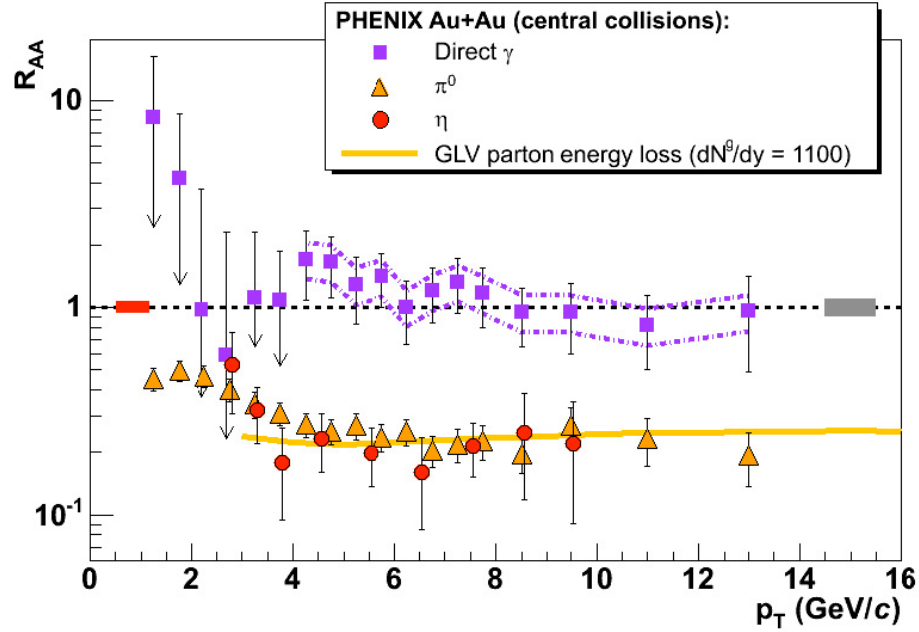


Figure 1.11. Nuclear modification factors of γ , π^0 , and η in central Au-Au collisions at $\sqrt{s_{NN}} = 200$ GeV from reference [13]

the production of the hadron of interest. Further details in determining the nuclear modification factor can be found in Section 5.1.4.

High p_T hadrons make an ideal probe because the production of their parent partons can be calculated perturbatively, unlike a soft process. These partons are colored objects, so we would expect them to be modified by the QGP. This can be seen in Figure 1.11. The large suppression in this figure for the π^0 and the η indicates that the medium formed is quite dense. An important check is looking at a hard process that should not be modified by the medium, and one such process would be direct photons. A photon has no color charge, so it should not be modified at all, as also shown in Figure 1.11. The photons have an R_{AA} of 1 and thus follow N_{binary} scaling, indicating that our method of calculating R_{AA} is consistent with our model expectations that hard processes which should not be modified by the medium.

Jets and correlations

By measuring the total energy and momentum contained within a jet, we can determine the properties of the parton that produced it. Prior to the techniques developed to allow full jet reconstruction in heavy-ion collisions, a proxy for jets was found by examining the azimuthal correlations between a leading hadron with high p_T and the other hadrons within the same event. This allowed jet quenching to be studied without interference from the background of a heavy-ion event [54]. This is done by looking at $dN/d\Delta\phi$ where $\Delta\phi$ is the difference between the azimuthal angle of the leading hadron and all the other hadrons in that event within a certain p_T range. When high p_T partons are produced in pairs in the initial hard scattering we expect them to be π radians apart (back-to-back) due to conservation of momentum, and this is the dominant effect in this azimuthal correlation. The azimuthal correlation structure associated with the leading hadron is called the “near-side” and the structure associated with particles with $\Delta\phi \sim \pi$ is the “away-side”. In $p + p$ collisions, we do not expect to have any modification of the away-side structure if we assume that there is no QGP produced in $p + p$ collisions. The away-side structure will be broader in these collisions due to the selection method outlined here, as the near-side preferentially will have more of its momentum locked up in a single hadron. [55]

In heavy-ion collisions, when the near-side jet (or dihadron structure) is found, it is biased such that it comes from near the surface of the QGP fireball. This bias is due to the fact that jets which come from below the surface will lose energy so they

are harder to find as most jet-finding algorithms include a p_T cut-off. Even if the resulting jet is unmodified by the medium except for the energy loss, the exponential spectrum of the jet cross section means that far more jets of that measured energy will have come from the surface. When a near-side jet is selected, this bias indicates that the away-side jet could have traveled through the medium (there will be some bias towards pairs that are tangential to the surface of the fireball). If there is a QGP, we would expect to see suppression of the away-side jet in $A+A$ collisions compared to $p+p$. This suppression in a dihadron correlation study is very easily seen in Figure 1.12. Also shown in this figure are the central d+Au results, where we can see that the away-side structure is mostly unmodified. This is important because this indicates that any modification seen in Au+Au collisions is not the result of Cold Nuclear Matter Effects (CNM). Similar measurements have been made with full jet reconstruction. There are many different jet-finding algorithms, one can find an overview in reference [56]. The simplest algorithm is the cone algorithm. In this algorithm, a cone with radius $R = \sqrt{\Delta\phi^2 + \Delta\eta^2}$ is constructed. All the particles within the cone are assumed to come from the same jet and their momentums are combined. Just as with the dihadron azimuthal correlations, there will be a near-side and an away-side jet.

Heavy Flavor Suppression

Heavy Flavor is the term used to describe hadrons that contain either a charm quark or a bottom quark. We do not consider the top quark as it decays too quickly to be bound into a hadron. The mass of the charm quark is $\sim 1.3 \text{ GeV}/c^2$ and the

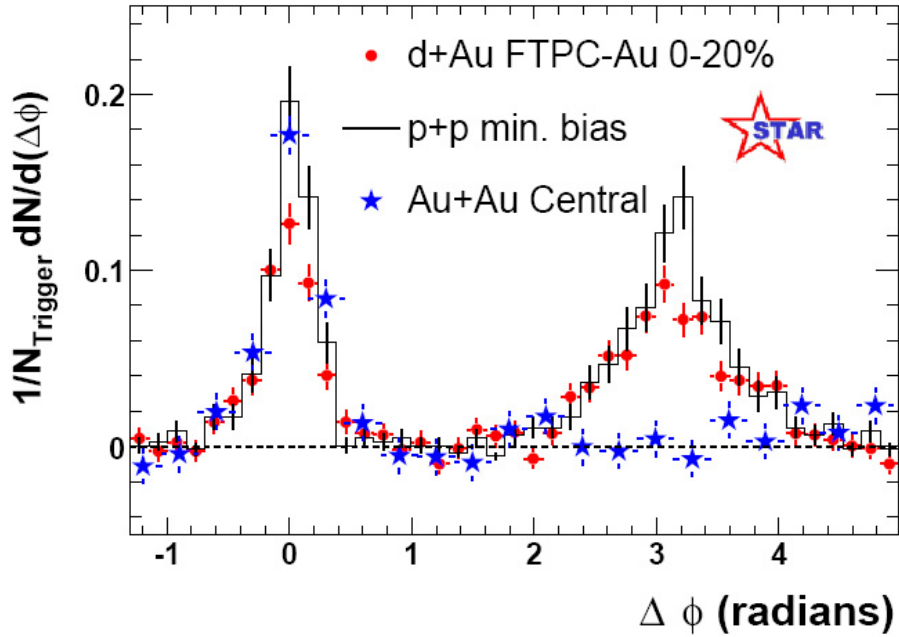


Figure 1.12. Dihadron azimuthal correlations from reference [14]. In black is the reference $p + p$ result, in red is the d+Au result and in blue is the central Au+Au result.

bottom is $\sim 4.2 \text{ GeV}/c^2$ [57], heavy enough that the heavy quark production can be calculated perturbatively. These quarks are also heavy enough that it was assumed that they were only produced in the initial hard scatter. A measurement of the total $\sigma_{c\bar{c}}$ in Au+Au collisions at STAR showed that it followed binary scaling which indicates that this assumption is valid [58]. Heavy flavor can be divided into two categories: Open heavy flavor where the heavy quark is paired with a lighter quark (e.g. B and D mesons), and closed heavy flavor, more commonly referred to as Heavy Quarkonia. It is called closed heavy flavor because there is no net charm (or bottom) quantum number to these mesons, so the charm (bottom) is “hidden”. I will discuss quarkonia in heavy-ion collisions, the topic of this thesis, in the following Chapter.

At STAR, we look at the semileptonic decay of the D and B mesons to electrons.

These are given the label non-photonic electrons (NPE) and allow us to reconstruct the azimuthal direction of their parent B and D mesons. An NPE R_{AA} can also be calculated, as described above. It had been assumed, previous to measurements from PHENIX, that heavy quarks would be less suppressed than light quarks due to the dead cone effect [59]. However, at high p_T the suppression of NPE is very similar to that of the π s. This is shown in Figure 1.13. Another interesting result is that the v_2 of the NPE is also not zero [15], indicating that heavy quarks have some flow. Like the NPE R_{AA} this was an unexpected result because it had been thought that the v_2 of heavy quarks should be much smaller because their expected thermalization time was thought to be larger than that of the light quarks due to their reduced energy loss via gluon radiation [60].

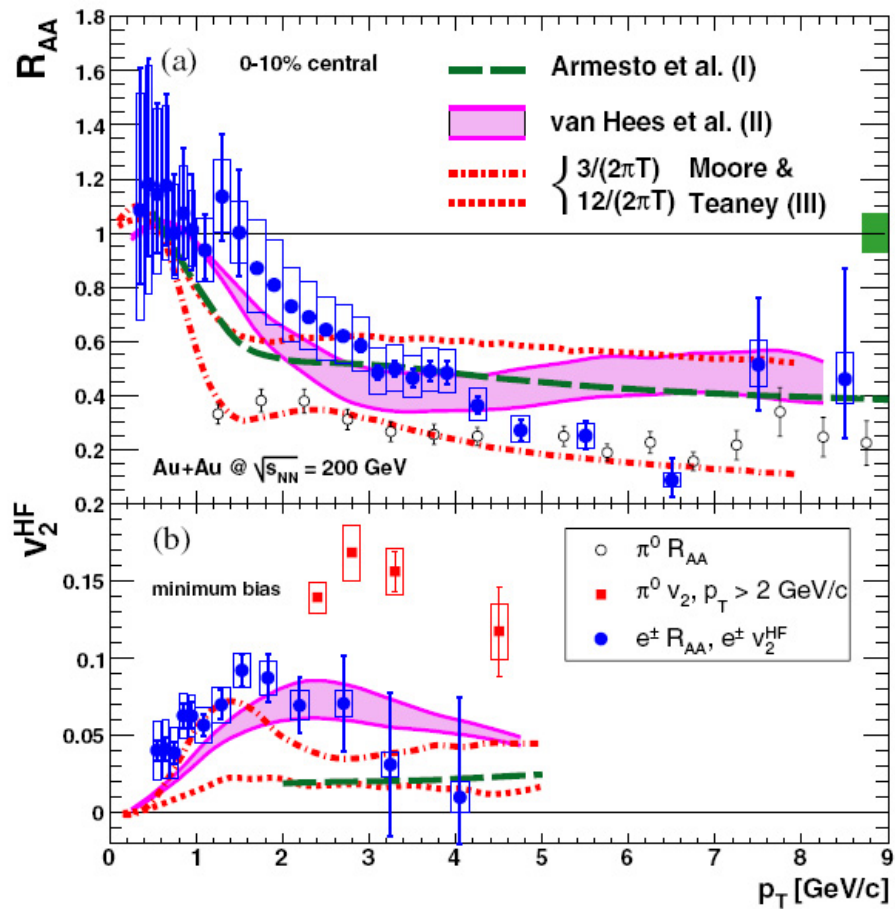


Figure 1.13. The top graph is a PHENIX measure of the R_{AA} of electrons from heavy flavor decays in blue. In open circles the R_{AA} of the π^0 is shown again. The lines are from model calculations. The lower graph is the v_2 for the same particle species. Note that these are not scaled by n_q , the interesting result here is simply that the heavy mesons seems to flow. This graphs come from reference [15].

Chapter 2

Quarkonia

Heavy Quarkonia are an excellent hard probe of the medium produced in heavy ion collisions. It is defined as bound charm-anticharm or bottom-antibottom pairs. The $c\bar{c}$ $1S$ bound state is the J/ψ while the $b\bar{b}$ bound $1S$, $2S$ and $3S$ states are given the labels $\Upsilon(1S)$, $\Upsilon(2S)$, and $\Upsilon(3S)$ (or sometimes Υ , Υ' , Υ''). The formation times of the J/ψ and Υ are less than $1 \text{ fm}/c$ ($t \propto 1/m_Q$), which indicates that they form prior to the creation of the QGP which has a formation time on the order of $1 \text{ fm}/c$ [1]. The ground states of heavy quarkonia (J/ψ and $\Upsilon(1S)$) have a high binding energy when compared to lighter hadrons. Whereas the higher order states have binding energies that are more similar to that of the lighter hadrons, and significantly less than that of the ground states. This indicates that if we were to ignore all other effects besides the Debye screening of the $Q\bar{Q}$ pair, we should see a sequential suppression that depends on the temperature of the medium [61]. Also the heavy quarkonia states have reasonable dilepton decay branching ratios. This is important as the leptons do not carry color charge and will not be modified by the QGP and reconstructing the

invariant mass of the state from dileptons is a straight forward signature.

2.1 Production

In order to use quarkonia as a probe of the QGP, it is necessary to understand its production mechanism. Unfortunately, despite the fact that the masses of the J/ψ and the Υ are large so that perturbative (pQCD) calculations are applicable, we still do not understand their production mechanism. However, the hadronization method by which the charm and anti-charm (bottom and anti-bottom) become a J/ψ (Υ) is not understood. Another complication is that a significant portion of the yield of the lower mass charmonium and bottomonium states is the result of feed down from the higher-mass states [61]. In many experiments, such as at STAR, we measure the inclusive yield of the lower mass states and can not separate the direct production from the production due to feed down. Since the different states will be effected differently by QGP effects, this can complicate our understanding of our quarkonium measurements in heavy ion collisions.

Obviously as fully formed mesons, both the J/ψ and the Υ are colorless, so the first models used to describe the formation assumed that the $Q\bar{Q}$ pair was produced in a color singlet state and then hadronized. Other models assume that the $Q\bar{Q}$ pair is in a color octet state, which means that it has a net color charge. In order to hadronize and become a bound meson, the heavy quark pair must shed the color by radiating one or more gluons. It is important to understand the production mechanism of this particular probe because one can easily envision a scenario where the QGP could

modify the quarkonium yield differently depending on what production mechanism is valid. Further elaboration on the issues facing a heavy ion quarkonia analysis can be found in 2.7.

In each model, it is assumed that the production of the meson obeys factorization. This means that the production is just the product of the parton distribution functions (PDF) \times the pQCD cross section. The production cross section of the initial hard scatter that produced the heavy quark pair is calculated in pQCD. This pair of heavy quarks must be nearly on-shell (non-virtual) and the quarks must have a low relative velocity with respect to each other. It is also assumed that the final state quarkonium retains the spin of the $Q\bar{Q}$ pair. Further descriptions of quarkonia production models can be found below.

2.2 Color Singlet Model

In the Color Singlet Model (CSM) a hard gluon is assumed to come off the same vertex as the heavy quarks which carries the net color away from the pair of heavy quarks. The heavy quarks then hadronize and retain their initial spin [21]. The problem is that this model drastically underpredicts the yield of the J/ψ and the Υ . However, adding Next to Leading Order (NLO) terms can increase the yield in this model. A CSM calculation is compared to data for the J/ψ and the Υ at $\sqrt{s_{NN}} = 200$ GeV [16], is shown in Figure 2.1. The STAR Υ point in this figure is from a preliminary version of the results discussed in this thesis in Chapter 4. As we can see, this calculation still underpredicts the Υ differential cross section.

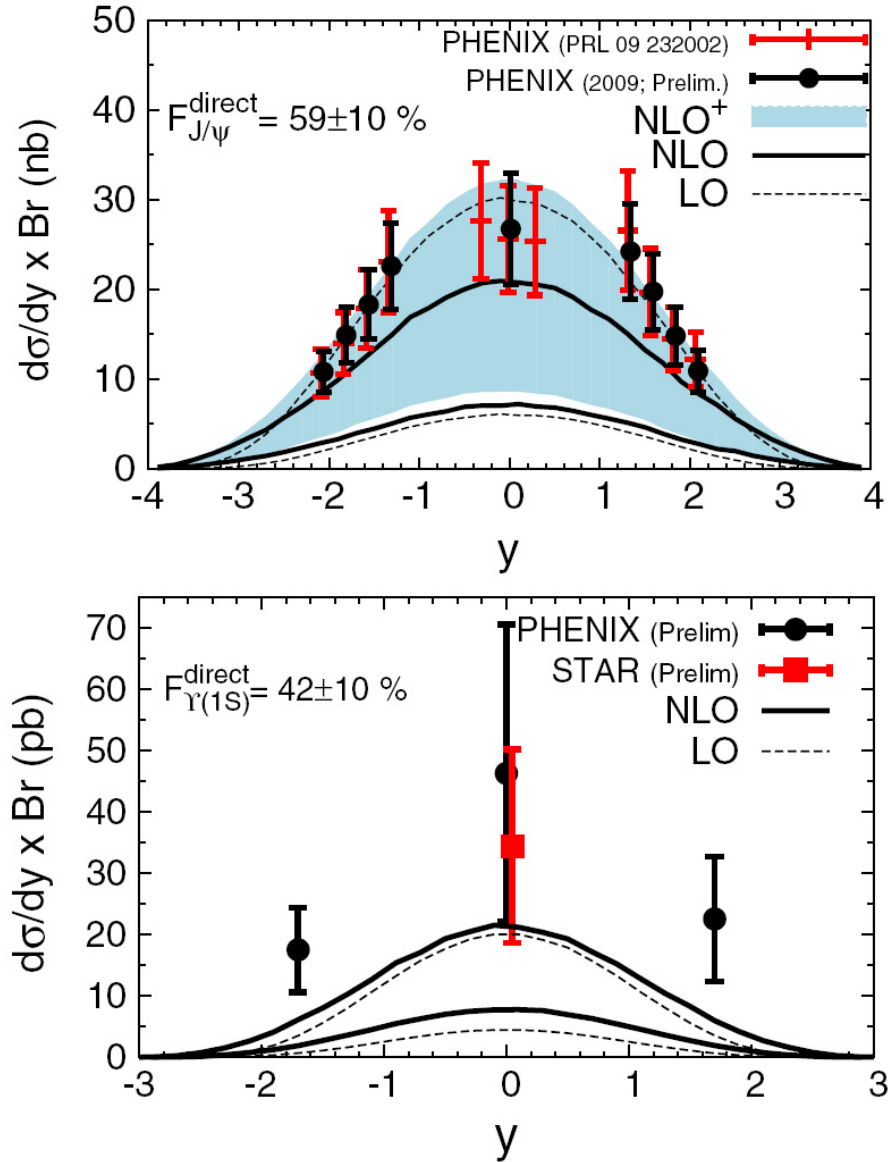


Figure 2.1. The top graph is a comparison of the PHENIX J/ψ results multiplied by an estimate of the fraction that are direct compared to the CSM at LO, NLO and NLO+ cg fusion model. The cg stands for the fusion of a gluon with an intrinsic charm quark in the nucleon sea. The lower graph shows the PHENIX Υ results and the STAR Υ results (that will be discussed in Chapter 4 of this thesis) also multiplied by an estimate of the percentage that come from direct production. These are compared to LO and NLO CSM calculations. These graphs come from Ref. [16].

2.3 NRQCD

Nonrelativistic QCD (NRQCD) is another approach used to calculate heavy quarkonium production. As noted above, color singlet LO terms do not accurately predict

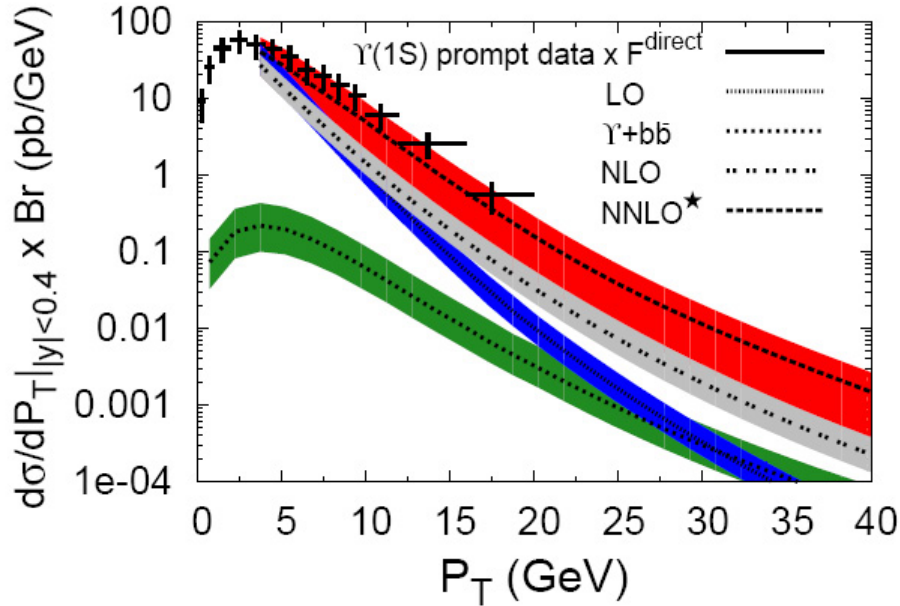


Figure 2.2. Results for $\Upsilon + X$ at LO, full NLO and for NNLO* compared to results from $\sqrt{s} = 1.8$ TeV measured by CDF. This calculation comes from Reference [17]. The theoretical uncertainty comes from uncertainties in the choice of scale and the mass of the b quark. See the Reference for further details.

the yield of heavy quarkonium yield as a function of p_T . Color octet terms were added to the color singlet terms and this allowed theoretical calculations to achieve a p_T dependence for the quarkonia yield that closely followed data [17]. However, this approach yields a polarization that does not agree with the data taken by D0 or CDF [17]. Additional improvements to these calculations can be done in the NRQCD model by the addition of NLO and some NNLO terms as outlined in Reference [17]. The comparison of this calculation with CDF data for the $\Upsilon(1S)$ state are shown in Figure 2.2. This calculation suggests that color octet terms are not needed to accurately predict the heavy quarkonium data. However, the model that best describes the data in this thesis is described next.

2.4 Color Evaporation Model

The calculations that best describe the $p + p$ $\Upsilon(1S + 2S + 3S)$ cross section discussed in this thesis were done in the Color Evaporation Model (CEM). In the CEM it is assumed that the heavy quarkonium yield is a fraction of the total yield of all $Q\bar{Q}$ pairs that are below two times the mass of the relevant lowest mass heavy flavor hadron. So, for the Υ we would want to calculate the fraction of all $b\bar{b}$ pairs that form Υ s that are below the threshold for producing a $B\bar{B}$ pair. In this model, there are no constraints on the spin or the color of the final state. Since the resulting heavy quarkonium needs to be colorless to be a bound state, it is assumed to interact with the color field induced by the collision and become color neutral. The loss of the net color of the pair is the “color evaporation” referred to in this model [32]. The quarkonium cross section can be a small fraction of the total of the total $Q\bar{Q}$ cross section. For instance, for the Υ , the fraction of the $b\bar{b}$ cross section with mass less than two times the B mass is on the order of 0.02 [32].

This fraction, which we can give the label F_{Υ} for the Υ family is fixed by data, but then should remain constant with respect to \sqrt{s} , y , and p_T . The calculation for F_{Υ} does depend on the quark mass, the scale, the parton densities, and the order used in the calculation. The constant value of this fraction with respect to \sqrt{s} , y , and p_T was verified that this fraction is universal in Reference [62]. CEM calculations are often taken to NLO as LO does not describe high p_T quarkonium production [32]. We compare a NLO CEM calculation for midrapidity Υ to our data in Figure 6.4.

2.5 Cold Nuclear Matter Effects

The method used to measure the modification of heavy quarkonia, as explained in 1.1.2, is to look at the ratio of the yield in $A + A$ collisions and compare that to $p + p$ collisions. What we are interested in are modifications that are the result of a deconfined phase of colored partons. However, it is possible to have some modification of the yield simply because the partons that participate in the hard scattering that creates the quarkonia are contained within a nucleus. These modifications are called “Cold Nuclear Matter” (CNM) effects because they exist at normal nuclear densities and temperatures. These modifications can be measured by looking at $p + A$ or $d + A$ collisions and finding a ratio very similar to R_{AA} which we give the labels R_{pA} or R_{dA} respectively. The ratio of R_{AA}/R_{dA} will indicate how much the yield of the heavy quarkonia is suppressed beyond any CNM effects. If this ratio is below 1, we can say that we see an anomalous suppression of the heavy quarkonia.

Cold nuclear effects can be divided into two categories, initial-state effects and final-state effects. Initial state effects are those that modify the production of the $Q\bar{Q}$ pair. A final state effect is one that modifies the quarkonium meson, by destroying it after it has formed or preventing the hadronization of the $Q\bar{Q}$ pair into a J/ψ or Υ . Some initial state effects include: modification of the parton distribution function, shadowing, and energy loss by the parton traveling through the nucleus. A final state effect is absorption of the newly formed quarkonium by nucleons as it passes through the newly formed nucleus [18]. Experimental measurements are necessary to constrain the theory results and allow these various effects to be separated and quantified. For

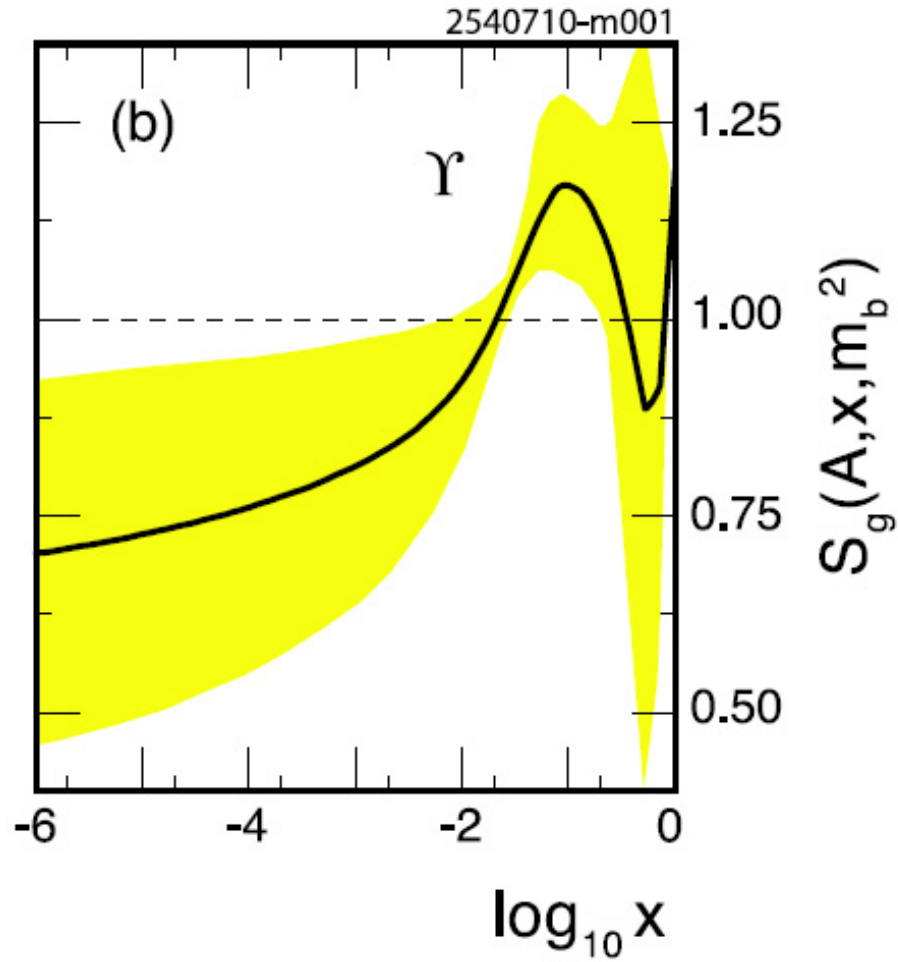


Figure 2.3. This is the EPS09 gluon-shadowing parameterization at $Q = m_b$ versus $\log_{10} x$. The shaded bands are the uncertainty in the calculation. At $\sqrt{s_{NN}} = 200$ GeV, the shadowing results are consistent with 1 for the Υ as the Feynman x region for Υ production is ~ 0.05 (or $\log_{10} x = -1.3$), though it's possible that this measurement could be in the anti-shadowing region. See reference [18].

instance, current shadowing parameterizations have large uncertainties, as seen in Figure 2.3. Shadowing is an initial state effect where one nucleon modifies the parton densities of the other partons within the nucleus, modifying the probability that they will be involved in the hard scatter.

2.6 Quarkonia in Heavy Ion Collisions

J/ψ suppression due to the Debye screening of the QCD potential between the $c\bar{c}$ pairs was originally believed to be an unambiguous signature of QGP formation [1]. One advantage to heavy quarkonia is that, unlike the lighter hadrons, the bulk of the mass of the quarkonia comes from the mass of its quarks. This means that the velocity of the quarks within the meson is quite low. Thus a nonrelativistic calculation can be done to model the binding of the quarks. This calculation was done using a simple model where the nonrelativistic confining color potential, V , at $T = 0$ was parameterized in terms of a linear term with the string tension σ and a $1/r$ contribution containing a Coulomb-type coupling [20]. This potential is called a ‘‘Cornell’’ potential,

$$V(r) = \sigma r - \frac{\alpha}{r} \quad (2.1)$$

$$\left[2m_Q - \frac{1}{m_Q}\nabla^2 + V(r)\right]\Phi_i(r) = M_i\Phi_i(r) \quad (2.2)$$

Since this is a nonrelativistic calculation, this potential can simply be used with the above Schroedinger equation [20] where m_Q is either the charm or bottom mass, and M_i is the mass of the particular quarkonium state. This allows one to calculate the mass and the average size of the quarkonia mesons. The predictions match very well with experimental evidence. The measured masses of the J/ψ and the Υ can then be used to fix the parameters σ , α , m_Q , and the other quarkonia states are calculated using these fixed parameters. As stated in the Introduction of Chapter 1, the two quarks can be separated until it becomes energetically favorable to pop a $q\bar{q}$ pair out

of the vacuum. But the question we really care about is: what happens when we are not in a vacuum? What about a deconfined medium of quarks and gluons?

A simple way to calculate this would be to modify the potential so that it is also a function of temperature in the following manner [20]:

$$V(r, T) \sim \sigma r \frac{1 - e^{-\mu(T)r}}{\mu(T)r} - \frac{\alpha}{r} e^{-\mu(T)r} \quad (2.3)$$

where $\mu(T)$ is the temperature dependent screening mass (inverse of the Debye screening radius). One can use this with the Schroedinger equation to determine the temperature at which a particular quarkonia species would disassociate. However, there are difficulties with this model, mainly the result of ambiguities in the choice of potential. However, the idea is very similar regardless of the choice in potential and can give us a good picture of what the modification of quarkonium mesons in a hot medium may look like.

Recent developments have allowed us to improve our use of potential models through the use of spectral functions. The potential is assumed to have a real and imaginary part. The real part is constrained by the lattice QCD data with a finite temperature through the use of the meson correlators [19]. The imaginary part is calculated using pQCD [19], as this is not possible to calculate within lattice QCD. In the non-relativistic limit, which we can use for heavy quarkonia, the calculation of these correlators is the same as solving the Green's functional form of the Schroedinger

equation as shown in Equation 2.4 [19, 63]:

$$\left[-\frac{1}{m}\vec{\nabla}^2 + V(r, T) - E\right]G(\vec{r}, \vec{r}', E, T) = \delta^3(r - r') \quad (2.4)$$

The spectral function, $\sigma(\omega, T)$, can be calculated from the Green's function in the following manner [19]:

$$\sigma(\omega, T) = \frac{6}{\pi} \text{Im}G(\vec{r}, \vec{r}', E, T)|_{\vec{r}=\vec{r}'=0}$$

The result of this analysis for calculating Υ bound states are shown in Figure 2.4. One obvious difference is that the addition of the imaginary part of the potential increases the width of the existing states, this is called ‘‘Landau’’ damping. This in turn may call into question what it means to be a bound state. For instance, if we look at $T = 245$ MeV, in both cases we can see the $\Upsilon(2S)$ state, but it appears to be barely above the continuum in the case where the imaginary part of the potential is included. This indicates that any perturbation could send the $\Upsilon(2S)$ into the continuum, and this is called threshold enhancement. These calculations include these two effects in addition to the screening effect.

After the prediction by Matsui and Satz, and some development of the potential models, the suppression of J/ψ was observed by both SPS and RHIC with the SPS results shown in figure 2.5 [2] and the comparison between SPS and RHIC shown in Figure 2.6, which indicates that the strongly interacting matter formed in these collisions does modify the production of the J/ψ . The magnitude of the suppression

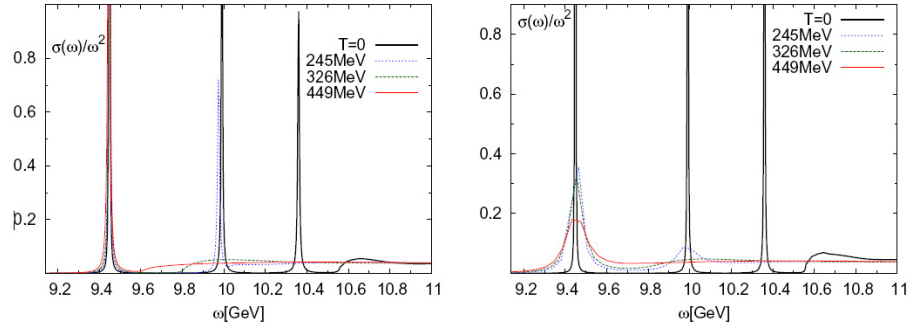


Figure 2.4. The graph on the left shows the bottomonium spectral functions if only the real part of the potential is used. On the right the is the spectral function if both the real and imaginary part of the potential are used [19].

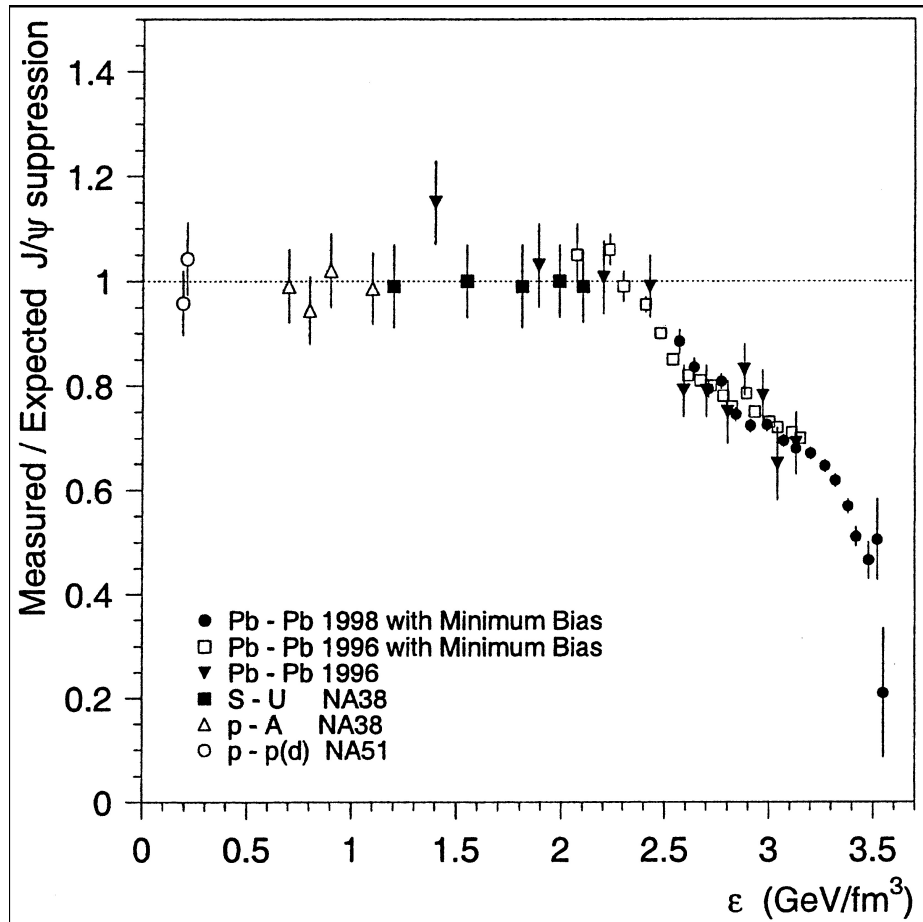


Figure 2.5. Measured J/ψ production yields shown as a function of the collisional energy density. These yields are normalized to the expected yield assuming the only source of suppression is the ordinary absorption by the nuclear medium. The expected yield was determined by proton-ion collisions [2].

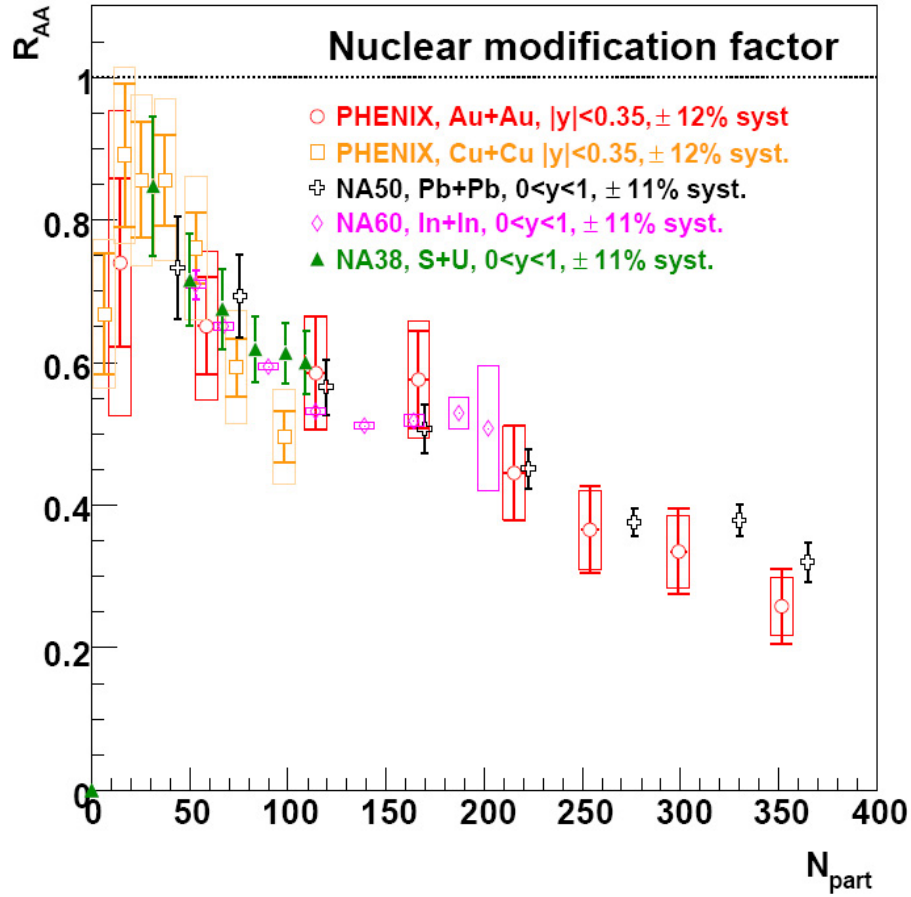


Figure 2.6. J/ψ R_{AA} versus the number of participants at mid-rapidity for the SPS and RHIC energies. Despite the differing energies, the nuclear modification factors appear to be the same for all data sets [20].

was similar for both RHIC and SPS despite the different energy densities, verifying that the original model of the J/ψ production being most affected by Debye screening was too simplistic. One factor that needed to be accounted for was the CNM effects, as SPS was in the anti-shadowing regime and RHIC was in the moderate shadowing regime.

As stated in Section 2.5, the cold nuclear matter effects can change the yield of the quarkonia states in heavy ion collisions regardless of whether a QGP was formed. Since these effects have a strong dependence on x , a shift in energy from SPS to RHIC

indicates a shift in x as we would be looking at the same Q^2 . This change in x from SPS to RHIC should move us from the anti-shadowing region to a strong shadowing region, which would increase the J/ψ yield from SPS to RHIC assuming all other effects were the same.

One effect that can be seen in heavy ion collisions that can enhance the quarkonia yield is recombination, where $c\bar{c}$ or $b\bar{b}$ quarks produced in different hard scattering collisions combine to form a quarkonia meson. Recombination will increase with $\sqrt{s_{NN}}$ as the cross section for $c\bar{c}$ and $b\bar{b}$ pairs increases. This in turn, will increase the probability that they will find each other within the fireball and hadronize. Another effect that plays a role in heavy ion collisions is the absorption to comoving hadrons. This final state effect occurs when secondary hadrons that are near the produced quarkonium meson in phase space scatter off of it inelastically. As with many of these effects, absorption due to comovers increases with $\sqrt{s_{NN}}$ [64].

Another issue to consider is the geometry of the QGP fireball. A quarkonia meson that forms on the outside surface will not disassociate regardless of the temperature of the medium because it doesn't have a chance to interact with it. This is why we never see a R_{AA} that is equal to zero. The formation time of the quarkonia meson, the QGP and the QGP lifetime can affect the apparent suppression as well. For instance, a high p_T quarkonia meson could have a formation time long enough that it actually does not see the QGP at all and thus isn't suppressed.

Yet another issue is the effect of feed down from higher order states. Roughly half of the yield of the J/ψ and the $\Upsilon(1S)$ come from the decays of excited states [61]. If a higher order state is suppressed, it will be reflected in a lower R_{AA} for the lower

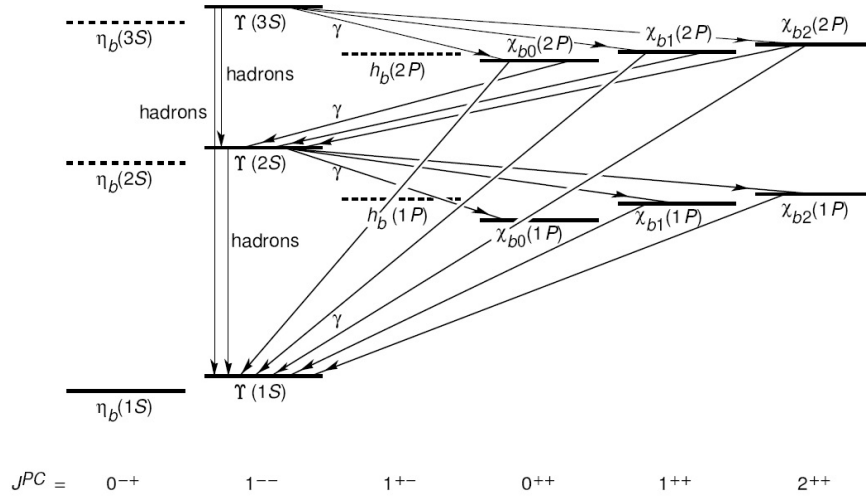


Figure 2.7. This shows the spectrum and transitions of the bottomonium family with masses below the $B\bar{B}$ threshold [21].

states, even if those ground states were unmodified by the medium. The spectrum of the bottomonium family can be seen in Figure 2.7.

2.7 $\Upsilon(1S + 2S + 3S)$ Family as a probe

Recent increases in integrated luminosity have made it possible to measure the Υ states in both $p + p$ and $A + A$ collisions. Υ at $\sqrt{s_{NN}} = 200$ GeV is in many ways a better probe than the J/ψ despite its much smaller cross section. Many of the non-QGP effects which modify the quarkonia yield in heavy ion collisions are much smaller for the Υ than for the J/ψ . For instance, recombination will always be less for the Υ family as $\sigma_{c\bar{c}} > \sigma_{b\bar{b}}$. Therefore, the systematic uncertainties due to these effects should be much smaller for the Υ family. Cold Nuclear Matter effects for midrapidity $\Upsilon(1S)$ are calculated to be negligible [18]. Other suppression mechanisms, such as the effect of co-moving hadrons, is lower for the Υ than for the J/ψ [3]. Also, one of the

important results is a measurement of relative suppression. The ψ' is very difficult to measure which makes it difficult to compare the J/ψ to other charmonium results.

In order to measure the ΥR_{AA} a baseline $p + p$ cross section measurement must be made. The techniques and results for this measurement will be discussed in Chapter 4. Next, the results for the measurement of ΥR_{AA} at $\sqrt{s_{NN}} = 200$ GeV from two different runs will be discussed. The first is from a run with an identical detector and trigger set-up as in the $p + p$ analysis. The latter was from a larger data set taken with less inner detector material and a modified trigger that had a higher efficiency. This will be discussed in Chapter 5.

Chapter 3

Experimental Facilities

Brookhaven National Lab, home of the Relativistic Heavy Ion Collider (RHIC), is located in Upton, New York. RHIC can collide protons, deuterons, copper ions and gold ions at a variety of energies from $\sqrt{s_{NN}} = 7.7$ GeV to 200 GeV for the ions and up to 500 GeV for the polarized proton beams. The performance specification for the Au-Au luminosity of RHIC was $2 \times 10^{26} \text{cm}^{-2} \text{s}^{-1}$ and for $p + p$ was $1.4 \times 10^{31} \text{cm}^{-2} \text{s}^{-1}$ [65]. The Υ trigger in run 6 $p + p$ with $\sqrt{s} = 200$ GeV had an integrated luminosity of 7.9pb^{-1} [4], Run 7 Au+Au with $\sqrt{s_{NN}} = 200$ GeV had an integrated luminosity of $\sim 300 \mu\text{b}^{-1}$ [66, 67, 68] and Run 10 Au+Au with $\sqrt{s_{NN}} = 200$ GeV had an integrated luminosity of $\sim 1400 \mu\text{b}^{-1}$.

3.1 STAR

The Solenoidal Tracker at RHIC (STAR) is a large acceptance experiment that is designed to focus on interesting physics at midrapidity. STAR has many different

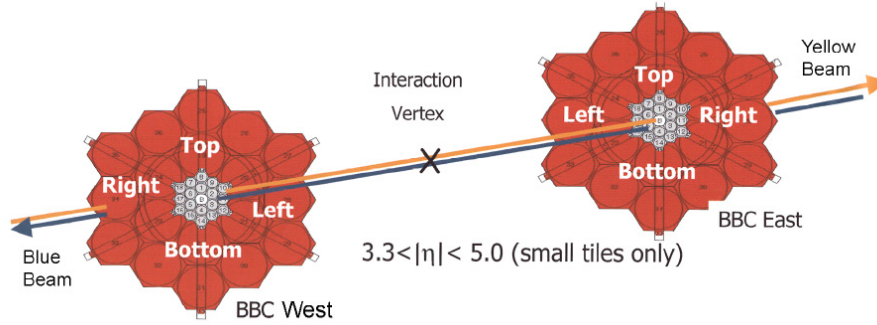


Figure 3.1. Schematic of STAR’s BBC East and BBC West. [22]

detectors. Those that were used for the analyses presented in this thesis are: the Time Projection Chamber (TPC) [24], the Barrel Electromagnetic Calorimeter (BEMC) [23], the Vertex Position Detector (VPD) [69], and the Beam-Beam Counter (BBC) [70]. These will be described in more detail in the following sections.

3.2 Beam-Beam Counter

The Beam-Beam Counter (BBC) is a scintillator detector that can be found 3.75 m from the center of the STAR detector on both the east and west sides of STAR. The center is defined at $z = 0$, where the z -axis is defined by the magnetic field. The BBC has an inner ring and an outer ring with different sized tiles on them, which can be seen in Figure 3.1. For our analysis, we used the 18 inner tile pieces as the basis of our minimum bias $p + p$ trigger. The pseudorapidity coverage (η) of these inner tiles is $3.4 < |\eta| < 5.0$. The signals from the tiles are sent down a fiber optic cable to magnetically-shielded photomultiplier tubes (PMTs) for readout [22, 70]

The STAR $p + p$ minimum-bias trigger requires an East-West coincidence in the BBCs as this indicates that a collision has occurred near the center of the detector.

In simulated studies of the the BBC acceptance and efficiency it was found that the BBC efficiency was $87 \pm 8\%$ for non-singly diffractive (NSD) collisions. The absolute cross section seen by the BBC trigger was measured via a van der Meer scan to be 26.1 ± 0.2 (stat.) ± 1.8 mb (sys.) [71]. The uncertainty in the BBC cross section is one of the dominant uncertainties in the Υ cross section measurement.

3.3 Vertex Position Detector

Two Vertex Position Detectors (VPDs) are located on the East and West sides of STAR a distance of 5.6 m from $z = 0$. The VPD detectors use photomultiplier tubes to determine the start time of a collision. An East-West VPD coincidence is required for minimum-bias Au+Au events. The VPD can be used to determine the location along the z -axis where the collision that fired the VPD took place. This location is called the vertex location, with the z position being given the label V_z . The VPD can not determine V_x or V_y . The V_z from the VPD can be used in conjunction with the TPC to select in-time events [69].

3.4 Barrel Electromagnetic Calorimeter

The last of the STAR trigger detectors used in this analysis is the Electromagnetic Calorimeter (BEMC). It is a lead and plastic scintillator sampling calorimeter with a full 2π azimuthal coverage and $|\eta| < 1$ on the outside of the Time Projection Chamber (TPC) as shown in Figure 3.2. The scintillation light is read out by PMTs. At the

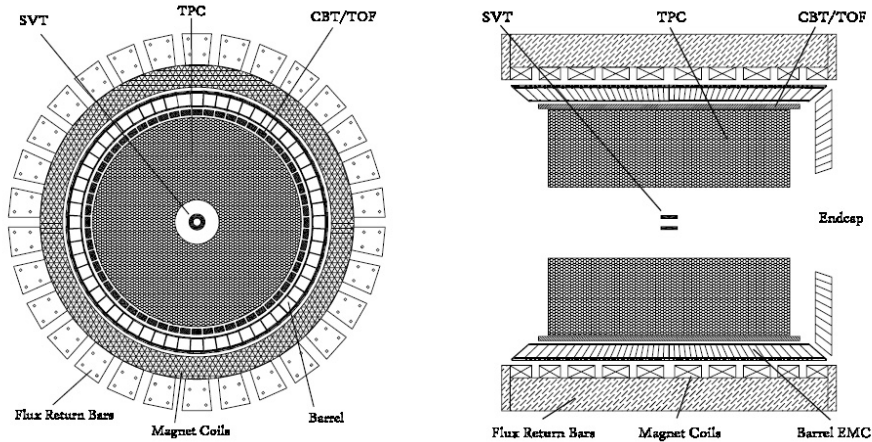


Figure 3.2. STAR's BEMC shown with the magnet and the TPC. The SVT in the center was removed after 2007. [23]

center of the BEMC ($\eta = 0$) the depth is 20 radiation lengths, which allows the BEMC to contain a 60 GeV electromagnetic shower. The BEMC is divided into 4800 towers that each subtend an area of 0.05 in $\Delta\eta$ and 0.05 in $\Delta\phi$ and point to the center of the detector. This can be seen in Figure 3.2. Each tower contains 20 layers of lead and 19 layers of plastic scintillator [23]. The energy resolution of the BEMC is $dE/E \sim \frac{14\%}{\sqrt{E}}$ plus a constant 1.5% term that needs to be added in quadrature. At 4.5 GeV this works out to a resolution of about 7%.

The BEMC is fast enough to trigger on every bunch crossing in RHIC, which is important for the Υ analysis as this allows us to sample the entire integrated luminosity. It uses 12-bit flash Analog to Digital Converters (ADCs) to trigger on high p_T electromagnetic signals. The BEMC can make a decision within $\sim 1\mu\text{s}$, to determine whether the TPC should be read out for the collision in question. The BEMC can trigger on the signal in a single tower, or it can trigger on the total signal in a patch of 4×4 towers called a jet patch. These patches are hard-wired into the

BEMC [23]. The jet patches were used for the run 6 Υ cross section measurement, but they were not used for any Υ analysis after that, including both the 2007 and 2010 Au+Au analyses discussed in this thesis.

In addition to firing a trigger, the BEMC can be used in Particle Identification (PID) in conjunction with the TPC. An electron should deposit its full energy into the BEMC, so the ratio of E/p where E is measured by the BEMC and p is measured by the TPC should be close to 1. A hadron will not leave its full energy in the BEMC, so it should have an E/p ratio considerably less than 1. The ratio E/p is used rather than the inverse as E and $1/p$ are both gaussian quantities. They are gaussian because the BEMC measures E and the TPC measures the track curvature, which is proportional to $1/p_T$, thus multiplying them together is a gaussian quantity. Further detail on how to use E/p for PID can be found in Section 4.3.2.

3.5 Time Projection Chamber

The STAR Time Projection Chamber (TPC), shown in Figure 3.3, is the heart of the STAR detector. It is 4.2 m long and the outer diameter of the drift volume is 4.0 m, which made it the largest TPC in the world until the construction of the ALICE TPC at the Large Hadron Collider. It fits inside STAR's 0.5 T solenoidal magnet. [24] Like the BEMC, the TPC has full azimuthal coverage and can track particles with $|\eta| < 1.8$. The TPC is used to measure the momentum of particles from 100 MeV/ c to over 30 GeV/ c and assists in PID by measuring the ionization energy loss (dE/dx).

At the center of the TPC there is a conductive Central Membrane (CM) which holds the high voltage necessary for the electric field. The CM, along with the concentric field-cage cylinders and the end caps creates a uniform electric field, which is necessary to precisely reconstruct the tracks. The entire TPC is filled with P10 gas, which is 10% methane and 90% argon during operation. When the TPC is not in use, it is filled with Nitrogen gas. High momentum particles leave an ionization trail within this gas, which drifts away from the CM to the read outs on either end cap. The TPC read-out is a Multi-Wire Proportional Chamber (MWPC). Each MWPC has 3 wire planes: the anode, the ground and the gating grid as well as the pad plane. There are 12 sectors in each end cap, with differing designs for the inner and outer sections as shown in Figure 3.4. The inner section, where the track density is highest, is optimized for good two-hit resolution by using smaller pads. The outer section is optimized for dE/dx resolution by having a continuous pad coverage, including no space between the pad rows. The outer section has 32 pad rows and the inner section has 13, which means a given track can have as many as 45 hits [24].

Tracks in the TPC are reconstructed by finding ionization clusters along the track. The x , y coordinates are reconstructed by the MWPC. The z coordinate is determined based on the time it takes for a particular cluster to reach the TPC read-out. The rate at which the ionization tracks flow to the end cap is determined by using lasers to form ionization tracks at specific locations in the TPC. The drift velocity is known to 0.1% precision. More specifically, the x (or y) position is determined by fitting the charge distribution across several pads assuming a gaussian pad response function [24].

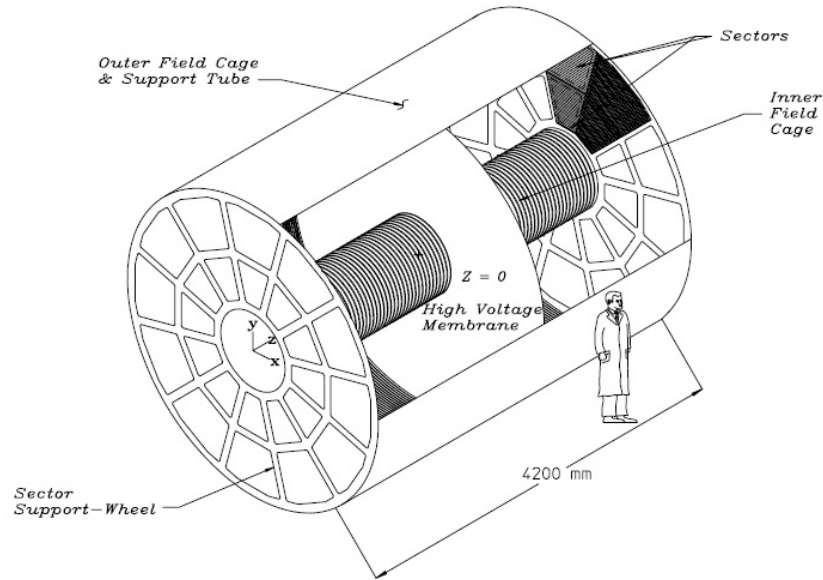


Figure 3.3. STAR TPC shown with a person for comparison [24]. The high voltage membrane is the plane that defines $z = 0$.

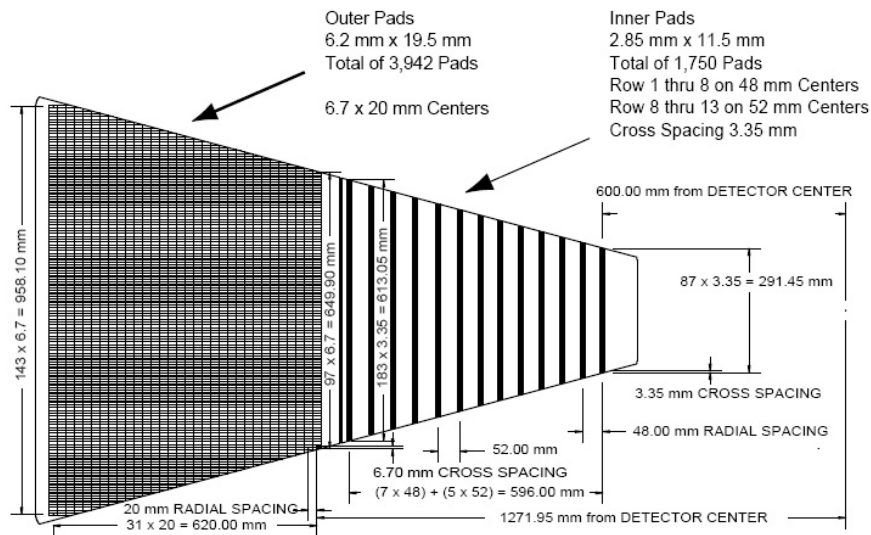


Figure 3.4. One TPC sector[24], of which there are 24. This schematic shows the differing schemes for the inner section and outer section.

3.5.1 Track Reconstruction

Another important aspect of reconstructing tracks within the TPC is the tracking software. This software uses a track model to fit the distribution of reconstructed

ionization clusters and determine a complete track structure. This allows us to determine the momentum from the track parameters, as well as the ionization energy loss. A charged particle moving in a solenoidal field would move in a helix. However, due to energy loss, tracks in the TPC deviate slightly from a helical path. Tracking starts at the outer pad rows where the hit density is lowest. This makes it easier to find a track seed. Track seeds are found using a Kalman filter approach and have at least 3 hits that are close in space [72]. Once a track seed is found, it is fit with a straight line that is extrapolated inward in order to find additional hits belonging to the same track segment. If additional hits are found, the resulting track segment is fit with a helix. The Kalman finder then uses the helix to find additional hits in the TPC [72]. Basically the Kalman fit proceeds inwards, adding hits if they lie within the radius determined by the error parameter of the helix. After a hit is added, the track segment is refit to refine the track parameters. Track segments are merged together if they appear to be the result of track splitting. All tracks are required to have hits on at least 10 pad rows because shorter tracks are probably just fragments of a longer track that was not successfully reconstructed. Once the track fit is complete, each event has a collection of global tracks.

3.5.2 Vertex Reconstruction

The collection of global tracks is then used to determine the vertex location. The vertex is the place in space where the collision that produced the charged particles that left the tracks occurred. STAR has two vertexing algorithms, MinuitVF and PPV,

that are used for $A+A$ collisions and $p+p$ collisions respectively. Both algorithms follow a very similar procedure. From the collection of global tracks, they find seed locations for the z position of the vertex based on the z positions of the tracks' distance of closest approach (DCA) to the beamline. Then the DCAs of the collection of tracks to the vertex are minimized. Both algorithms discard tracks that have DCAs > 3 cm from the vertex location so that the fit is not driven by outliers that could not come from the collision of interest. Then the vertices are ranked based on how many of their tracks can be associated with signals in faster detectors, such as the BEMC. This is necessary because the TPC is much slower than the collision rate, so in each recorded event there are a number of tracks that come from collisions that occurred before and after the collision that fired the trigger [73]. Once the vertex is found, the tracks associated with that vertex have the vertex position added as an additional point to their collection of hits. The tracks are then refit, and the refit version of these tracks are called primary tracks. This allows improved momentum resolution because the hit resolution at the full magnetic field strength of 0.5 T is ~ 2 mm [24], but the vertex location can be known more precisely than any hit in the TPC. The vertex resolution is dependent on the number of tracks used to find its location. For vertices with 1000 tracks the resolution is $350 \mu\text{m}$ [73].

Chapter 4

Υ in $p+p$ collisions at $\sqrt{s} = 200$ GeV

4.1 Data Set and QA

An important part of determining the effect of the hot matter formed in heavy ion collisions on the Υ is a measurement of the cross section in $p+p$ collisions. The data here is from the 2006 RHIC run, produced using a STAR specific Υ trigger. Ideally we would determine the cross section of the three Υ states independently. However, at the this time, the combination of the limited statistics and the resolution of the detectors made this impossible. So the cross section from this data set is for mid-rapidity $\Upsilon(1S + 2S + 3S)$ in the dielectron channel.

4.2 STAR Υ Trigger

A specific trigger for the Υ was necessary in order to sample the entire integrated luminosity available. This trigger had two stages, a Level-0 (L0) hardware stage [74] with a decision time of $\sim 1\mu s$, and a Level-2 (L2) software stage with a decision time of $\sim 100\ \mu s$ in $p+p$ collisions (this increases to $\sim 400\ \mu s$ in Au+Au). This particular data set had two different triggers, which we label as Trigger I and Trigger II, that only differed in their thresholds. An increase in the threshold was needed to reduce the trigger rate and reduce the deadtime of the TPC during the run. The parameters for these triggers were based on simulations and on expected trigger rates from calorimeter data taken in 2003.

Υ L0 Trigger

The L0 part of the Υ trigger is the combination of a minimum-bias $p+p$ trigger and a signal in the BEMC consistent with a high energy electron or positron. A L0 decision can be made every single bunch crossing. The signal in the BEMC was evaluated based on two quantities. One was based on the read out from a single tower, the other is based on the signals from a group of towers containing a single tower with a signal above the relevant threshold. This tower is called a “High Tower” and we give it the label HT. The group of towers is a sum of towers in fixed η - φ regions of the BEMC, where each region comprises 4×4 towers. Each of these regions is called a “Trigger Patch” which we label as TP. Since each tower covers 0.05 units in η and 0.05 radians in φ , the TP coverage is 0.2×0.2 radian.

The signal from each tower is digitized and then a background pedestal is subtracted from it. This signal is sent to the L0 Data Storage and Manipulation (DSM) hardware at a 6-bit ADC value. The calibration of the BEMC is done so that these DSM-ADC values from the BEMC towers are proportional to the transverse electromagnetic energy (E_{\perp}). The Υ L0 trigger conditions for Trigger I (Trigger II) are that at least one tower has a DSM-ADC value > 12 (16) which is approximately an E_{\perp} of 2.6 (3.5) GeV and that the Trigger Patch containing that tower has a total DSM-ADC sum > 17 (19) which is approximately an E_{\perp} of 3.8 (4.3) GeV. For both of these triggers, the minimum bias condition based on a BBC coincidence as described in Chapter 2, is required. The combination of a tower and trigger patch that satisfied the trigger conditions will be given the label HTTP [4].

Figure 4.1 shows the p_T distribution for electrons and positrons from simulated Υ s in which both daughters fall within the STAR acceptance. For each decay, we plot the p_T distribution of the daughter with the highest p_T as this is the distribution important for firing the L0 trigger. The distributions for the electron and positron daughters are identical, which is expected given that they only differ by charge. The sum of these two distributions is also shown as a black histogram. Since the L0 trigger measures E_{\perp} and not p_T the corresponding DSM-ADC values are shown in Figure 4.2. In this figure, the L0 HT Trigger II threshold of 16 is shown by the vertical dashed line.

From the p_T and ADC distributions for the Υ daughter with the highest E_T in Figs. 4.1 and 4.2, the average values are $\langle p_T \rangle = 5.6$ GeV/c and $\langle \text{ADC} \rangle = 18.0$ counts. Since the trigger threshold is placed at 16 ADC counts, the hardest daughter will

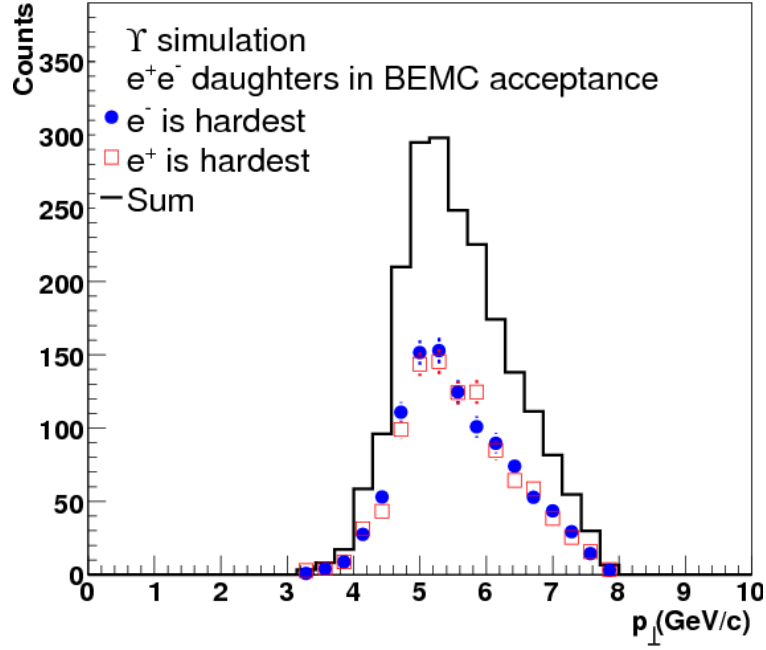


Figure 4.1. The p_T distribution for simulated Υ daughter electrons in filled circles and positrons in open squares, with the highest p_T . Only those daughters with a parent Υ which falls in the STAR BEMC geometrical acceptance are shown. The solid histogram is the sum of the two distributions [4].

typically fire the trigger. We find that 25% of the Υ 's produced at midrapidity have both daughters in the BEMC acceptance and at least one of them can fire the L0 trigger. The details of the HTTP trigger efficiency and acceptance are discussed in Sec. 4.2.3.

4.2.1 Υ L2 Trigger

If a collision satisfies the L0 HTTP trigger conditions, and the trigger is issued, the information for all detectors in STAR begins to be digitized. At this time, the software based L2 algorithm can make a decision whether to keep the event as a potential Υ event or not. The L2 system uses information from the calorimeter towers to make the

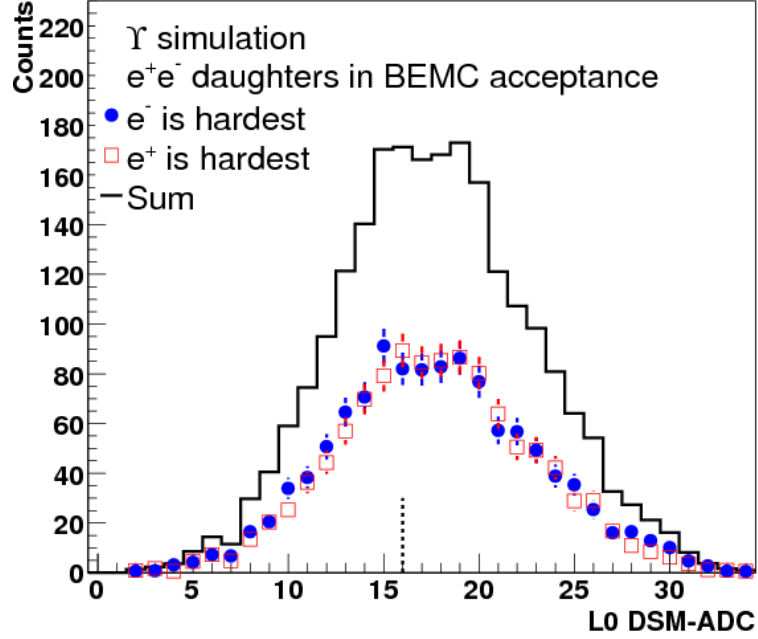


Figure 4.2. The L0 DSM-ADC distribution for simulated Υ daughter electrons (filled circle) or positrons (open square) with the highest ADC. The histogram is the sum. The threshold for Trigger II is shown as a vertical dotted line. [4].

decision. Unlike the L0 trigger, the L2 system has access to the full energy resolution of the calorimeter. The L2 trigger is a topological trigger that looks for a signal in the BEMC consistent with the production of a high invariant mass electron-positron pair. Since the BEMC does not differentiate electrons from positrons, we will refer to both potential Υ daughters as electrons for the purposes of the trigger discussion.

First the algorithm collects all the towers that satisfy the L0 High Tower threshold. Each of these towers is a seed for a 3-tower cluster. The algorithm looks at the 8 neighboring towers of the seed tower (unless the seed tower is on the edge of the calorimeter, in which case it will only have 5 neighbors) and keeps the 2 with the highest energy. Simulations show that this clustering algorithm will contain most of the energy of an electron and will keep the additional background due to the

underlying event in Au+Au events at a minimum. This 3-tower cluster is a more accurate reflection of the energy than the single tower used in the L0 algorithm. If the 3-tower cluster contains greater than 4.0 GeV of energy, it is kept as a seed for the latter part of the algorithm and given the label “L2 Cluster-1”. While it is possible for an event to have multiple clusters that satisfy the L0 threshold and satisfy this additional energy requirement, the vast majority only have a single tower [4].

The next step is to find additional electron candidates in the event. The energy threshold for these candidates is lower than what is required for the L0 candidate. All towers which have $E_{\perp} \gtrsim 0.7$ GeV (10-bit ADC of at least 75 counts after pedestal subtraction) are considered. A 3-tower cluster is constructed in the same manner as for the higher energy daughter. If this cluster has greater than 2.5 GeV, this cluster is also accepted for further consideration and given the label “L2 Cluster-2”.

Next we make all possible cluster pairs, where each pair must have at least one L2 Cluster-1 and calculate two pairwise quantities: the opening angle and the invariant mass. However, only some information is accessible during this time and calculations must be done quickly, so some approximations are made. One is that the vertex associated with the collision that produced the trigger is located at the center of the detector ($z = 0$). Another is that the electrons traveled in a straight line from the vertex to their respective towers. The third assumption is that the electrons are massless. To pass the L2 requirement, we require that a cluster pair have an opening angle (θ) such that $\cos(\theta_{12}^{L2}) < 0.5$ and that the invariant mass is in the range $6 < M_{12}^{L2} < 15$ GeV/ c^2 . A picture of this topological scheme can be seen in Figure 4.3.

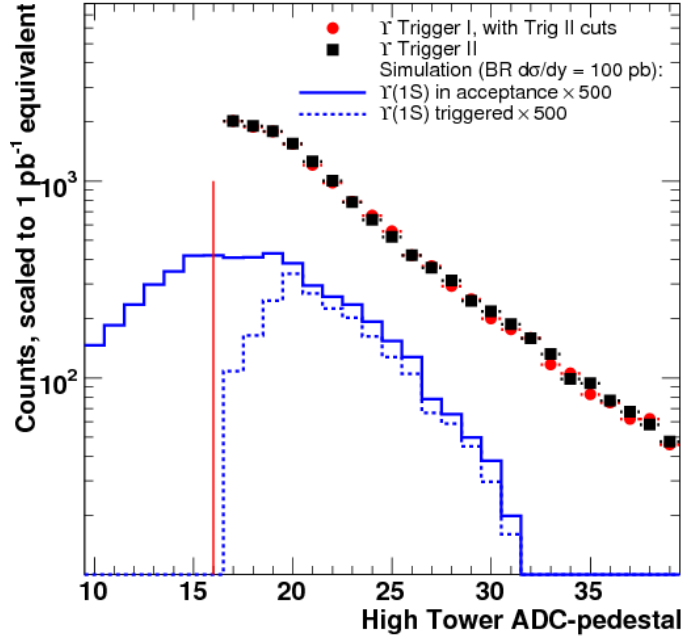


Figure 4.4. The L0 DSM-ADC distribution for the highest BEMC tower of a candidate pair, the same as the black histogram shown in 4.2. We show Trigger I data after applying Trigger II thresholds (red circles) to the data, and Trigger II data (black squares). All yields are normalized by the integrated luminosity. The blue histograms are the distributions of the daughters from simulated $\Upsilon(1S)$ that have passed acceptance. The dotted line has the additional requirement that it has passed both L0 trigger requirements. The simulation histograms are normalized assuming $\text{BR} \times d\sigma/dy = 100$ pb times a factor of 500. The threshold for Trigger II is shown as a vertical solid line. [4].

uncertainty is due to the uncertainty in the BBC measurement of the cross section as determined by a van der Meer scan explained in section 3.2 [71].

Figure 4.4 shows the ADC distribution of the tower with the largest E_{\perp} for each candidate pair seen at the trigger level in an even. The two triggered data sets are shown, with Trigger II displayed as squares and Trigger I, with Trigger II requirements applied, displayed as circles. The rejection factor is defined as the number of minimum-bias events divided by the number of events where the trigger was issued was found to be 1.8×10^5 for Trigger II. The trigger rate for the Υ trigger is

deominated by background events with back-to-back π^0 s as no tracking or PID information is available at the trigger level, and the cross section for these back-to-back π^0 s greatly exceeds that of the Υ . The trigger distributions are scaled by their integrated luminosity in order to compare the relative normalization of the two data sets. The scale is chosen such that the counts in each triggered data set correspond to an integrated luminosity of 1 pb^{-1} . The relative luminosity normalization between the datasets agrees to a level of $\approx 1\%$. The solid and dotted lines come from simulated and accepted $\Upsilon(1S)$ where an accepted Υ is defined as one where both electron daughters have left at least 1 GeV of energy in the BEMC. The dashed line has the additional Trigger II requirements applied to it. The vertical line at 16 ADC counts represents the L0 ADC high tower threshold for Trigger II. The simulated Υ signal is also scaled to an integrated luminosity of 1 pb^{-1} assuming a cross section times branching ratio into e^+e^- for the $\Upsilon(1S)$ at midrapidity of 100 pb, which is the right order of magnitude. The simulated $\Upsilon(1S)$ distributions were then multiplied by a factor of 500 for display purposes. Based on our estimate of the Υ cross section and the integrated luminosity, we expect only one Υ for every ~ 3000 triggers. This means that the shape of the data in Fig. 4.4 is therefore dominated by this π^0 background. The same normalization and scale factors are used in Figs. 4.5–4.6 for comparing the trigger-level background distributions and the expected $\Upsilon(1S)$ signal [4].

The distribution of the L2 Cluster-1 energy for all clusters that include a tower above the HT DSM-ADC threshold of 16 ADC and that have their corresponding Trigger Patch DSM-ADC sum above the threshold of 19 ADC counts are shown in Figure 4.5. The TP and HT requirements are the reason the peak of the L2 Cluster-1

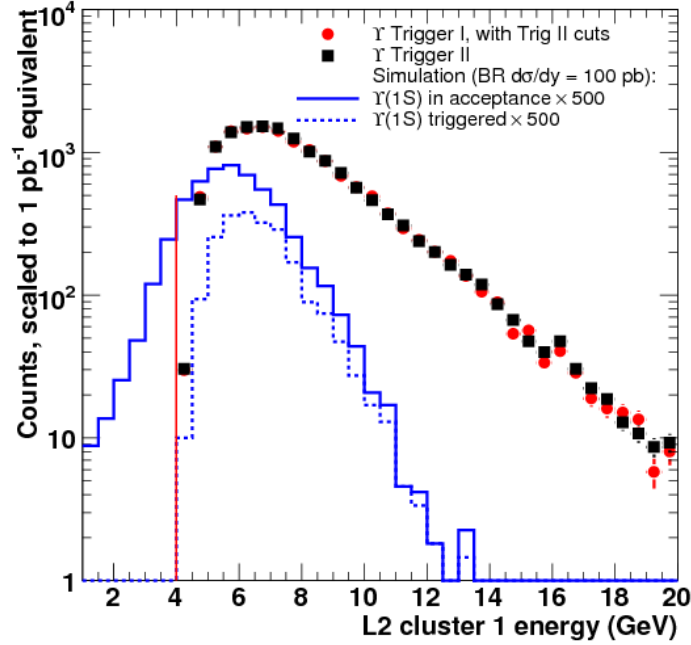


Figure 4.5. The L2 Cluster-1 energy distribution (EL21) for all towers above the HT threshold in a trigger patch above the TP threshold. The L2 trigger requires EL21 \geq 4.0 GeV. The solid-line histogram shows the accepted Upsilon (from simulation) after acceptance requirements, while the spectrum shown by the dashed-line includes all trigger requirements. Normalization and scaling factors are done as for Fig. 3.[4].

is not at the threshold of 4 GeV. Some clusters with energy $>$ 4 GeV do not satisfy the L0 requirements, and thus are removed from the distribution [4].

In Figure 4.7, the L2 opening angle can be seen. It is peaked towards a back-to-back topology, much more so than the distributions from the simulated $\Upsilon(1S)$'s. This is also due to the fact that the majority of this distribution comes from back-to-back π^0 's. Most of these background events are rejected when an electron track in the TPC is required to be associated with a given cluster [4].

The L2 invariant mass distribution shown in Fig. 4.6 is peaked at ≈ 8 GeV/c^2 due to the cluster energy requirements. The vertical lines depict the lower and upper thresholds at 6 and 15 GeV/c^2 , respectively. As before, the solid line is from a scaled

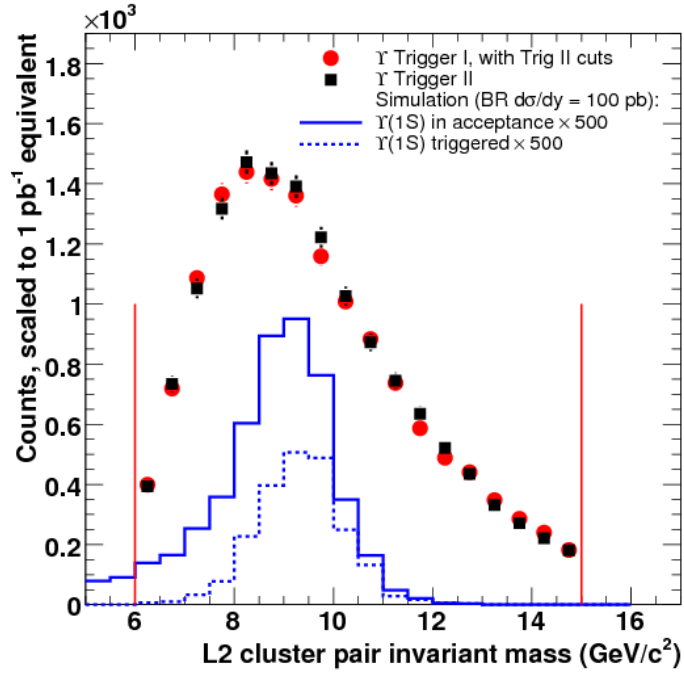


Figure 4.6. The L2 invariant mass M_{L2}^{12} distribution for accepted events. The histogram shows the M_{L2}^{12} distribution for simulated $\Upsilon(1S)$ s after acceptance, L0 trigger, L2 cluster and L2 opening angle selection on the e^+e^- daughters. Vertical lines show location of the trigger thresholds. Normalization and scaling factors are done as for Fig. 3 [4].

simulation of accepted $\Upsilon(1S)$'s and the dashed line is from those that have passed the Trigger II requirements [4]. The L2 invariant mass resolution at the Υ mass is calculated from the simulation to be 849 ± 8 MeV/ c^2 . The main contributions are the energy resolution in the BEMC and the straight line approximation used to calculate the opening angle of the energy clusters. This is about an order of magnitude larger than the offline resolution calculated from the daughter momentum as measured in the TPC. The L2 invariant mass requirement mainly serves to reject background. In addition, the L2 information (such as that shown in Figs. 4.5–4.6) is available online after every run, which serves as a useful diagnostic tool.

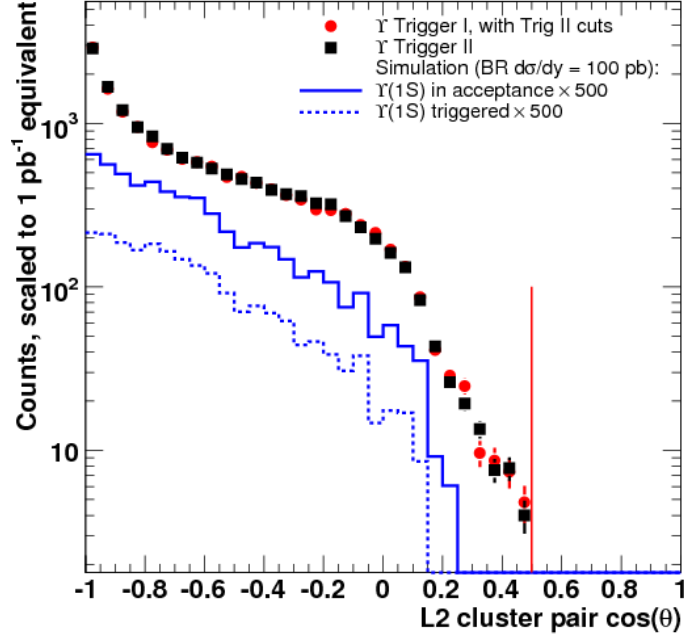


Figure 4.7. The cosine of the L2 opening angle L212 distribution for accepted events. The histogram shows the distribution for simulated Upsilon after acceptance, L0 trigger and L2 Cluster selection. The vertical line shows the location of the trigger threshold. Normalization and scaling factors are done as for Fig. 3. [4].

4.2.3 Υ Acceptance and Trigger Efficiency

To calculate the geometrical acceptance and the efficiency for measuring $\Upsilon \rightarrow e^+e^-$ at STAR, we combined two different types of events. The first type of event was a GEANT simulation of $\Upsilon \rightarrow e^+e^-$. This was then propagated through the detector geometry. The simulations were done with uniform population of the p_T - y phase space in order to insure that all the Υ phase space that would be measured in this analysis had a very small statistical error bar from simulation. The distributions were then weighted with a Gaussian in y ($\sigma = 1$) and a realistic p_T distribution. We chose the form $dN/dp_T \propto p_T/(\exp(p_T/T) + 1)$ with the parameter $T = 2.2$ GeV/ c obtained from a fit to CDF data [75]. The dependence of the acceptance on p_T was

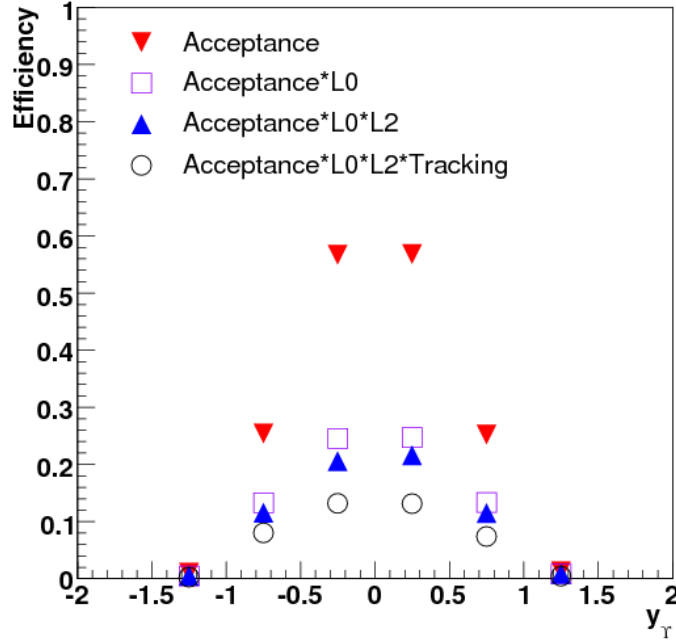


Figure 4.8. Combined acceptance efficiency as a function of rapidity y_{Υ} for the decay $\Upsilon \rightarrow e^+e^-$ in STAR. Circles: BEMC acceptance only; squares: adding L0 requirement; upright triangles: adding L2 requirement; down triangles: adding TPC acceptance+TPC tracking cuts and TPC-BEMC matching. [4].

negligible, which indicates that our choice of p_T functional form does not introduce much in the way of systematic uncertainty. This was verified by using function forms derived from data at lower energies. The simulated Υ decay was then combined with a $p + p$ minimum-bias PYTHIA event [76] with CDF Tune A settings [77].

The second type of event was a data set of triggers called "zero bias". These events do not require signals in any of the STAR detectors, they only require a beam coincidence. These events do not always have a collision, but include all the effects from pile-up and detector noise. The simulated events were combined with these zero-bias events to give a realistic environment in which to study the acceptance and efficiency. The PYTHIA+ Υ was embedded into the zero-bias event with a vertex

position that was sampled from a realistic distribution of the vertex positions obtained from the Υ triggered data.

We defined an accepted simulated Υ] as one where each of its decay electrons deposited at least 1 GeV in the BEMC, as simulated by GEANT. We find that the acceptance depends strongly on the Υ rapidity (y_Υ), but weakly on its transverse momentum ($p_{T\Upsilon}$). At $|y_\Upsilon| < 0.5$, the acceptance is 57%, dropping to below 30% beyond $|y_\Upsilon| = 0.5$, and is nearly zero beyond $|y_\Upsilon| = 1.0$. This distribution is shown in Fig. 4.8 where the downward triangles depict the geometrical acceptance of the BEMC detector ϵ_{geo} obtained from the analysis of the simulated Υ decays in the zero-bias data events.

For the accepted, simulated Υ 's, we calculate the trigger efficiency based on Trigger II thresholds. This required simulations of the BEMC response and digitization. The resulting simulation also had to be run through the software reconstruction chain. The L0 and L2 trigger efficiencies multiplied by the acceptance can be seen in Figure 4.8. The squares include the effect of the L0 HTTP trigger requirement, ϵ_{L0} , and the upright triangles include the L2 trigger condition, ϵ_{L2} . The open circles include TPC acceptance plus tracking efficiency, ϵ_{track} , and TPC-BEMC matching, ϵ_R . These selections, as well as the PID cuts, and the matching of TPC tracks to triggered clusters in the BEMC, are discussed in Sec. 4.3. For the region $|y_\Upsilon| < 0.5$, the acceptance and efficiencies are given in Table 4.1.

The relative systematic uncertainty on the L0 HT trigger efficiency was estimated to be $^{+5.9\%}_{-7.5\%}$. This is the dominant source of systematic uncertainty of the Υ trigger efficiency. It is asymmetric because the underlying E_\perp distribution of the daughter

Table 4.1. Acceptance, trigger efficiency, and tracking efficiency for reconstructing $\Upsilon \rightarrow e^+e^-$ in STAR in the kinematic region $|y_\Upsilon| < 0.5$. The first 4 rows are for the 1S and the last row is for the cross section-weighted 1S+2S+3S combination. All systematic uncertainties are listed in Table 6.1.2.

Quantity	Value
ϵ_{geo}	0.57
$\epsilon_{\text{geo}} \times \epsilon_{\text{L0}}$	0.25
$\epsilon_{\text{geo}} \times \epsilon_{\text{L0}} \times \epsilon_{\text{L2}}$	0.21
$\epsilon_{\text{geo}} \times \epsilon_{\text{L0}} \times \epsilon_{\text{L2}} \times \epsilon_{\text{track}} \times \epsilon_R$	0.13
$\epsilon_{\text{geo}} \times \epsilon_{\text{L0}} \times \epsilon_{\text{L2}} \times \epsilon_{\text{track}} \times \epsilon_R$ (1S+2S+3S)	0.14

electrons is not flat at the threshold, as shown in Figure 4.2. After including the L2 trigger, tracking, and TPC-BEMC matching efficiencies, we obtain a combined efficiency of 13.2% for the $\Upsilon(1S)$.

We repeated the procedure for the $\Upsilon(2S)$ and $\Upsilon(3S)$ states, which have slightly higher trigger efficiencies due to their larger masses. To find the total efficiency of the $\Upsilon(1S + 2S + 3S)$, we calculated a weighted average among the 3 states, including the branching ratio to electrons and the ratio of cross sections. We used the PDG values of the branching ratios [30], and the cross section ratios from a NLO CEM pQCD calculation which used a bottom quark mass of $m_b = 4.75$ GeV/ c^2 . The PDFs used are MRST HO [31], the choice of scale was $\mu = m_T$, and the center-of-mass energy was $\sqrt{s} = 200$ GeV [32]. The branching ratios and cross sections we used for this purpose are shown in Table 4.2.

The combined acceptance, trigger efficiency, track finding efficiency, and TPC-BEMC matching efficiency is 14.3% for the averaged $\Upsilon(1S + 2S + 3S)$ combination, as shown in the last row of Table 4.1. To determine the systematic uncertainty in the efficiency due to the averaging procedure, we varied the values in Table 4.2 in

Table 4.2. Branching fractions for $\Upsilon(nS) \rightarrow e^+e^-$ [30] and total cross sections at $\sqrt{s} = 200$ GeV from an NLO CEM model [31].

Υ state	\mathcal{B} (%)	σ (nb)
$\Upsilon(1S)$	2.38 ± 0.11	6.60
$\Upsilon(2S)$	1.91 ± 0.16	2.18
$\Upsilon(3S)$	2.18 ± 0.21	1.32

two ways. When we vary the branching ratios by their uncertainty, we find that the efficiency varies from 14.2–14.4%. If instead of using the values listed in Table 4.2, we use the measured values of the ratios $\Upsilon(2S)/\Upsilon(1S)$ and $\Upsilon(3S)/\Upsilon(1S)$ from Ref. [78] and vary these measured ratios within their uncertainty, we obtain weighted efficiencies in the range 14.1–14.4%. This means that the overall scale of the cross section from the NLO calculations introduces very little systematic uncertainty in our results.

The hadron rejection power of the BEMC towers at the energy threshold of ~ 4 GeV is approximately 100 [4]. The main source of the trigger background comes from high- p_T π^0 's decaying into two photons. These photons then deposit energy in the BEMC. If the opening angle between them is large enough, the Υ trigger will fire. These events are typically from di-jets. Fortunately these events also have a low cross section so that the trigger rate was sufficiently small for us to sample all of the available integrated luminosity with the Υ trigger. The trigger distributions shown in Figures 4.4–4.7 are dominated by this $\pi^0 \rightarrow \gamma\gamma$ background [4], as shown by the scaling necessary to put the data and the Υ simulated yield on the same graph. These background events are rejected in the offline analysis.

4.3 Υ Analysis

4.3.1 Track Selection

During the offline analysis, we select any pair of the energy clusters in the BEMC that could have fired the Υ trigger to create a list of trigger candidates. Since the energy threshold for the L2 tower requirement is low (< 1 GeV) it is possible for two or more towers that have an energy higher than this threshold to be next to each other in the BEMC. The clustering algorithm may then create two separate clusters that contain both of these towers, which means that the clusters really are identical. This was solved by removing the lower energy tower from consideration whenever two such towers are next to each other.

Once the triggered energy cluster pairs are selected, charged tracks in the TPC are used to select those cluster pairs that likely came from a dielectron. First we require that all tracks point close in η - φ to the position of the candidate clusters. The ionization energy loss in the TPC is used to help select those tracks which came from electrons. Also, the momentum calculated from the TPC track, and the energy from the three tower clusters are also used to help with electron identification by calculating the ratio E/p .

The tracks in the TPC are selected based on a number of parameters. They were required to have at least 20 space points (out of a possible 45). We also required them to have at least 52% of their possible space points. This guarantees that we have no split tracks without throwing out those tracks that could not have 45 space points due to passing through inactive areas of the TPC. We also only selected those

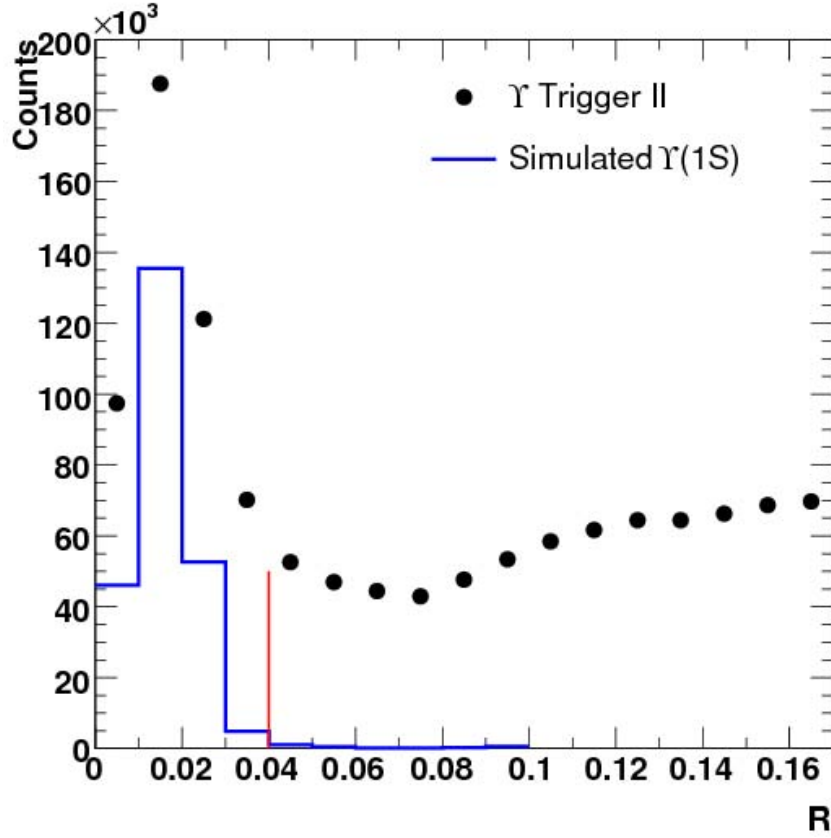


Figure 4.9. The line histogram shows the η - φ radial distance $R = \sqrt{\Delta\eta^2 + \Delta\phi^2}$ between the TPC track and the 3-tower BEMC electron cluster for simulated Υ daughters. The black squares show this distribution from data. We reject candidate tracks with $R > 0.04$ [4].

tracks with $p_T > 0.2$ GeV/ c . An additional cut on momentum is indirectly imposed by the combination of the energy cluster threshold and the E/p requirement. We only use those tracks which extrapolate to a primary vertex, and candidate track pairs must come from the same vertex. We find the combined TPC acceptance times tracking efficiency for detecting each Υ daughter to be $\epsilon_{\text{TPC}} = 85\%$ [4]. This value is approximately independent of electron p_T , which means that the pairwise efficiency can be obtained by squaring the single particle efficiency.

In order to match tracks to the BEMC, we require them to be within a circle of

radius $R < 0.04$ in η - φ space of the L2 candidate clusters. This guarantees that the analysis only uses tracks that could have fired the trigger. This cut has an efficiency of $\epsilon_R = 93\%$ for a given Υ daughter electron and has good background rejection, as shown in Figure. 4.9. The R distribution for simulated $\Upsilon(1S)$ daughters is given by the histogram. The R distribution from tracks passing basic quality cuts in the triggered events is shown as the solid circles.

Another important part of the analysis is the vertex-finding efficiency. The Υ -triggered events have a high vertex-finding efficiency compared to minimum-bias $p + p$ events. The efficiency is higher due to the presence of the HT trigger because these events are likely to have a high- p_T track which increase the probability that a vertex will be found. We find that the vertex-finding efficiency ϵ_{vertex} for Υ events is $96.4 \pm 0.9\%$ [4]. In this run the luminosity was high enough that in $\sim 9\%$ of all Υ -triggered events there were multiple vertices reconstructed. In this analysis, we examined candidates from every vertex in an event. We only selected those vertices that had a pair of TPC tracks that extrapolated to BEMC clusters as outlined above. Since the BEMC is read out every bunch crossing, as stated in Chapter 3, this allows us to reject those vertices from out-of-time pile-up. With this vertex selection criteria, there were no events with candidates from multiple vertices.

4.3.2 PID

Electrons were selected by requiring TPC tracks to have ionization energy losses (dE/dx) consistent with what is expected for electrons. In order to remove the

charged pions from the electron sample, a cut was placed on dE/dx . The cut was chosen to optimize the effective signal S_{eff} of single electrons, $S_{\text{eff}} = S/((2B/S) + 1)$, where S is the electron signal and B is the hadron background. To do this, we constructed a normal distribution of ionization energy loss measurements. This was done by comparing the ionization energy loss of each track to the expected value for an electron and dividing this quantity by the dE/dx resolution. This yields a normalized Gaussian distribution of ionization energy loss measurements, called $n\sigma_{\text{electron}}$. This distribution was fit with three Gaussians, one to represent the electrons and the other two to model the background from pions and other hadrons. The chosen cut yielded an electron efficiency of $\epsilon_{dE/dx} = 84\%$ [4].

In addition to dE/dx , we used the combined information of the BEMC cluster energy E , as obtained by the 3-tower candidate clusters from L2, and the TPC track momentum p to compute the E/p ratio, which should be unity for ultra-relativistic electrons to a very good approximation.

In Figure 4.10, we show the E/p distribution from a positron sample selected via dE/dx in a particular energy window. To select electrons (positrons) cuts were placed at $E/p = 1.0 \pm 0.3$, which is close to a 2σ cut, given that fitting this distribution with a Gaussian gives $\sigma = 0.157 \pm 0.002$. It was expected that E/p be approximately Gaussian due to the Gaussian shape of the resolution in both the energy measurement done in the BEMC and in the curvature measurement done in the TPC. Recall from Chapter 3 that curvature is proportional to $1/p_T$. The E/p distribution from data shows a non-Gaussian tail that we studied carefully to insure that electron daughters from Υ s could not end up in this distribution.

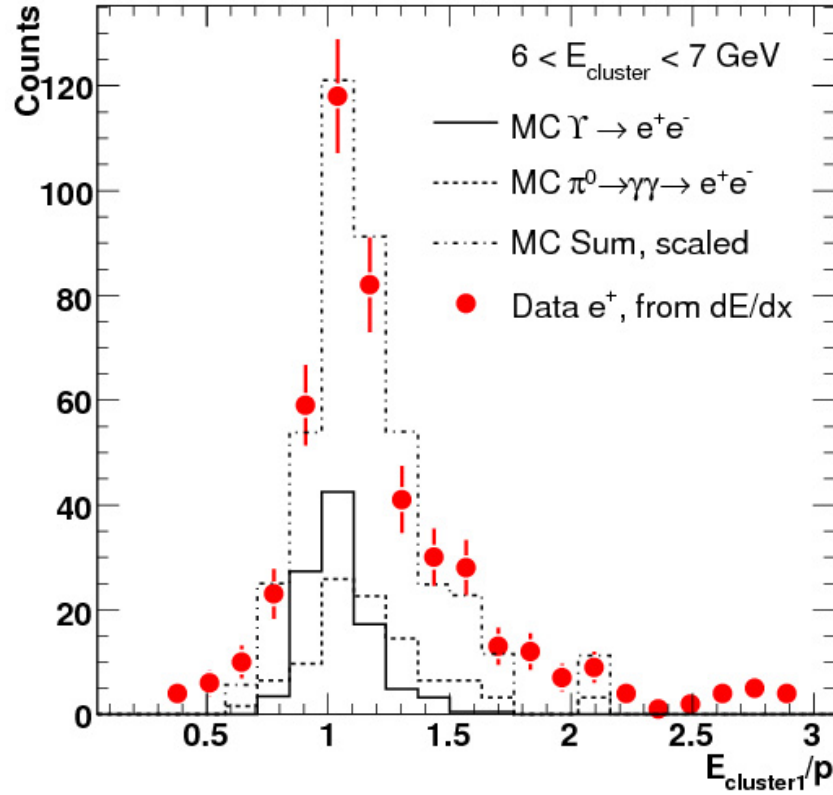


Figure 4.10. The E/p distribution for reconstructed positrons from simulated Υ decays is the dashed line. Positrons selected from Υ triggered data events selected using dE/dx are the red points. The solid line is simulated $\pi^0 \rightarrow \gamma\gamma \rightarrow e^+e^-$ R/p . The dot-dashed line is a fit to the data using a combination of the two simulated distributions [4].

The distribution shown in Figure 4.10 included several selection criteria. One was that we selected positrons rather than electrons in order to avoid antiproton contamination. We also used much tighter dE/dx cuts than were used for the Υ analysis in order to have a very pure sample. We studied an energy window sufficiently above the trigger threshold in order to avoid threshold effects. We made isolation cuts on the positron tracks in order to rule out contamination of the BEMC energy cluster due to near by charged particles. From this analysis, we concluded that the high E/p

tail had two sources: electron bremsstrahlung and photon conversions.

Electron Bremsstrahlung

The solid line in Figure 4.10 shows the simulated E/p for positrons from Υ s combined with a PYTHIA underlying $p + p$ event and embedded into a zero-bias-triggered event as discussed in Section 4.2.3. Many of these positrons produce a Gaussian E/p distribution, but we also see a tail in the E/p distribution. We looked at those simulated particles where the Monte Carlo momentum at the outermost TPC point differs from the momentum at the Υ decay vertex by more than 100 MeV/ c . These are positrons that have undergone Bremsstrahlung. The E/p of these positrons had a mean that was shifted. All entries in the region $E/p \sim 1.3$ of the solid line in Fig. 4.10 come from these cases. This indicates that part of the non-Gaussian shape can be accounted for by positron (electron) bremsstrahlung in the detector material. Electron daughters from Υ will suffer from this physics process.

Photon Conversions

Events with a high Q^2 dijet that include back-to-back π^0 's can also fire the Υ trigger because these π^0 's decay to photons. Some of the π^0 daughter photons will convert into e^+e^- pairs and leave a TPC track that matches with a BEMC cluster which fired the Υ trigger. Generally, the e^+ and e^- will strike the BEMC near their sibling photon. This results in a track with a high E/p value. We analyzed these simulated π^0 events and applied the same tracking cuts, calorimeter clustering, and BEMC-TPC matching used in this paper to the resulting electrons. The resulting

E/p distribution is shown as the dashed line in Figure 4.10. We see a non-Gaussian tail extending to larger values than that of the Υ electrons. The average E/p for the electrons from π^0 events is ≈ 1.18 compared to ≈ 1.08 for Υ electrons [4].

Of these two effects, the first needs to be taken into account in the Υ reconstruction efficiency because the Υ daughters which undergo bremsstrahlung and have a resulting E/p value outside our cut will be removed from the analysis. The second effect does not need to be included in the E/p efficiency since it is not due to Υ events. These events will appear in the dielectron invariant mass spectrum as well, but will be subtracted out with the like-sign pair combinatorial background.

Since the E/p distribution in the Υ -triggered dataset has both types of events, we reproduced the shape of the data using the two types of electron simulations outlined above. These are added and scaled to approximately fit the data in the region $0.6 < E/p < 1.7$, shown as the dot-dashed line in Figure 4.10.

We need to determine the efficiency for selecting electrons only from Υ sources. To do this, we used the Υ embedding simulations to estimate the efficiency of our E/p cut, including both Gaussian and non-Gaussian sources. The systematic uncertainty in this cut is dominated by the uncertainty in our knowledge of the number of radiation lengths of material we have in the inner detector. We estimated that we could be off by a factor of 2, due to the fact that we do not restrict our V_z near $z = 0$ where the material budget is both lower and better known. To estimate this effect, we split our original Υ simulated sample into those electrons that underwent bremsstrahlung and those that did not. We then scaled the former distribution by 2 and added the two back together in order to get a new E/p distribution and then recalculated the

efficiency. The efficiency is $\sim 3\%$ lower in this sample, which we assigned as the systematic uncertainty of $\epsilon_{E/p}$.

All the efficiencies used to obtain the Υ cross section and their systematic uncertainties are collected in Table 6.1.2.

Chapter 5

Υ in Au+Au at 200 GeV

The data for this chapter were taken during the RHIC 2007 heavy ion run at $\sqrt{s_{NN}} = 200$ GeV with the STAR Υ topological trigger (see Section 4.2), and in 2010 with the STAR high tower trigger (See Section 5.2). Much of the analysis technique parallels the technique described in Chapter 4 for the baseline $p + p$ analysis. One difference is that since we do not know the ratio of the $\Upsilon(1S)$ to the $\Upsilon(2S)$ or $\Upsilon(3S)$ we cannot determine an exact line shape for $\Upsilon(1S + 2S + 3S)$. In fact, this is one of the measurements we wish to make. Another difference is that the Silicon Vertex Tracker (SVT) was removed from the center of STAR before the 2008 run so that the number of radiation lengths went from $5.5\%X_0$ to $0.69\%X_0$ [79] at $z = 0$ and $y = 0$. This improves the mass resolution which allows for a better Υ measurement.

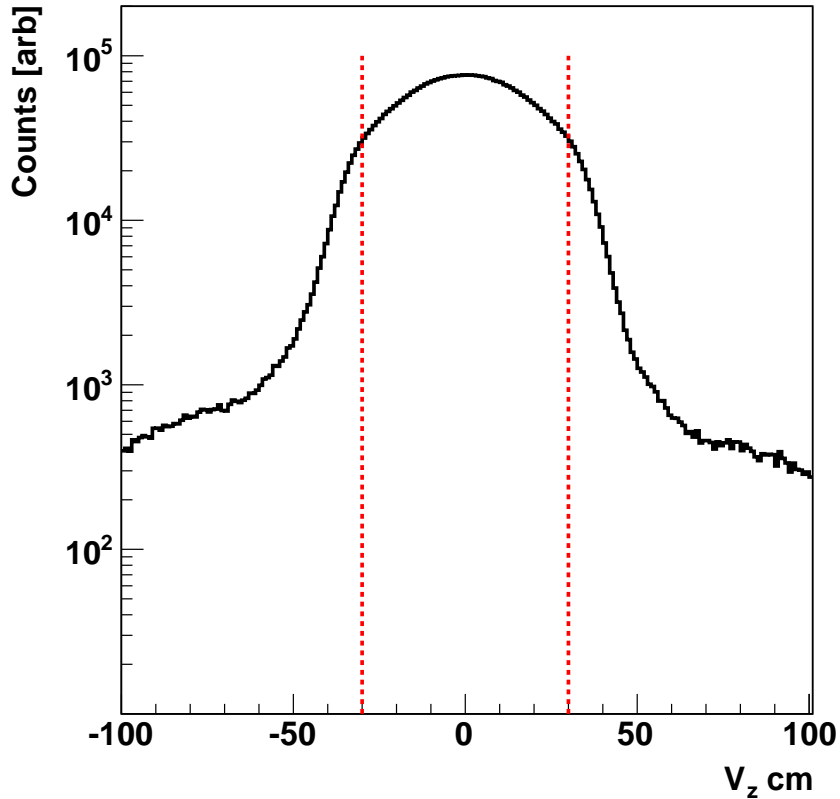


Figure 5.1. The reconstructed V_z distribution for the highest ranked vertex in those events that satisfied the 2007 Υ trigger. The dotted lines indicate the VPD V_z window for this data set.

5.1 Analysis of 2007 Data

The trigger requirements for the 2007 analysis were nearly the same as for the 2006 $p + p$ analysis discussed in Chapter 4, with one key difference. There was no TP requirement for this trigger. The L0 HT trigger threshold was increased from 16 to 18 DSM-ADC, and the opening angle requirement was tightened from $\cos(\theta_{12}^{L2}) < 0.5$ to < 0.0 . The difference in efficiency due to these two changes was determined by simulation. The trigger parameters are listed in Table 5.1

The total integrated luminosity seen by the Υ trigger was roughly $300 \mu\text{b}^{-1}$,

Table 5.1. L0 and L2 parameters for the 2007 STAR Υ trigger

Trigger Parameter	Threshold
HT	> 18 DSM-ADC
L2 Cluster-1	4.0 GeV
L2 Seed Tower Theshold	80 ADC
L2 Cluster-2	2.5 GeV
$\cos(\theta_{12}^{L2})$	< 0.0
M_{12}^{L2}	> 6.0 GeV/ c^2
M_{12}^{L2}	< 25.0 GeV/ c^2

which is equivalent to 9.40×10^8 minimum-bias triggers. The Υ trigger had a different minimum-bias (minbias) trigger for this run than the rest of the STAR triggers, because the online cut on the vertex location as given by the VPD was increased. This was done in order to allow the STAR Υ trigger to sample a greater luminosity. The STAR baseline minbias trigger used the VPD to constrain the vertex location to $|V_z| < 5$ cm, whereas the VPD requirement for the Υ trigger was $|V_z| < 30$ cm. The offline reconstructed vertex distribution for the Υ trigger can be seen in Figure 5.1. Since the TPC acceptance has a dependence on the z position of the vertex, a Glauber model calculation for the Υ triggered data in order to determine the centrality selection had to be performed, as the centrality selection in STAR is based on the TPC charged multiplicity measured in $|\eta| < 0.5$.

5.1.1 Glauber Model

A Monte-Carlo (MC) Glauber model calculation was done to determine the centrality selection for this data set. On an event-by-event basis, for a given impact parameter b , two gold ions were populated with nucleons using a Woods-Saxon dis-

tribution, which describes the nuclear density ($\rho(r)$), shown in Equation 5.1.

$$\rho(r) = \frac{\rho_0}{1 + \exp\left(\frac{r-r_0}{c}\right)} \quad (5.1)$$

The value of ρ_0 was 0.169346 nucleons/fm³, r_0 was 6.5 fm and c was 0.562 fm. The separation between the nucleons was required to be at least 0.9 fm. If two nucleons from the distinct nuclei overlapped, with the assumption that each nucleon had a spherical radius of 0.535 fm, a collision was said to have occurred. We repeat this procedure for $0 < b < 14$ fm until we have a distribution of b versus the number of binary collisions (N_{bin}) and versus the number of participants (N_{part}). Unfortunately none of these quantities are measurable, so additional model assumptions are required to create a distribution in centrality based on a measurable quantity. A two component model can be used to describe the multiplicity distribution:

$$\frac{dN}{d\eta} = n_{pp} \left[(1-x) \frac{N_{\text{part}}}{2} + x N_{\text{bin}} \right] \quad (5.2)$$

Where x is the fraction of the hard component and n_{pp} is the average multiplicity of a $p + p$ collision at $\sqrt{s} = 200$ GeV. In order to generate a multiplicity distribution complete with statistical fluctuations, we convolute the above distribution with a negative binomial for n_{pp} , with one free parameter k . The probability to to create n

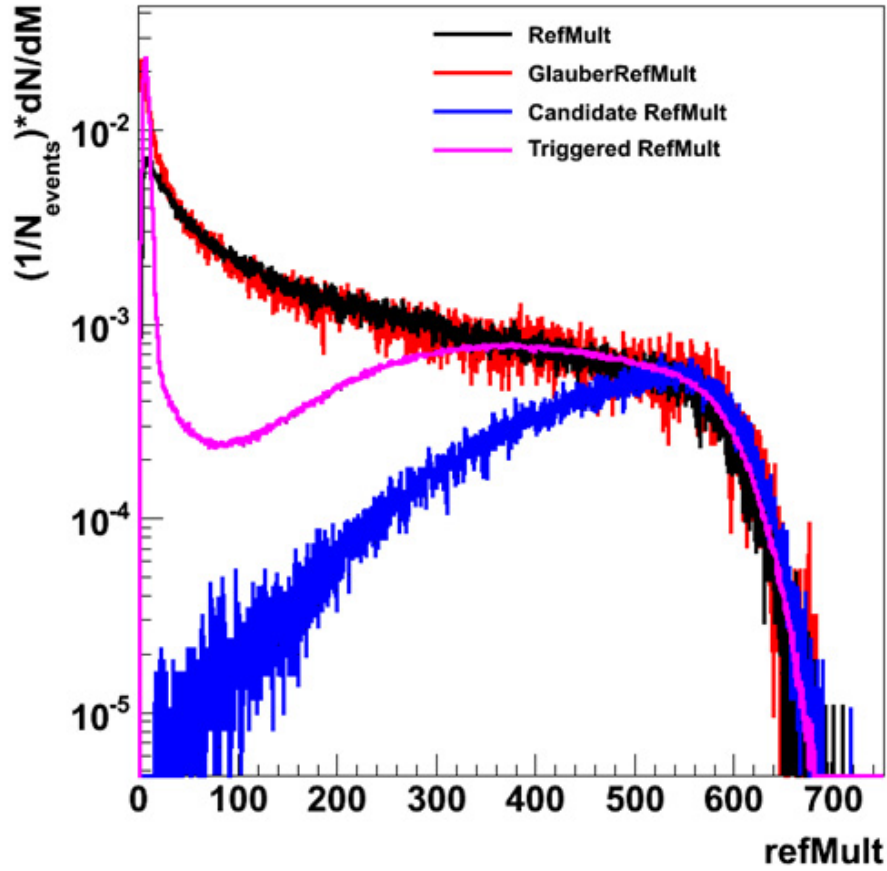


Figure 5.2. Reference multiplicity for 4 categories of events. In black is the reference multiplicity associated with the highest ranked vertex from the Υ minimum-bias trigger. In red is the multiplicity generated from the Glauber model calculation explained in Section 5.1.1. This distribution had a parameter, k , chosen so that it matched the minimum-bias distribution from RefMult > 100 . Below that, the inefficiency of triggering on these low multiplicity events can be seen. The purple curve is the reference multiplicity from the highest ranked vertex from Υ triggered events. It is biased towards central events, with the low reference multiplicity tail coming from those events where the vertexer ranked an out-of-time pile-up vertex ahead of the proper vertex. In blue is the reference multiplicity for those events that had a track associated with each L2 energy cluster.

charged particles in a $p + p$ collision at a given energy is given in Equation 5.3.

$$P(n, n_{pp}, k) = \binom{n+k+1}{k-1} \left(\frac{n_{pp}/k}{1+n_{pp}/k} \right)^n \left(\frac{1}{1+n_{pp}/k} \right)^k \quad (5.3)$$

This probability is sampled N_{part} times for a given b and this allows us to have a measure of the number of charged particles. The value of k is fit by matching the generated distribution with the minbias reference multiplicity (refMult) distribution in the ~ 0 -50% central region, where the refMult is the charged particle multiplicity in the TPC with a $|\eta|$ of 0.5. The generated reference multiplicities can be seen in Figure 5.2 for $k = 2.0$. In this figure, the blue curve, which is the refMult from events with an Υ candidate, is heavily biased towards more central events. This is to be expected for those events in which we are selecting a hard process, as this process should scale proportionally with number of collisions, whereas soft processes scale with the number of participants. The number of collisions increases rapidly with decreasing impact parameter as it scales with the length of the interaction volume along the beam axis [80]. Quantitatively, this works out such that we would expect a hard process that scaled perfectly with N_{bin} to have 40% of its cross section in the top 10% most central events [81].

To select 0-60% the data requires a cut of $\text{refMult} > 47$ and to select 0-10%, this cut should be 430. Also, from this calculation $N_{\text{bin}}(0 - 60\%) = 395 \pm 7$ and $N_{\text{bin}}(0 - 10\%) = 964 \pm 27$. When these cuts were applied to the Υ minimum bias trigger sample, we found that 1.14×10^9 events had $\text{refMult} > 47$ and 1.78×10^8 had $\text{refMult} > 430$. Some of the assumptions that go into the Glauber Model that are important are that it treats each collision as an independent $p + p$ collision with $\sqrt{s} = 200$ GeV. It is assumed that nucleons collide in a completely elastic manner and remain complete nucleons despite suffering several collisions. For the purposes of measuring processes such as the production of Υ at $\sqrt{s_{NN}} = 200$ GeV, these

assumptions are reasonable. The Q^2 for most processes is much less than the p of the nucleons participating in the collision, which is why assuming the collisions are elastic with respect to the nucleons is reasonable, despite the fact that they do lose enough energy to produce particles. Also, valence quark interactions are not the production channel for Υ s, and in fact, valence quark collisions are rare so most collisions are of the gluons in this case. Which means that assuming a nucleon is complete is reasonable. Experimentally, the idea of N_{bin} scaling, along with the calculation of R_{AA} as described in Section 5.1.4, is validated by the PHENIX photon measurement shown in Figure 1.11 and, more recently, by the CMS Z^0 measurement in Pb+Pb collisions [82], discussed in the thesis of J. Robles [83].

5.1.2 PID

As in Chapter 4, this analysis relied on two different methods for determining particle identification. One was to measure the ionization energy loss (dE/dx), and the other was to measure E/p . Both of these methods required a data-driven determination of their efficiencies, as neither is well simulated within the STAR software framework. The distribution of dE/dx is normalized with a parameter labeled as $n\sigma_{\text{electron}}$, which should have a width of 1 and a mean of 0 for electrons. In 2007 the calibration was not quite correct, so the values of the mean and width of the $n\sigma_{\text{electron}}$ Gaussian were determined from the data. For each momentum bin, a three Gaussian fit to the $n\sigma_{\text{electron}}$ distribution was performed to determine the μ and σ of the electron gaussian. An example from $6.0 < p < 7.0$ GeV/ c can be seen in Figure

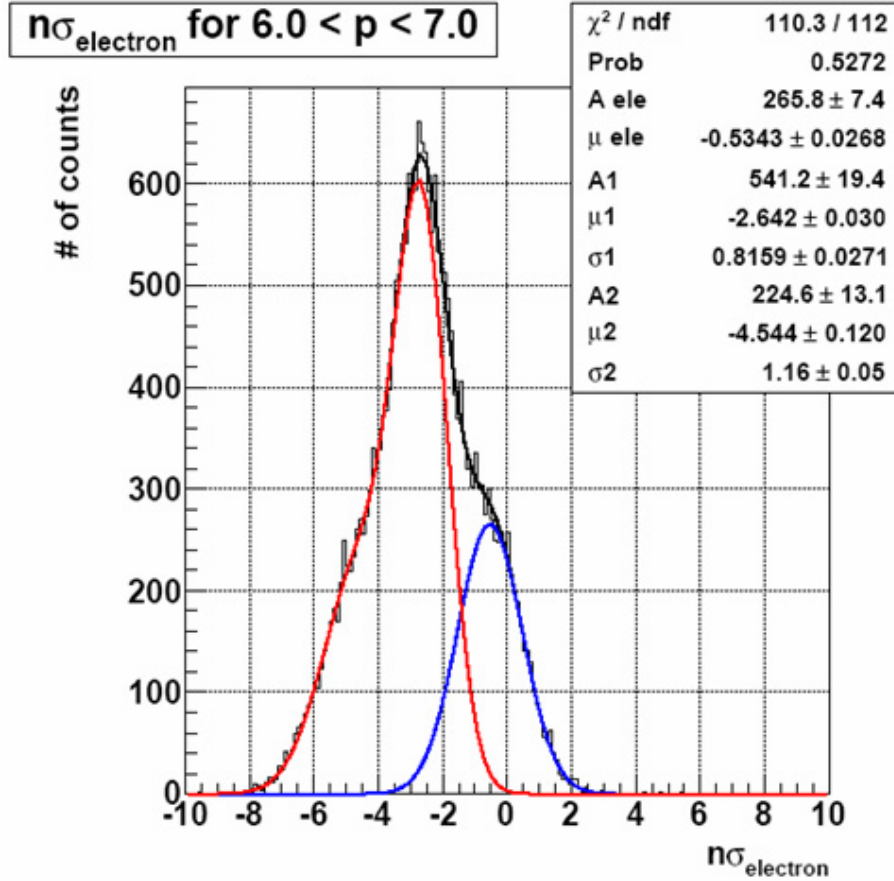


Figure 5.3. The distribution, $n\sigma_{electron}$, a normalized distribution of electron dE/dx for tracks with $6.0 < p < 7.0$ which extrapolate to a trigger cluster. This distribution is simultaneously fit with three gaussians to determine the mean of the electron distribution.

5.3. A straight line was fit to the distribution μ versus momentum in Figure 5.4, and the result was found to be $\langle \mu_{n\sigma_{electron}} \rangle = -0.5326 \pm 0.0087$. The efficiency of any given $n\sigma_{electron}$ cut is calculated assuming a Gaussian with extracted μ and σ . The uncertainty in the fits is a systematic uncertainty.

The distribution of E/p was also examined, as seen in Figure 5.5. This distribution had the same width as the baseline $p + p$ measurement but was found to be shifted to 1.1 due to the increase in the energy deposited in the BEMC due to the higher multiplicity underlying Au+Au events. There are two non-Gaussian features in the

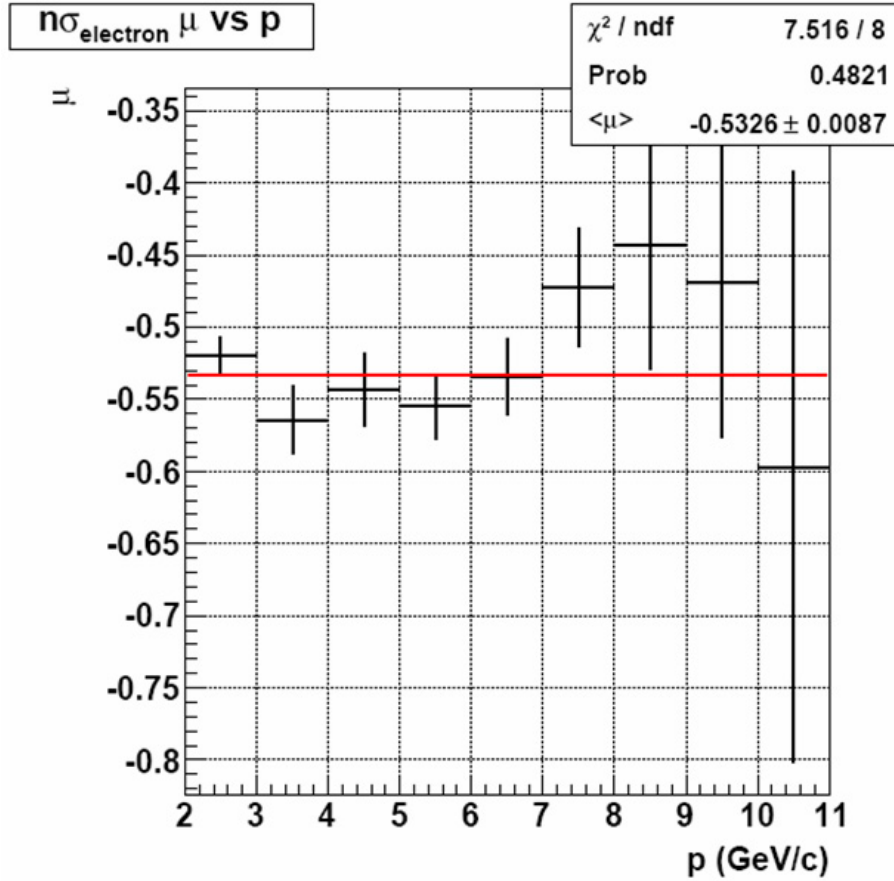


Figure 5.4. The means (labeled as μ) of $n\sigma_{electron}$ versus momentum for tracks which extrapolate to trigger clusters.

Figure 5.5. The excess at low E/p is due hadron contamination. The tail at high E/p is due to bremsstrahlung and π^0 photon conversion electrons as explained in Section 6.1.1. Given their similarities, the efficiency calculations from Chapter 4 were used to determine the efficiency of the E/p cut. To select electrons we used a cut of $-1.4 < n\sigma_{electron} < 3.0$ and $0.8 < E/p < 1.4$. The efficiency of the $n\sigma_{electron}$ cut is 0.807 and the efficiency of the E/p cut is 0.888. The systematic uncertainty of these numbers is discussed in Section 6.1.2. This gives a total efficiency for our PID cuts of 0.514.

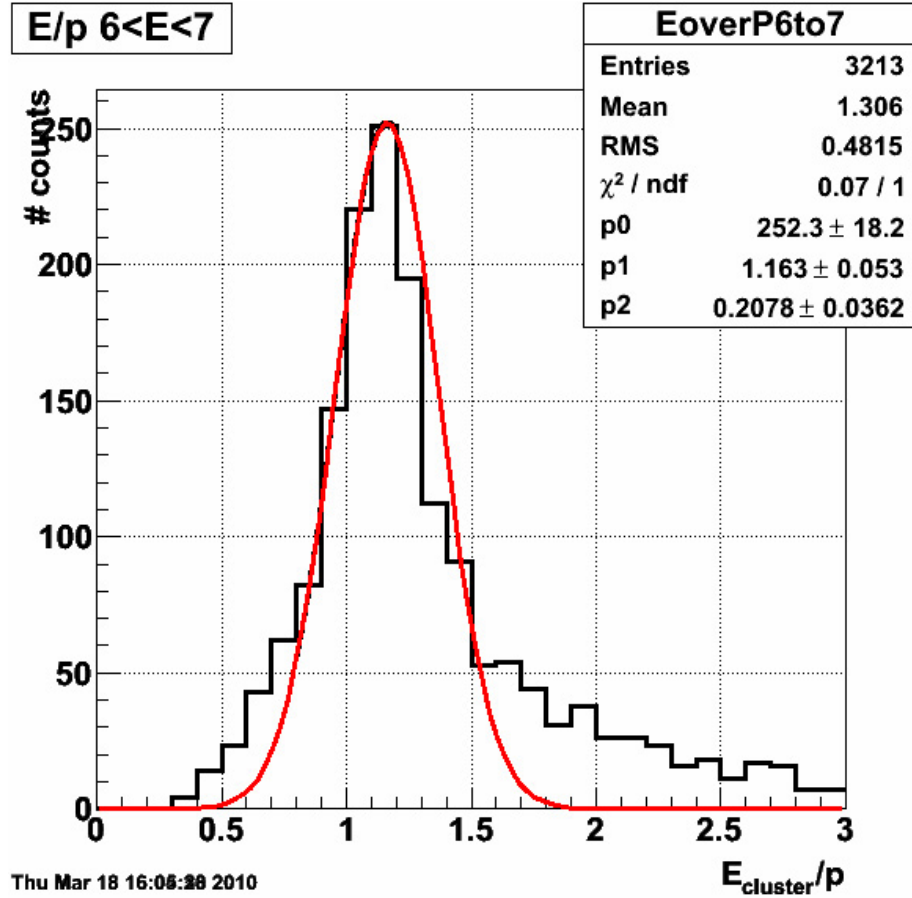


Figure 5.5. The three-cluster energy over the momentum for TPC tracks which extrapolate to a trigger cluster. This distribution is calculated from those tracks with $6 < p < 7$ and has the same width as the distribution calculated in the baseline p+p measurement.

5.1.3 Υ Reconstruction Efficiency

In order to determine the Υ reconstruction efficiency in the Au+Au environment, simulated $\Upsilon \rightarrow e^+e^-$ were embedded directly into Υ triggered events. This allowed us to determine the efficiency versus centrality, one of the main differences between this analysis and the $p + p$ analysis discussed in Chapter 4. Embedding into the minbias data set would have required reweighting the Υ results based on the proper centrality distribution as the Υ trigger is highly biased towards more central events as shown in Figure 5.2. This would have required much greater simulated statistics to achieve

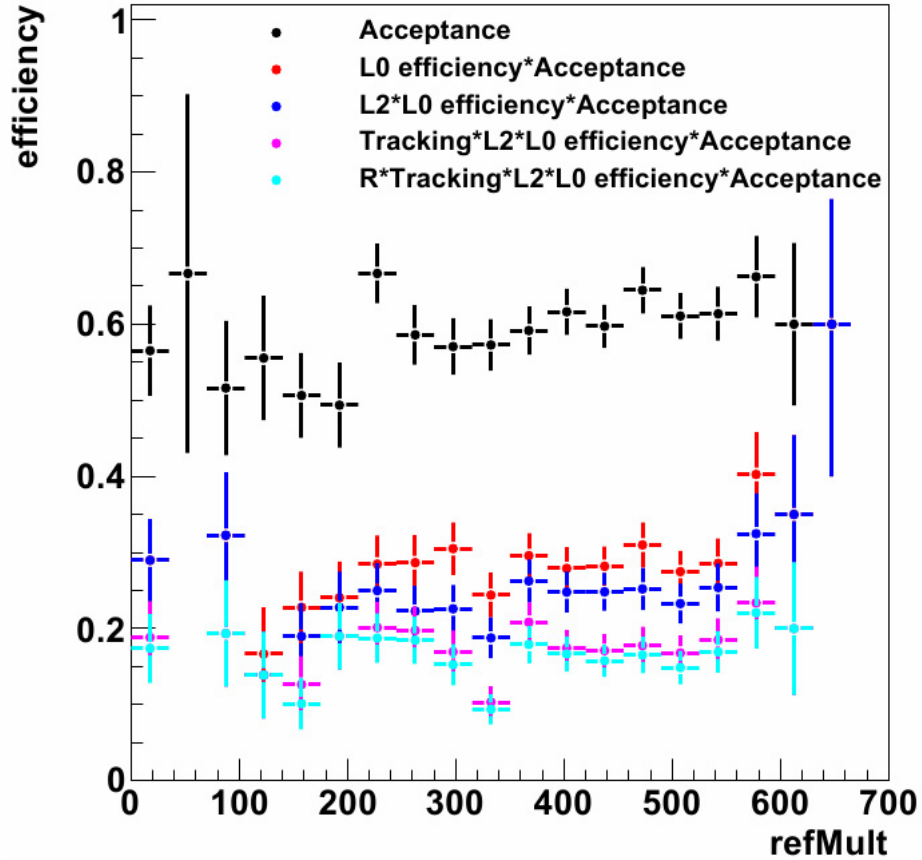


Figure 5.6. Efficiency versus refMult from the 2007 Υ embedding with the 2007 Υ trigger conditions applied. The efficiency appears to be flat versus centrality as the decreased tracking efficiency in the most central events is balanced by the increased trigger efficiency due to the underlying event increasing the probability that a trigger will fire for a given Υ .

the necessary precision.

The line shape is also important when calculating the efficiency of the $\Upsilon(1S + 2S + 3S)$ reconstruction since the three states do not have the same efficiencies. The greater mass of the $\Upsilon(2S)$ and $\Upsilon(3S)$ make them more efficient because their daughter electrons have higher average momenta, facilitating our ability to trigger on them. For this analysis, we calculate the $\Upsilon(1S + 2S + 3S)$ efficiency assuming the PDG values for the branching ratio to electrons and use a NLO CEM calculation to determine

Table 5.2. Efficiency from 2007 Υ embedding with 2007 Υ trigger conditions applied.

Υ state	Acceptance	\times L0	\times L2	\times Tracking
1S	0.57	0.26	0.18	0.12
2S	0.57	0.30	0.22	0.15
3S	0.56	0.33	0.23	0.15
1S+2S+3S	0.56	0.27	0.20	0.13

the cross sections [4]. If the $\Upsilon(2S + 3S)$ were completely suppressed, the assumption that they exist in the same yields relative to the $\Upsilon(1S)$ state as in $p + p$ would bias us towards a higher value for Υ reconstruction efficiency than reality due to the higher efficiency of the excited states. The difference between the efficiency of the $\Upsilon(1S)$ state only and the $\Upsilon(1S + 2S + 3S)$ states weighted in the above manner can be taken a systematic uncertainty. The results can be found in Table 5.2.

5.1.4 R_{AA}

The formula for calculating R_{AA} is given in Equation 5.4.

$$R_{AA} = \frac{\frac{1}{N_{mbAA}} \frac{dN_{AA}^{\Upsilon}}{dy}}{\frac{N_{bin}}{\sigma_{pp}} \frac{d\sigma_{pp}^{\Upsilon}}{dy}} \quad (5.4)$$

Where N_{mbAA} is the number of minbias events from the luminosity sampled, $\frac{dN_{AA}^{\Upsilon}}{dy}$ is the number of Υ from the luminosity sampled, N_{bin} is the average number of binary collisions in the centrality bin under investigation, σ_{pp} is the total inelastic p+p cross section which is taken to be 42 mb at $\sqrt{s_{NN}} = 200$ GeV. Finally, $\frac{d\sigma_{pp}^{\Upsilon}}{dy}$ is the $\Upsilon(1S + 2S + 3S)$ cross section measured in $p + p$ collisions at $\sqrt{s} = 200$ GeV.

5.2 Analysis of 2010 Data

The data is from 50.5 Million events that satisfied the high tower trigger taken during the 2010 RHIC run, roughly $1400 \mu b^{-1}$, roughly $5\times$ the integrated luminosity available in 2007. This is equivalent to 6.85×10^9 minimum bias triggers. An additional 5M triggers were discarded due to run-by-run QA requirements, and a further 5M triggers were not analyzed and could be included in future analyses. The high tower trigger requires a single tower above 18 ADC-DSM (4.2 GeV) in the BEMC. The trigger differed from previous Υ triggers because the recent upgrade to the DAQ allowed us to record TPC data at a higher rate. This allowed us to move the kinematic peak, as seen in Figure 6.7, lower in invariant mass so that the effect of the trigger turn-on was not in our region of interest. The results of the like-sign and unlike-sign spectra agree very well, with the only differences coming from physics processes. In this plot, we can see the excess due to photons with a reconstructed mass near 0. Additional cuts will increase the S/B ratio in the Υ mass region. The percentage of events that had multiple towers that satisfied the L0 requirement, as shown in Figure 5.7, is similar to that of 2007. These events are noteworthy only in that they are events where it is possible to double count Υ candidates if proper care with Υ reconstruction is not taken.

The offline analysis for this measurement was similar to that described in 5.1, with some key differences. As before, we started with the towers that satisfied the L0 requirement and formed a three tower cluster. The distribution of that 3 tower energy cluster can be shown in Figure 5.8. The dotted line indicates the energy equivalent

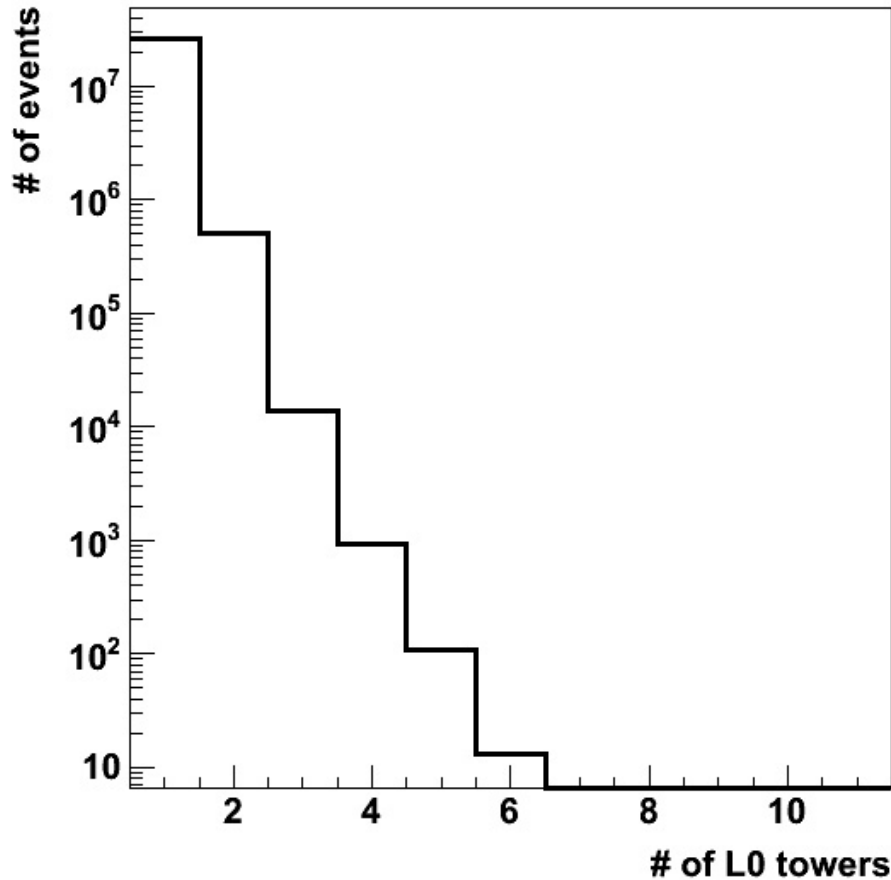


Figure 5.7. The number of towers satisfying the L0 trigger requirement for the 2010 data set.

for the L0 trigger requirement of 18 DSM-ADC. The peak is shifted higher than what is expected from the single tower trigger threshold, due to the extra energy in the cluster given by the additional two towers. The calibration used to determine the energy was the offline calibration as of January 15, 2011. The second daughter was required to have a valid single tower energy, but no further constraints were required. The single tower for the second daughter was the tower closest in $\eta - \phi$ to where the daughter projects to on the BEMC. The energy distribution for those daughters can be seen in Figure 5.9. In this figure a loose selection on the normalized ionization energy loss of $-2 < n\sigma_{electron} < 3$ was performed in order to remove some of the pion

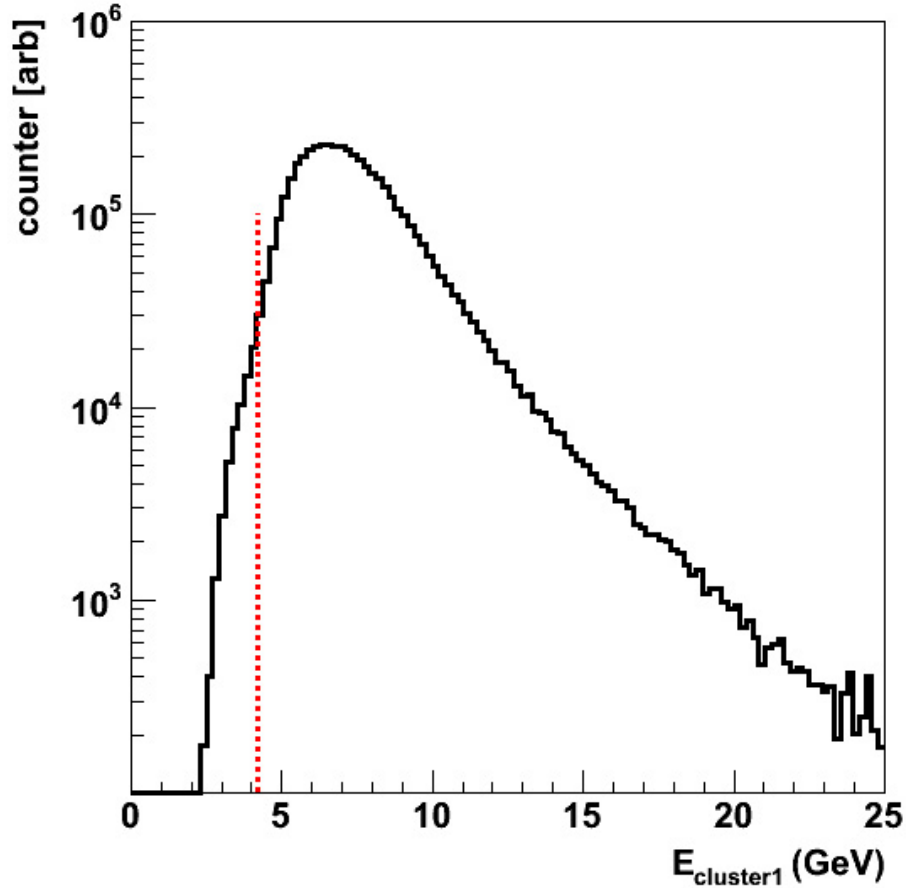


Figure 5.8. The 3 tower energy cluster formed for those towers that met the L0 trigger requirement. The red dotted line indicates the online energy value for the adc of 18.

background. Shown in Figure 5.10 is the invariant mass distribution for like-sign and unlike-sign pairs with a cut on E/p of < 3 and $-2 < n\sigma_{electron} < 3$. We can see the kinematic peak is close to $4.5 \text{ GeV}/c^2$, far from the Υ mass region.

5.2.1 PID

As before, we used two different methods to select electrons for our analysis: E/p and $n\sigma_{electron}$. The E/p distribution for both daughters in the range of $5 < E < 6$ GeV, with a cut of $n\sigma_{electron} > 0.5$ to have a high purity sample, is shown in Figure 5.11. For simplicity, we chose the same E/p cuts of $0.7 < E/p < 1.3$ as used in the

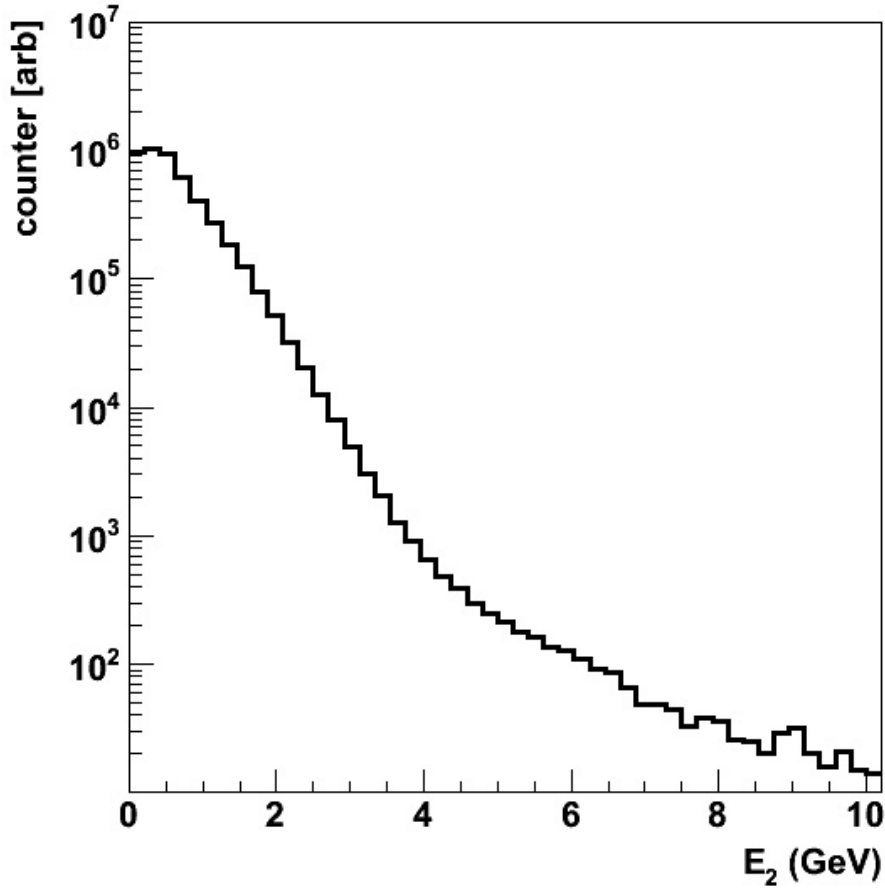


Figure 5.9. The single tower energy for secondary tracks that are in HT trigger events with a requirement that the energy in the tower based on the offline calibration be greater than 0. The tracks had a loose selection on the normalized ionization energy loss of $-2 < n\sigma_{electron} < 3$ in order to remove some of the pion background.

the $p + p$ analysis. Just as in Section 5.1.2 the width of the 3 tower cluster associated with the triggered daughter is close to 0.16, very similar to the result seen in Chapter 4 for the $p + p$ analysis. Also, the peak was centered at $E/p = 1.1$, just as in 5.1.2. The second daughter, using only a single tower, had an E/p distribution peaked at 0.95 with a width of 0.18. The efficiencies for these daughters was determined as in Chapter 4 for the $p+p$ analysis. The E/p distribution from the 2007 embedding was smeared in order to match the measured width, and then the efficiency was determined from this smeared distribution. For these cuts, the efficiency of the cut

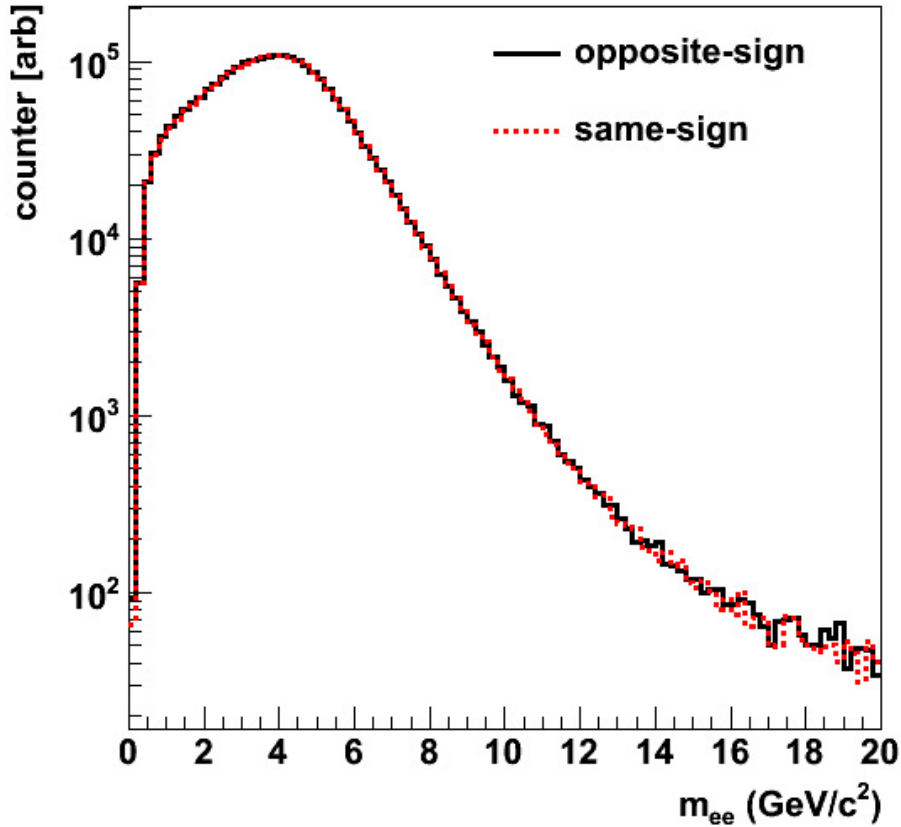


Figure 5.10. In solid is the distribution for opposite sign track pairs and in the red dotted line for same sign pairs with $|1 - E/p| < 3$ and $-2 < n\sigma_{electron} < 3$. The kinematic peak is far removed from our region of interest of $7 < M_{ee} < 12 \text{ GeV}/c^2$.

on the triggered daughter is 0.885 and the efficiency of the cut on the secondary daughter is 0.883.

One thing to note is that by not having an energy requirement on the second daughter, we introduce a large pion background. This can be seen in Figure 5.12 on the right side of the graph. On the left side is the E/p versus E for the triggered daughter, which we can see is close to 1 as expected for electrons. In the right side there are a lot of low energy particles with a low E/p that cannot be electrons. It may be useful in the final analysis to determine whether an additional cut on energy could reduce the pion background. For this analysis, a cut on $p_T > 1 \text{ GeV}/c$ was placed on

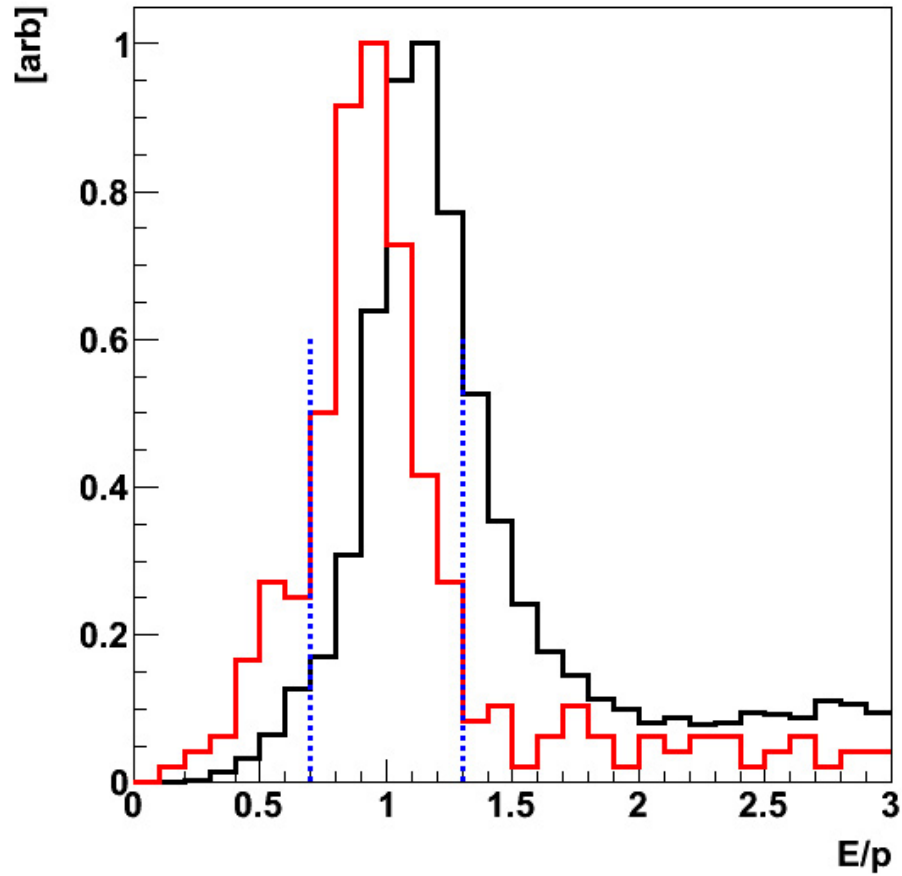


Figure 5.11. E/p distributions for the two Υ candidate daughters. In black is the distribution using the three tower cluster associated with the L0 trigger tower. In red is the single tower value for the secondary daughter. The dotted lines are the offline analysis cuts used to select electrons.

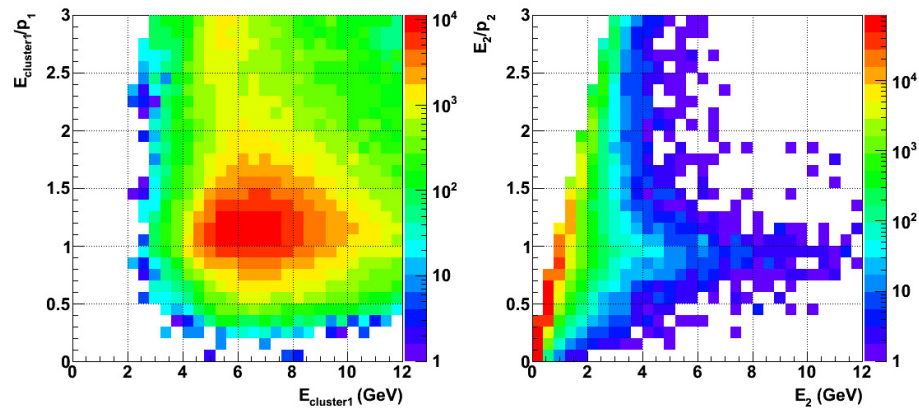


Figure 5.12. E/p versus E for the triggered daughters on the left and the secondary daughters on the right.

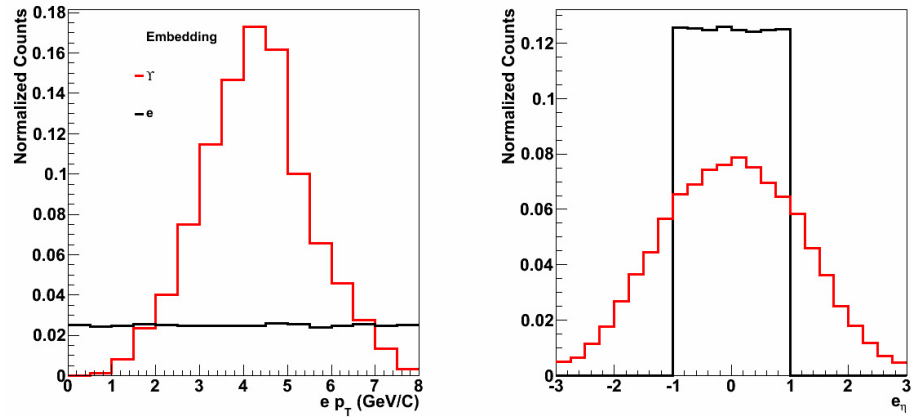


Figure 5.13. The kinematic distributions of the two different electron embedding data sets. In red is the monte carlo distribution from the electrons coming from $\Upsilon(1S)$ as embedded into the 2007 geometry. In black is the distribution from the monte carlo distribution of the electrons embedded into the 2010 geometry.

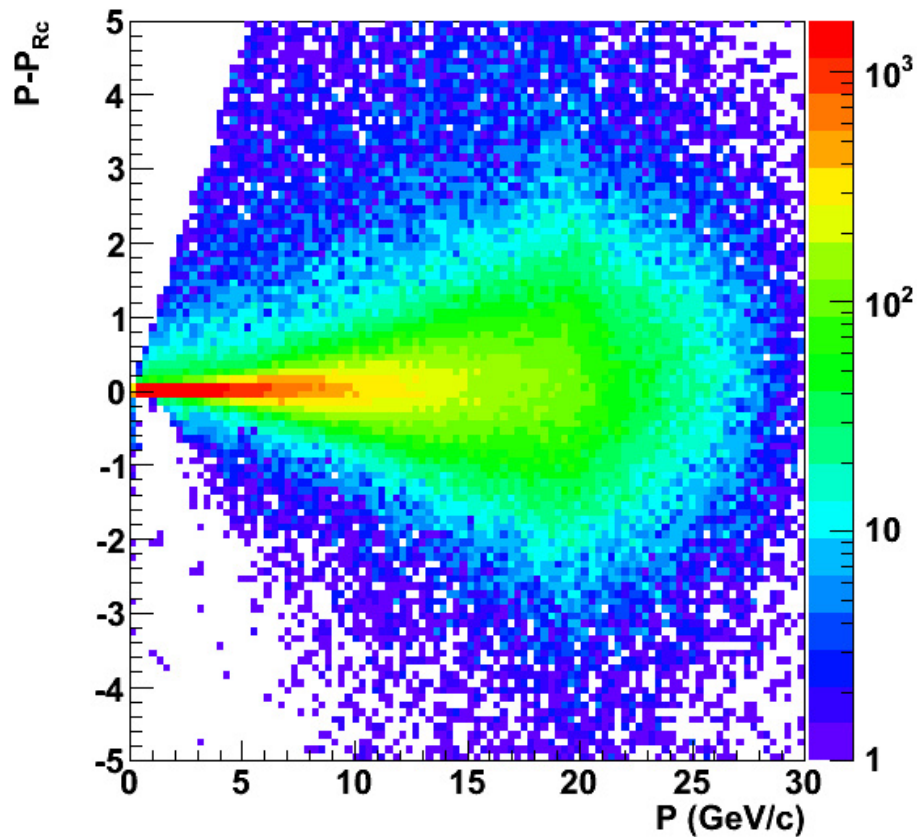


Figure 5.14. The difference between the MC and reconstructed momentum versus the MC momentum for electrons which were accepted, reconstructed and passed the track quality cuts.

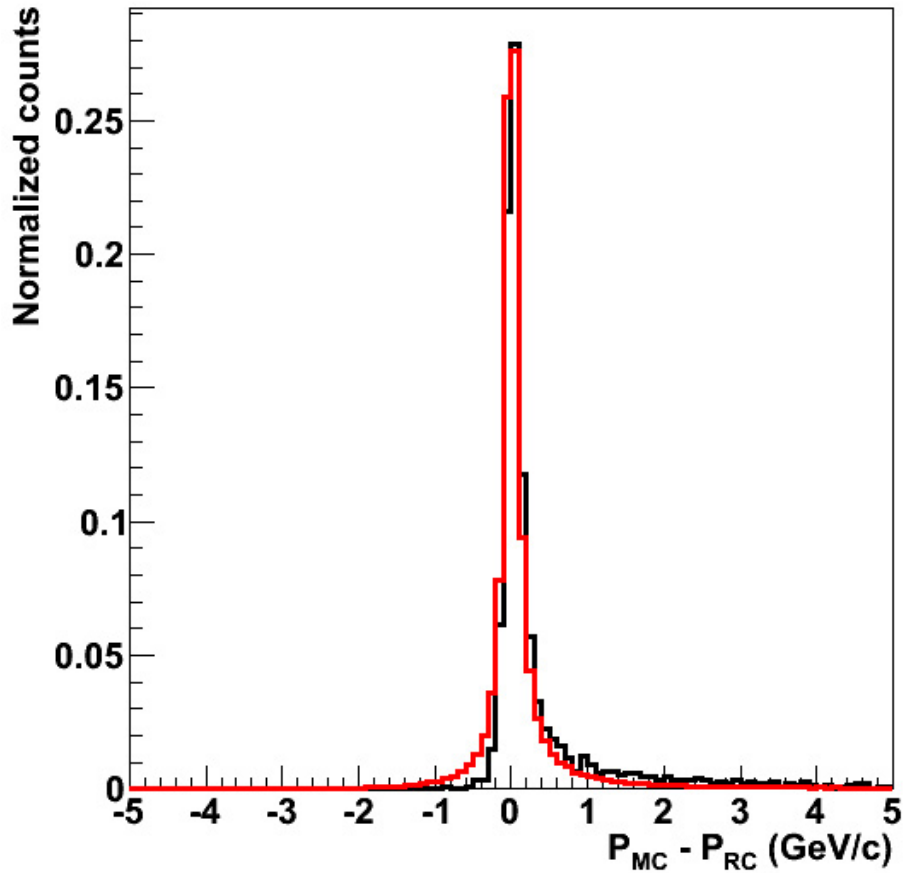


Figure 5.15. The difference between the MC and reconstructed momentum for electrons which were accepted, reconstructed and met the track quality cuts. In black is the distribution coming from $\Upsilon(1S) \rightarrow e^+e^-$ embedded into the 2007 geometry. In red is the pure electron sample, weighted by the expected momentum distribution from Υ decays, embedded into the 2010 geometry.

the non-triggered daughter in order to remove most of the pion background.

The single track distribution for the $n\sigma_{electron}$ distribution was extensively studied during the Non-Photonic Electron (NPE) analysis of the 2010 data, and it was found that the calibration was performed such that the distribution was centered about 0 with a width of 1 [84]. The $n\sigma_{electron}$ distribution was selected as $-1 < n\sigma_{electron} < 3$, which is the same range as chosen in Chapter 4 for the $p + p$ analysis with the caveat that the shift in the center of this distribution was reflected in the cut. The single

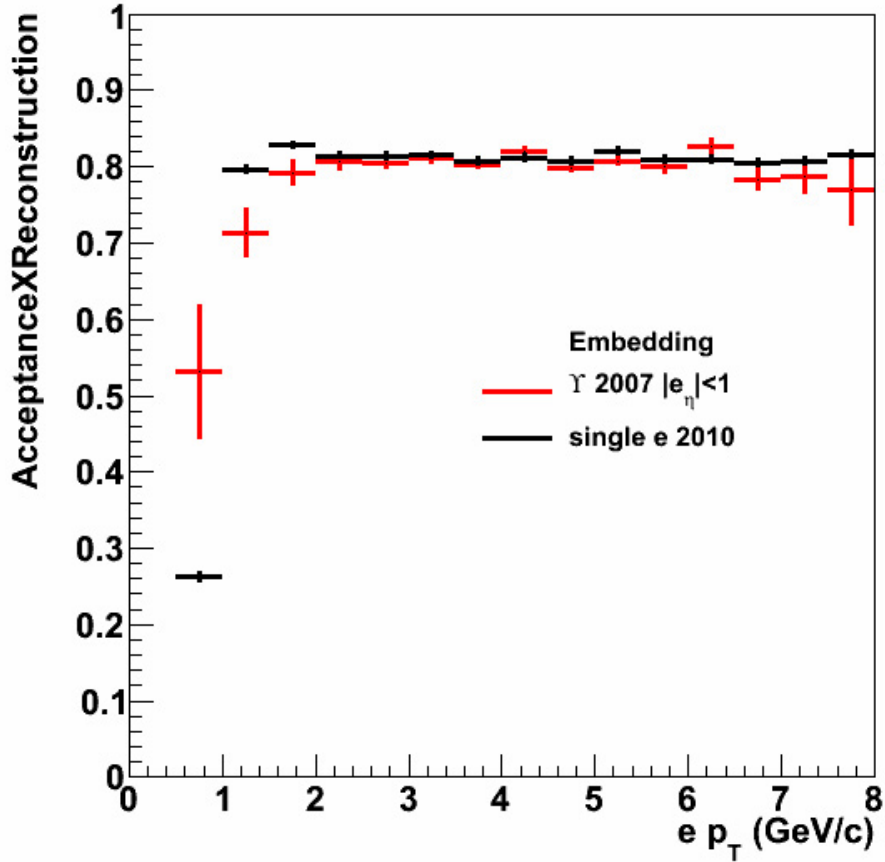


Figure 5.16. Reconstructed track efficiency for 2007 versus 2010 embedding samples. Black is the sample from the single electron sample from 2010, with the proper kinematic weighting for the Υ kinematics folded in and red is the $\Upsilon(1S)$ 2007 sample.

track efficiency of this cut is 0.84. Combing all these results together, we have a total PID efficiency of 0.552.

5.2.2 Υ Reconstruction Efficiency

For this analysis an embedding sample of $\Upsilon \rightarrow e^+e^-$ was not available. The efficiency and line shape were determined by using two different simulation samples. One was the embedding data set described in Section 5.1.3. The problem with this embedding data set is that the SVT had been removed prior to the 2010 analysis. The

2007 embedding sample was used to determine the trigger efficiency by applying the HT trigger requirements to the embedded Υ 's. We have now developed a technique to use the single electron efficiency to calculate the pair-wise trigger efficiency. The trigger efficiency will be updated using this technique with the simulation that more accurately represents the number of radiation lengths trigger electrons had to travel prior to reaching the BEMC.

The change in the inner-material will change the distribution of the difference between the reconstructed and Monte Carlo momentum ($p_{RC} - p_{MC}$). This, in turn, will change the line shape. The change in the inner-material can also have an effect on the track reconstruction efficiency for lower momentum tracks. While an Υ -specific embedding was not available, there was a sample of electrons embedded into the 2010 geometry that could be used. This embedding sample had electron tracks thrown in a distribution that is flat in p_T from 0 to 30 GeV/ c and flat in y from -1 to 1. They were embedded directly into high tower events. One issue with using this data set is that these quantities, p resolution and track-reconstruction efficiency, are dependent on the kinematic distributions of the particles in question. Kinematically, the electrons from this data sample had a very different distribution as the electron daughters coming from an $\Upsilon \rightarrow e^+e^-$ decay as seen in Figure 5.13. This becomes important when determining the exact resolution difference, as we can see from Figure 5.14. After weighting the distribution of the Monte Carlo momentum minus the reconstructed moment for those electrons that were accepted, reconstructed and passed the track quality cuts, the difference between the electrons from the 2007 embedding and the 2010 can be seen in Figure 5.15.

Table 5.3. Efficiency from 2010.

Centrality	Acceptance	x L0	x Tracking	x Rcut	x Mass Integral	x PID
0-60%	0.56	0.30	0.15		0.15	0.079
0-10%	0.56	0.34	0.15		0.14	0.075
10-30%	0.56	0.26	0.15		0.14	0.079
30-60%	0.56	0.24	0.15		0.14	0.078

The change in line shape due to the resolution difference seen in 5.15 was less than a five percent effect on the yield given the bin size in invariant mass and the systematic uncertainty due to underlying physics contribution to the line shape. In order to decrease the systematic differences between this analysis and the $p + p$ analysis described in Chapter 4, the same Crystal-Ball parameters were used. After accounting for the kinematic differences between the distributions, the track reconstruction efficiency was identical for those tracks with $p_T > 2$ GeV/ c , as shown in Figure 5.16, and the efficiency differed by 6% for the region of $1 < p_T < 2$. However only 0.7% of the tracks used to reconstruct an invariant mass in the region between 8 and 12 GeV/ c^2 came from this kinematic region, so this introduces only a small ($\sim < 0.1\%$) systematic variation on the estimated yield.

5.2.3 Centrality Selection

As in section 5.1.1, a Glauber model calculation was performed to determine the centrality definition. However, unlike in the previous analysis, the VPD V_z timing window was the same for the HT trigger used in the Υ analysis as for the standard STAR minimum-bias trigger so we used the same centrality definitions as the other 2010 analyses. In order to remove pile-up from the centrality analysis, only those reconstructed vertices with a V_z within 4 cm of the VPD V_z were used. These cuts

Table 5.4. Centrality cuts and uncertainties

Centrality bin	Cut	N_{bin}	unc N_{bin}	N_{part}	unc N_{part}	N_{mbAA}
0-60%	> 41	393	27	161	9	4.49×10^9
0-10%	> 375	962	28	325	4	7.09×10^8
10-30%	$> 182, < 376$	493	32	202	10	1.57×10^9
30-60%	$> 41, < 183$	138	24	80	10	2.21×10^9

were then used on the minbias trigger data set to determine N_{mbAA} .

Events were selected which satisfied the HT trigger requirement. Reconstructed vertices from the events were only used if they were within 4 cm of the VPD vertex. Due to the vertexing software, there could only be at most 2 vertices within 4 cm of the VPD, however this rarely happened. There were no events with multiple vertices that were within 4 cm of the VPD where each vertex had a track that extrapolated to a tower that could have fired the trigger. Thus we were safe to use the best vertex based on these criteria from the list of reconstructed vertices.

The triggered daughter track for the Υ candidates, given the label “daughter 1”, was selected from those tracks that were within $R < 0.04$ of the cluster around the trigger tower, with $0.7 < E/p < 1.3$ and with $-1 < n\sigma_{electron} < 3$. The second daughter (“daughter 2”) for the Υ candidate was chosen from the collection of other tracks associated with the same vertex as daughter 1. Daughter 2 was required to extrapolate to a tower with a non-zero value of energy (defined as having greater than $3 \times$ the pedestal energy width), and to also have $0.7 < E/p < 1.3$ and $-1 < n\sigma_{electron} < 3$. Both daughters had to have the same track quality cuts as listed in Chapter 4. These candidate pairs were then combined to like-sign and unlike-sign pairs. Once these distributions were determined, we can extract the Υ yield and determine R_{AA} , discussed in the next Chapter.

Chapter 6

Results

The results of the $\Upsilon(1S + 2S + 3S)$ in $p + p$ and in Au+Au are listed below. The $p + p$ analysis is used as the baseline for both of the Au+Au analyses.

6.1 Results for Υ in $p + p$

Electron-positron pairs are formed from TPC tracks that match to energy clusters that satisfy the L0 and L2 trigger requirements. These track pairs are used to produce the like-sign and unlike-sign invariant mass spectrum, using the track momentum reconstructed in the TPC and assuming the electron mass. The like-sign combinations of e^+e^+ and e^-e^- are used to estimate the combinatorial background as specified in Equation 6.1 [85].

$$N_{+-}^{\text{bck}} = 2\sqrt{N_{++}N_{--}} \cdot \frac{A_{+-}}{\sqrt{A_{++}A_{--}}} \quad (6.1)$$

The label N_{+-} (N_{++} , N_{--}) denotes the unlike-sign (like-sign) pair differential

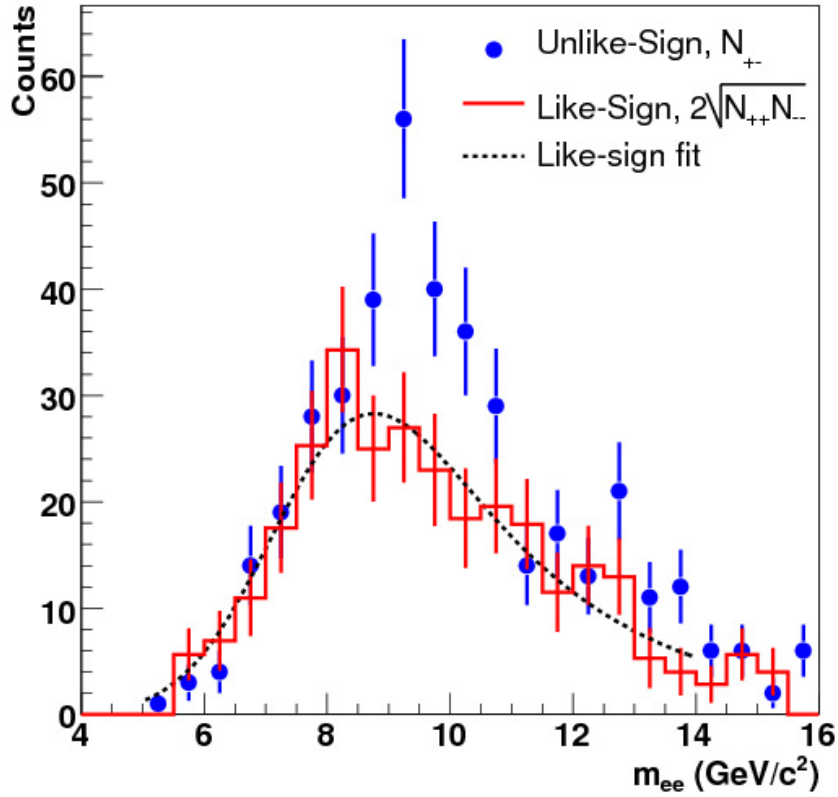


Figure 6.1. The invariant mass spectrum for the like-sign in red and the unlike-sign in blue from the Υ triggered data set in $p+p$. The black dotted line is a fit to the like-sign distribution explained in the text.

invariant mass distribution dN_{+-}/dm (dN_{++}/dm , dN_{--}/dm) and A_{+-} (A_{++} , A_{--}) denotes the acceptance for unlike-sign (like-sign) pairs. For the BEMC and TPC, $A_{+-} = A_{++} = A_{--}$ so Equation 6.1 simplifies to: $2\sqrt{N_{++}N_{--}}$. The unlike-sign and like-sign background invariant mass spectra are shown in Fig. 6.1.

6.1.1 Υ Line-Shape in p - p collisions

As stated in Chapters 5 and 6, we can not resolve individual states of the Υ family due to the limited statistics, finite momentum resolution, and electron bremsstrahlung.

So the yield reported here, and for the Au+Au analyses is for the combined $\Upsilon(1S + 2S + 3S)$ states.

The unlike-sign di-electron yield after the subtracting the combinatorial background given by the like-sign yield has three components: the Υ states, the Drell-Yan (DY) continuum and the $b\bar{b}$ continuum. In order to extract the Υ yield, which is the focus of this thesis, we need to be able to subtract the continuum yield from the unlike-sign contribution. To do this, we parameterize the expected shapes of each contribution. The parameterization for the Υ states is a functional form that was introduced by the Crystal-Ball experiment [86]. This parameterization was fit to the reconstructed invariant mass shapes from the $\Upsilon(1S)$, $\Upsilon(2S)$, and $\Upsilon(3S)$ states from the embedded sample discussed in Sections 4.2.2 and 4.2.3. The Crystal-Ball parameterization is shown in Equation 6.2.

$$f(m) = N \cdot \begin{cases} \exp\left(-\frac{(m-\mu)^2}{2\sigma^2}\right), & \text{for } \frac{m-\mu}{\sigma} > -\alpha \\ A \cdot \left(B - \frac{m-\mu}{\sigma}\right)^{-n}, & \text{for } \frac{m-\mu}{\sigma} \leq -\alpha \end{cases} \quad (6.2)$$

This equation and its derivative are both continuous if constants A and B are:

$$\begin{aligned} A &= \left(\frac{n}{|\alpha|}\right)^n \cdot \exp\left(-\frac{|\alpha|^2}{2}\right) \\ B &= \frac{n}{|\alpha|} - |\alpha| \end{aligned} \quad (6.3)$$

The lineshape for the $\Upsilon(1S + 2S + 3S)$ is a sum of three Crystal-Ball functions with their parameters fixed to the values determined by the fit to the simulated Υ s, and then their relative yields are fixed based on the average branching ratios to electrons and ratios of cross-sections shown in Table 4.2. The total yield of the three

Crystall-Ball functions is left as free parameter.

Drell-Yan and $b\bar{b}$ Continuum Contributions

The Drell-Yan continuum is parameterized from a pQCD NLO calculation [25] done in the kinematic range $|y_T| < 0.5$ and $m > 4 \text{ GeV}/c^2$. We convoluted the calculated spectrum with the detector resolution (accounting for bremsstrahlung), but this introduced only a very small change in the shape of the spectrum. We find that the shape of the Drell-Yan continuum can be parameterized by a function of the form listed in Equation 6.4.

$$\frac{A}{(1 + m/m_0)^n} \tag{6.4}$$

with the parameters $m_0 = 2.70 \text{ GeV}/c^2$ and $n = 4.59$.

The $b\bar{b}$ contribution is parameterized from a simulation using PYTHIA 8 [76]. We turn on production of $b\bar{b}$ pairs, and follow their fragmentation to B hadrons and then look at the subsequent decays of the B hadrons for di-electrons originating from the b quarks. As with the Drell-Yan continuum, we convoluted the simulated shape with the detector resolution and bremsstrahlung, and find that the shape is well described by a function of the form given in Equation 6.5.

$$\frac{Am^b}{(1 + m/m_0)^c} \tag{6.5}$$

The parameters were found to be $b = 1.59$, $m_0 = 29.7 \text{ GeV}/c^2$, and $c = 26.6$.

We did not wish to embed the simulated Drell-Yan and $b\bar{b}$ distributions and de-

to terminate the trigger response due to the extreme computing cost, we needed to find a way to parameterize the effect of the STAR Υ trigger on the continuum. The STAR Υ trigger was designed to reject events with a low invariant mass ($\sim < 6\text{GeV}/c^2$), we can parameterize the response by multiplying the functional forms of the Drell-Yan and $b\bar{b}$ continuum with an error function. This will give us both a trigger turn on and a width to that turn on due to resolution effects. This error function is listed in Equation 6.6.

$$\frac{\text{erf}((m - m_{\text{trig}})/w) + 1}{2} \quad (6.6)$$

Where m_{trig} is related to the trigger thresholds and w describes the width of the turn-on of the error function due to finite detector resolution. We obtained these parameters from the a fit to the like-sign data in Figure 6.1 by multiplying the error function with an exponential $\exp(-m/T)$ to account for the random like-sign combinations at higher mass. We use the like-sign for this fit because it is purely due to combinatorics and thus the shape of the distribution is not influenced by real physics such as the near-by $\Upsilon(1S)$ peak. In this data set, the parameters are $m_{\text{trig}} = 8.1 \pm 0.8 \text{ GeV}/c^2$ and $w = 1.8 \pm 0.5 \text{ GeV}/c^2$. In order to check our assumption that we did not need to fully simulate the Υ trigger response on the continuum, we varied the turn-on function parameters. This gave a negligible variation on the extracted yields, so our assumption was valid.

To obtain the $\Upsilon(1S + 2S + 3S)$ yield, we fit the unlike-sign invariant mass distribution after subtracting the like-sign background with a functional form that includes

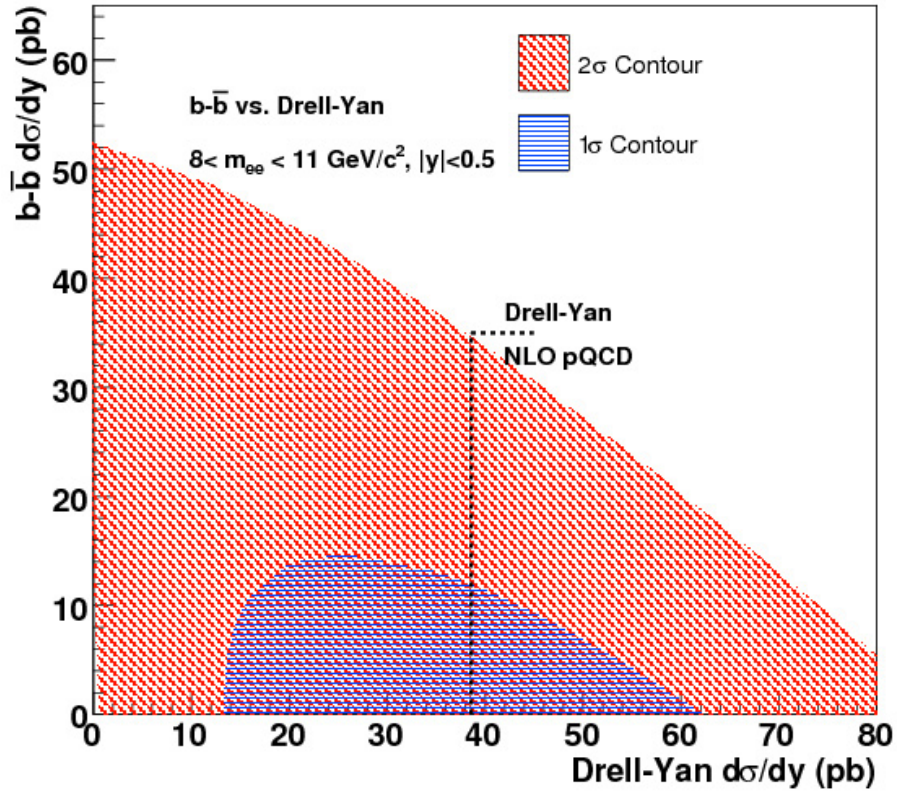


Figure 6.2. The correlation between the Drell-Yan and $b\bar{b}$ continuum cross-sections in the phase space region of $|y| < 0.5$ and $8 < m_{ee} < 11 \text{ GeV}/c^2$ at the 1σ and 2σ level. The prediction from an NLO calculation of the Drell-Yan cross section [25] is shown as the vertical line at 38.6 pb.

all three contributions listed above. The issue is that there is an anti-correlation between the Υ yield and the continuum yield. In the next section, we discuss how variations on the Drell-Yan and $b\bar{b}$ yields can affect the total Υ yield, and thus the measured cross-section.

The two parameterizations of the continuum contributions are very similar and they are also anti-correlated. The 1 and 2σ contours in the 2-D parameter space $\sigma_{b\bar{b}}$ vs. σ_{DY} are shown in Fig. ???. The quoted cross-sections are for the phase space in our region of interest of $|y| < 0.5$ and $8 < m_{ee} < 11 \text{ GeV}/c^2$.

The fit shows a strong anti-correlation between the Drell-Yan and the $b\bar{b}$ cross sections due to the similarity of their functional forms. The shape of the Drell-Yan is slightly favored by our data, and we obtain the minimal χ^2 for a Drell-Yan cross section of ≈ 38 pb with a negligible $b\bar{b}$ contribution. The fit gives $\chi^2/\text{NDF} = 1.1$. The prediction from an NLO calculation of the Drell-Yan cross section [25] is shown as the vertical line at 38.6 pb. This prediction is consistent with values in the $1\text{-}\sigma$ region. Within this region, the $b\bar{b}$ cross-section can be as much as 15 pb, assuming the Drell-Yan is subsequently reduced. For our purposes, we do not need to separate the two contributions, rather all we care about is their sum. This sum is: $(\sigma_{DY} + \sigma_{b\bar{b}})|_{|y|<0.5, 8<m<11\text{GeV}/c^2} = 38 \pm 24$ pb. This variation is taken into account in the fit to extract the Υ yield, and is included in the quoted uncertainty.

6.1.2 Υ yield and cross-section

The fitting function in Fig. 6.3 has three free parameters: the $\Upsilon(1S + 2S + 3S)$ yield, the Drell-Yan yield and the $b\bar{b}$ yield. The rest of the function form is set to the values determined in Section 6.1.1. This fit allows us to extract the Υ yield directly and includes both the statistical uncertainty of the points in Figure 6.3 and the uncertainty due to the anti-correlation between the Υ yield and the continuum yield. Another method that can be used to extract the $\Upsilon(1S + 2S + 3S)$ yield is to do a bin counting method. There are two different ways that this can be done. One is to take the background-subtracted unlike-sign yield directly from the data shown in Fig. 6.3, where the background subtraction is done for each mass bin. We can

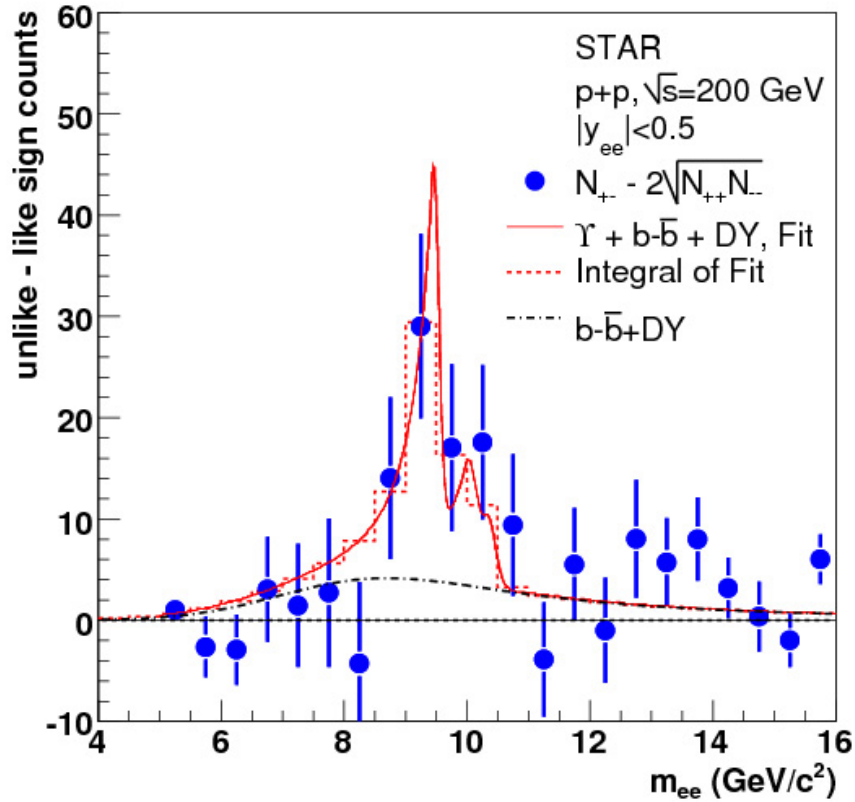


Figure 6.3. The blue data points are the result from subtracting the like-sign yield in Figure 6.1 from the unlike-sign on a bin-by-bin basis. The error bars on these points are statistical only. The solid red curve is the parameterization of the $\Upsilon(1S + 2S + 3S)$ states plus the contribution from the Drell-Yan and $b\bar{b}$ continuum as described in the text. The dashed red histogram is the integral of the fit function in each bin. The black dot-dashed line is the total of the Drell-Yan and $b\bar{b}$ continuum.

then sum the resulting histogram between 8–11 GeV/c^2 and subtract the contribution from the Drell-Yan and $b\bar{b}$ continuum obtained in the fit. A second method is to sum the yield of the unlike-sign (N_{+-}) in the region 8–11 GeV/c^2 , do the same for the like-sign positive (N_{++}), and like-sign negative (N_{--}), and then do the subtraction $N_{+-} - 2\sqrt{N_{++}N_{--}}$. We can call this latter method the single bin method. The results of these three methods for determining the background-subtracted unlike-sign yield and the resulting $\Upsilon(1S + 2S + 3S)$ yield are listed in Table 6.1.

Table 6.1. Extraction of $\Upsilon(1S+2S+3S)$ yield by bin counting and fitting. The sums are done in the range $8 < m < 11$ GeV/ c^2 .

Fitting Results	
$N_{+-} - 2\sqrt{N_{++}N_{--}}$	80.9
Υ counts	59 ± 20
Bin-by-bin Counting	
$N_{+-} - 2\sqrt{N_{++}N_{--}}$	82.7
Υ counts	61 ± 20
Single-bin Counting	
$N_{+-} - 2\sqrt{N_{++}N_{--}}$	75 ± 20
Υ counts	54 ± 18

The quoted uncertainty in $N_{+-} - 2\sqrt{N_{++}N_{--}}$ is listed for the single-bin counting method, which is obtained from a straightforward application of the statistical errors of the corresponding yields ($N_{+-} = 230$, $N_{++} = 92$, $N_{--} = 65$). It contributes 26% to the uncertainty, and originates only from counting statistics. In addition to this statistical uncertainty, we must also take into account the uncertainty of the continuum subtraction. We can not simply use counting statistics to determine the uncertainty on the $\Upsilon(1S + 2S + 3S)$ yield due to the continuum subtraction because the Υ yield and the continuum yield are anti-correlated. This anti-correlation must be taken into account when determining the total uncertainty in the Υ yield. The best way to determine this is by the fitting method because the fit takes into account both the statistical precision of the invariant mass spectrum and the anti-correlation between the Υ yield and the continuum yield. We find the uncertainty from the fit to be 33% of the Υ yield, and we use this fitting-method result to estimate the uncertainty in all the Υ yields quoted in Table 6.1. We quote this as the “stat. + fit” uncertainty in our cross section result. In this analysis, the allowed range of the of the variation of the continuum yield is still dominated by the statistical uncertainty,

so most of this 33% is statistical in nature.

A systematic uncertainty due to the continuum yield can be determined by varying the model used to produce the continuum contribution from $b\bar{b}$, e.g. LO vs. NLO. However, the statistics are such that the variation in the shape of the $b\bar{b}$ continuum between LO and NLO does not contribute a significant difference. We can see this in Figure. ??, where the fit of the continuum allows for a removal of the $b\bar{b}$ yield entirely, as long as the Drell-Yan contribution is kept. So, in this analysis, the systematic uncertainties in the continuum yield due to the choice of models is negligible.

In this analysis, we see that the difference between the bin-by-bin counting method and the fitting method is negligible. The single-bin counting method yield is lower than the one from the bin-by-bin counting method by 9%, which we assign as a component of the systematic uncertainty.

Table 6.1 also lists the yield of $\Upsilon(1S+2S+3S)$ and its associated uncertainty obtained directly from the fit, as well as the contribution from Drell-Yan and $b\bar{b}$ discussed in the previous section. As mentioned above, this has the advantage that the uncertainty due to the continuum subtraction and the correlations between the Υ , Drell-Yan and $b\bar{b}$ contributions are automatically taken into account. The disadvantage is that there is a model dependence on the line-shapes used for the fit. This disadvantage will be very important when we discuss the Au+Au results later on in this Chapter. The counting methods of extracting the Υ yield reduce the model dependence on the Υ line shape. Since the uncertainty in the continuum contribution should include similar correlations between the Υ yield and continuum yields as found in the fitting method, we use the same relative Υ yield uncertainty for the counting

methods as for the fitting method.

To get the total Υ yield we must correct for the reconstructed Υ mass yield outside the integration region. This correction can be obtained from the fitted Crystal-Ball functions, and gives an additional 9% contribution to the Υ yield. We report results for the cross section using the bin-by-bin counting method.

In order to determine the cross-section from the measured yield of $\Upsilon(1S+2S+3S)$, we used the following formula:

$$\sum_{n=1}^3 \mathcal{B}(nS) \times \sigma(nS) = \frac{N}{\Delta y \times \epsilon \times \mathcal{L}}, \quad (6.7)$$

where $\mathcal{B}(nS)$ is the branching fraction for $\Upsilon(nS) \rightarrow e^+e^-$ and $\sigma(nS)$ is the cross section $d\sigma/dy$ for the nS state in the region $|y_\Upsilon| < 0.5$. The value of N is the 67 ± 22 (stat.), which is the measured $\Upsilon(1S+2S+3S)$ yield from the bin-by-bin counting method in Table 6.1 with a 9% correction to account for the yield outside $8 < m_{ee} < 11$ GeV/ c^2 . And finally $\Delta y = 1.0$ is the rapidity interval for our kinematic region $|y_\Upsilon| < 0.5$.

The total efficiency for reconstructing members of the Υ family is the product $\epsilon = \epsilon_{\text{geo}} \times \epsilon_{\text{vertex}} \times \epsilon_{\text{L0}} \times \epsilon_{\text{L2}} \times \epsilon_{\text{TPC}} \times \epsilon_R \times \epsilon_{dE/dx} \times \epsilon_{E/p}$. The symbols are as follows: ϵ_{geo} is the BEMC geometrical acceptance, ϵ_{vertex} is the vertex-finding efficiency, ϵ_{L0} and ϵ_{L2} are the trigger efficiencies for L0 and L2, respectively, ϵ_{TPC} is the TPC geometrical acceptance times tracking efficiency for reconstructing both daughters in the TPC, ϵ_R is the TPC-BEMC η - φ matching efficiency, $\epsilon_{dE/dx}$ is the electron iden-

tification efficiency from the specific ionization requirement, and $\epsilon_{E/p}$ is the electron identification efficiency from the E/p selection.

We find for the cross section at midrapidity in $\sqrt{s} = 200$ GeV $p + p$ collisions the result

$$\sum_{n=1}^3 \mathcal{B}(nS) \times \sigma(nS) = 114 \pm 38^{+23}_{-24} \text{ pb} . \quad (6.8)$$

The uncertainties quoted are the 33% statistical+fit uncertainty (mentioned in the discussion of Table 6.1) and the systematic uncertainty, respectively.

Systematics

The major contributions to the systematic uncertainty are: in the choice of bin-counting method, the integrated luminosity, the BBC efficiency for $p + p$ NSD events and the L0 trigger efficiency for Υ events. The polarization of the Υ states also affects the estimation of the geometrical acceptance. This uncertainty was estimated by comparing simulations of fully longitudinal and fully transverse decays and comparing the acceptance of these cases with the unpolarized case. A list of all corrections and systematic uncertainties in the procedure to extract the cross section is compiled in Table 6.1.2. The combined systematic uncertainty is obtained by adding all the sources in quadrature. Since the single-particle efficiencies enter quadratically when reconstructing dielectron pairs, we multiply the single-particle uncertainty by a factor of 2 when estimating the pairwise uncertainty.

The result we obtained for the cross-section is shown in Figure 6.4, where our

Table 6.2. Systematic uncertainties on the measurement of the Υ cross section.

Quantity	Value	Syst. uncertainty on $d\sigma/dy$ (%)
$N_{+-} - 2\sqrt{N_{++}N_{--}}$	82.7	$^{+0}_{-9}$
\mathcal{L}	7.9 pb $^{-1}$	± 7
ϵ_{BBC}	0.87	± 9
ϵ_{geo}	0.57	$^{+3.0}_{-1.7}$
ϵ_{vertex}	0.96	± 1.0
ϵ_{L0}	0.43	$^{+7.5}_{-5.9}$
ϵ_{L2}	0.85	$^{+0.7}_{-0.2}$
ϵ_{TPC}	0.85 2	$2 \times \pm 5.8$
ϵ_R	0.93 2	$2 \times ^{+1.1}_{-0.2}$
$\epsilon_{dE/dx}$	0.84 2	$2 \times \pm 2.4$
$\epsilon_{E/p}$	0.93 2	$2 \times \pm 3.0$
Combined		$^{+22.8}_{-24.1}$ pb

measurement is represented by the star. The error bars and the box depict the statistical and systematic uncertainties, respectively. To illustrate the acceptance in rapidity, we also show the unlike-sign pairs after like-sign background subtraction in the Υ region $8 < m_{ee} < 11$ GeV/ c^2 as a hashed histogram. The cross-section measurement is then compared to a NLO CEM predictions [25] of the $\Upsilon(1S)$ rapidity distribution. Since we measure all three states only in the di-electron channel, the calculation of the $\Upsilon(1S)$ is scaled by a factor

$$\frac{\mathcal{B}(1S) \times \sigma(1S) + \mathcal{B}(2S) \times \sigma(2S) + \mathcal{B}(3S) \times \sigma(3S)}{\sigma(1S)} \quad (6.9)$$

in order to compare it to our measurement. The branching ratios and cross-sections used are from Table 4.2.

The calculation is in agreement with our measurement. The two dotted lines in the plot are the upper and lower bounds of the cross-section obtained from a

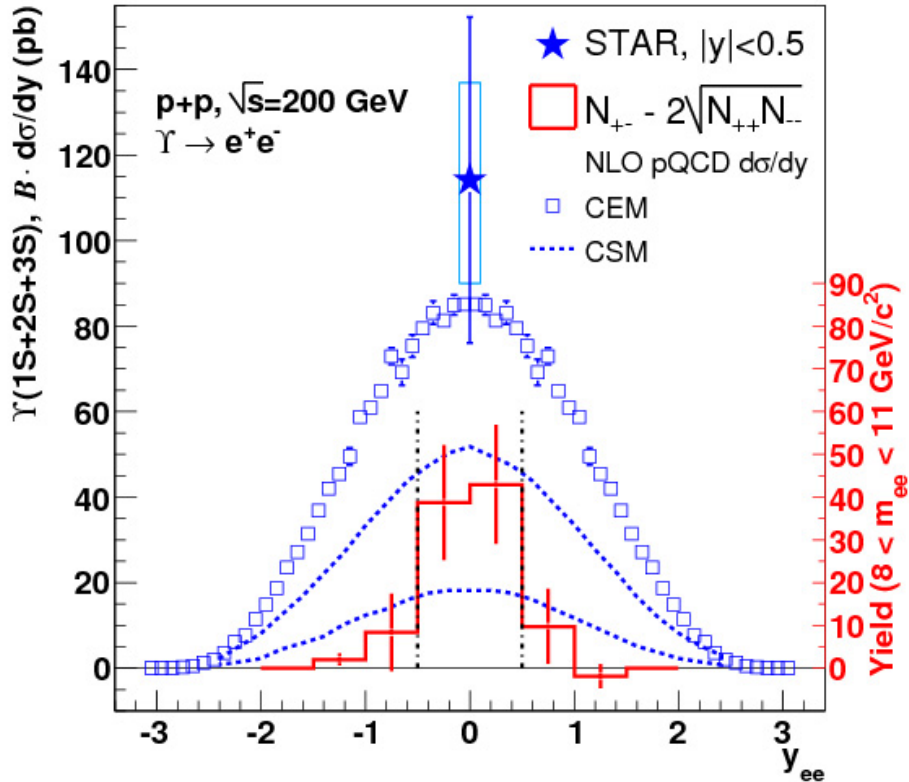


Figure 6.4. The STAR measurement of the $\Upsilon(1S + 2S + 3S)_{|y|<0.5}$ cross-section times branching ratio into electrons. The error bars are statistical, the shaded box shows the systematic uncertainty with the scale given by left axis. The raw Υ yield vs. y is shown by the histogram at the bottom, with scale on the right axis. The cross-section was calculated from the yield between the vertical dot-dashed lines. The open squares are from a NLO CEM calculation, and the area between the dotted lines is the prediction from a NLO CSM calculation of the Υ cross-section (see text).

calculation in the CSM for direct $\Upsilon(1S)$ production [16] based on NLO code developed for quarkonium production at hadron colliders [87]. Since the calculation is only for the direct $\Upsilon(1S)$ state to compare it to our measurement, which includes all 3 states and feed-down contributions, we scaled the calculation by dividing it by a factor 0.42 to account for this (see Ref [16] for details). The CSM prediction is lower than our data, indicating that additional contributions are needed beside production via color

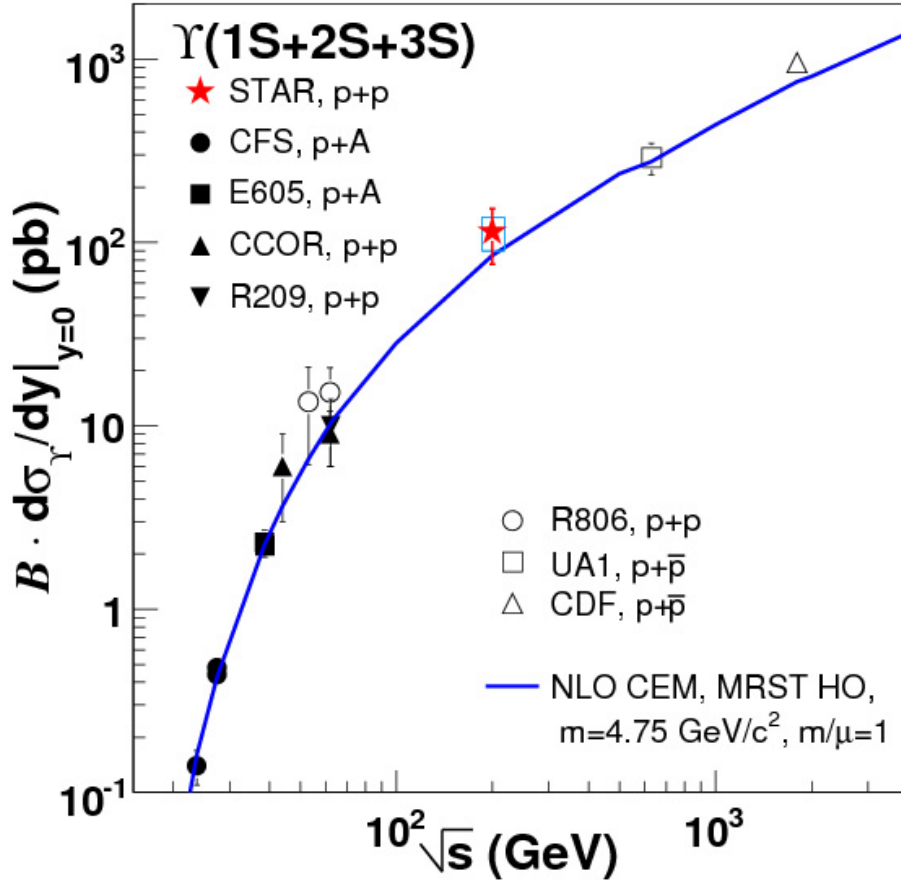


Figure 6.5. Measurements of the $\Upsilon(1S + 2S + 3S)$ cross-section versus center-of-mass energy for the world data compared to a NLO CEM calculation. The error bars on the STAR point are statistical and the box is systematic.

singlet, as mentioned in Chapter 2.

In Figure 6.5, we also compare our $\Upsilon(1S + 2S + 3S)$ result with measurements done in $p + A$, $p + p$ and $p + \bar{p}$ collisions at center-of-mass energies ranging from 20 GeV up to 1.8 TeV [?, 78, 88, 87, 89, 90, 91], and to NLO CEM predictions [32] for a wide range of center-of-mass energies.

Our result is consistent with the trend, and provides a reference for bottomonium production at the top RHIC energy that will be used to calculate R_{AA} in the following sections.

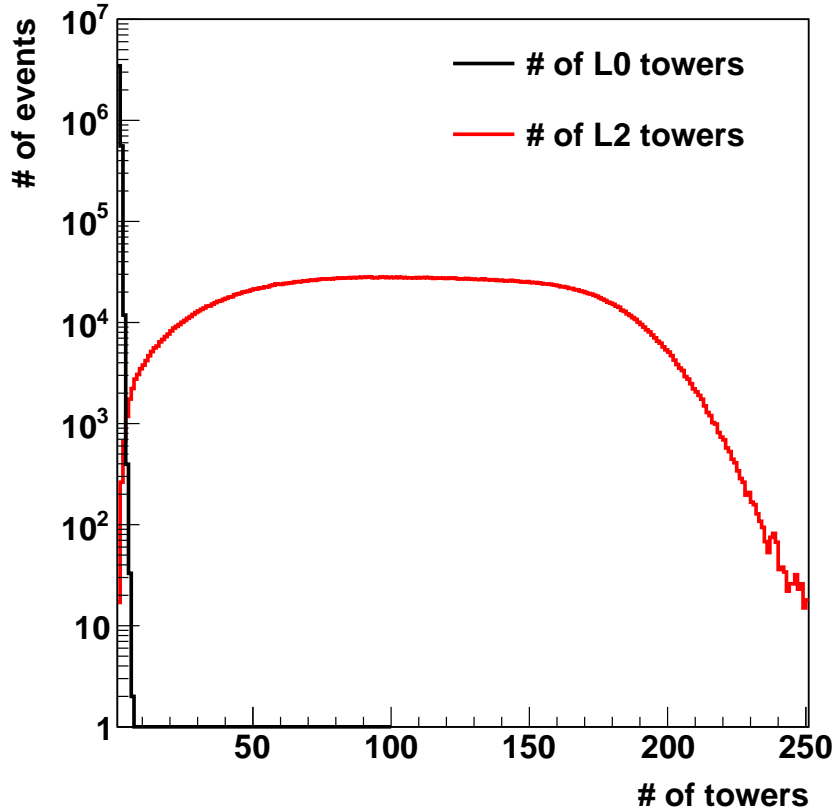


Figure 6.6. The number of towers that satisfied the L0 trigger condition for the 2007 Au+Au Υ trigger is in black. The number that satisfy the L2 trigger condition are in red. Every event has at least 1 tower that satisfies the L0 condition, and at least 2 that satisfy the L2 trigger condition since every tower that satisfies L0 also satisfies L2.

6.2 Υ in Au+Au: Results from 2007

6.2.1 Line-Shape

Given our current detector resolution and statistics, we were unable to separate the three Υ states in our Au+Au analyses. In order to recover the number of measured Υ 's, we need to be able to fit the like-sign subtracted invariant mass spectrum with a line-shape that includes contributions from the Drell-Yan, uncorrelated $b\bar{b}$ pairs, and the $\Upsilon(1S + 2S + 3S)$ states. However, the $b\bar{b}$ continuum and the $\Upsilon(1S + 2S + 3S)$

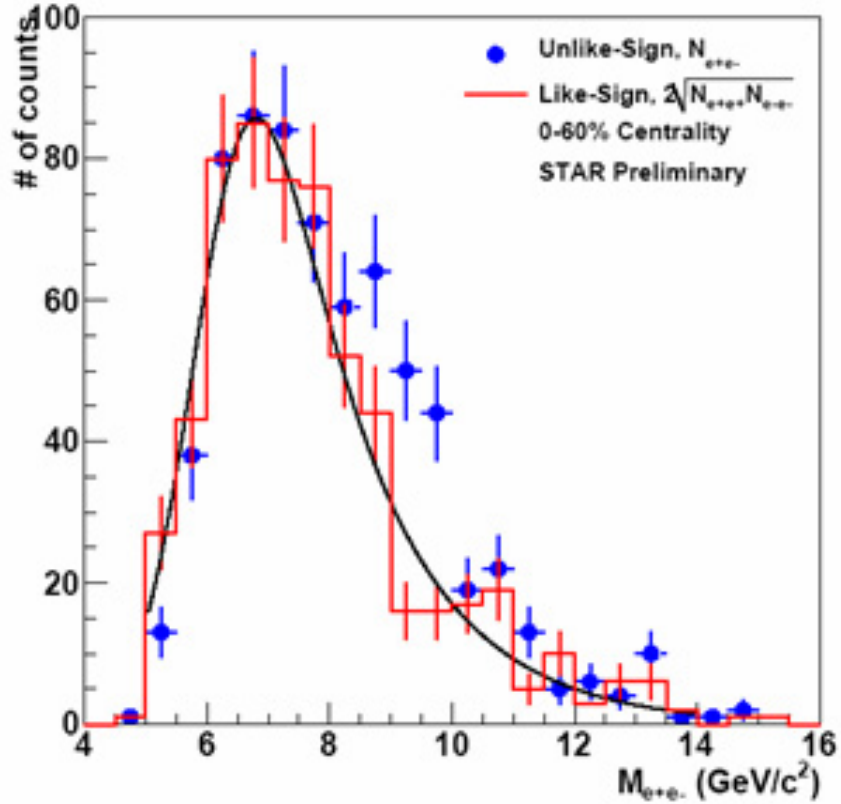


Figure 6.7. The unlike-sign di-electron spectrum for 0-60% central events is shown as the blue circles. The sum of the like-sign spectra is shown as the red histogram. The solid line is a fit to the like-sign background.

states will be modified by the medium. Given the statistics, it would be unwise to fit this function with five free parameters. There are large uncertainties in our yield of $\text{Drell-Yan} + b\bar{b} \rightarrow e^+e^-$ as indicated in Chapter 3, so even scaling this contribution by N_{bin} would not improve the fit uncertainty.

The method to extract the Υ was developed as follows. A functional form of the line-shape with two free parameters would be fit to the like-sign subtracted invariant mass spectrum, with the two free-parameters being the total yield of the Drell-Yan + $b\bar{b}$ background and the the total yield of the Υ . The line-shape for each individual Υ

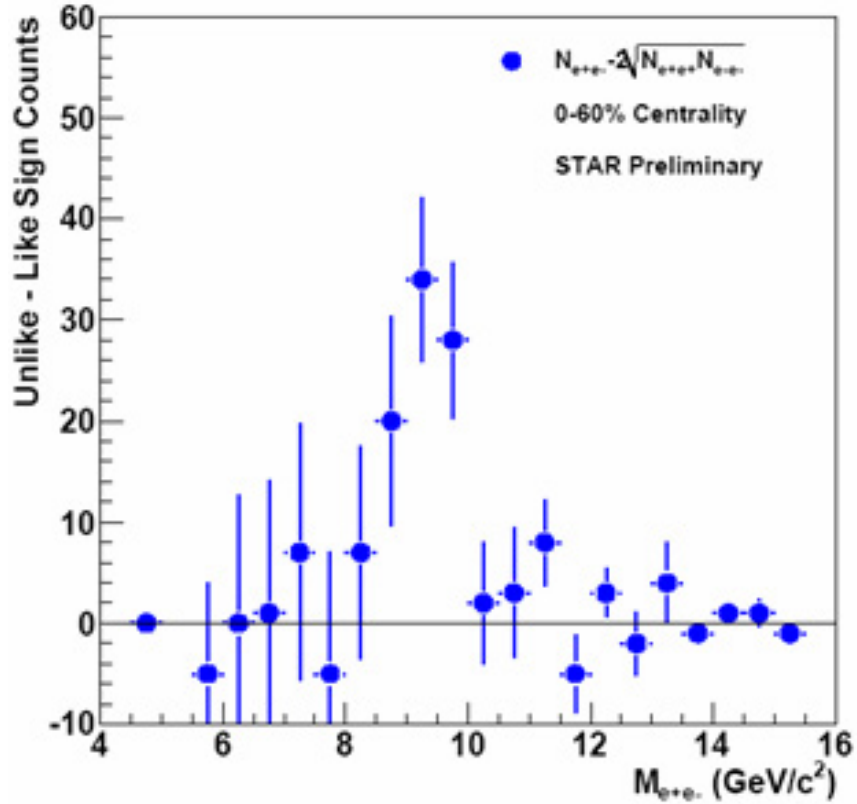


Figure 6.8. The unlike-sign subtracted background for 0-60% central events.

state is a Crystal-Ball function as described in Chapter 3, with the same parameters. Further explanation for this choice is given in Section 5.1.3. The Drell-Yan + $b\bar{b}$ continuum was parameterized with the equation $A/(1 + m/m_0)^n$ where $n = 4.69$ and $m_0 = 2.7$, multiplied by an erf determined in the fit to the like-sign background. This method is outlined in more detail in Chapter 3. The ratios of the $\Upsilon(1S)$ to $\Upsilon(2S)$ and the $\Upsilon(1S)$ to $\Upsilon(3S)$ were held fixed to the same ratios used in the $p + p$ analysis. We do not expect these ratios to remain the same, however since we do not know how much these ratios will change this is one way to extract the total yield of the Drell-Yan and $b\bar{b}$ background. We do not calculate the yield of the $\Upsilon(1S + 2S + 3S)$

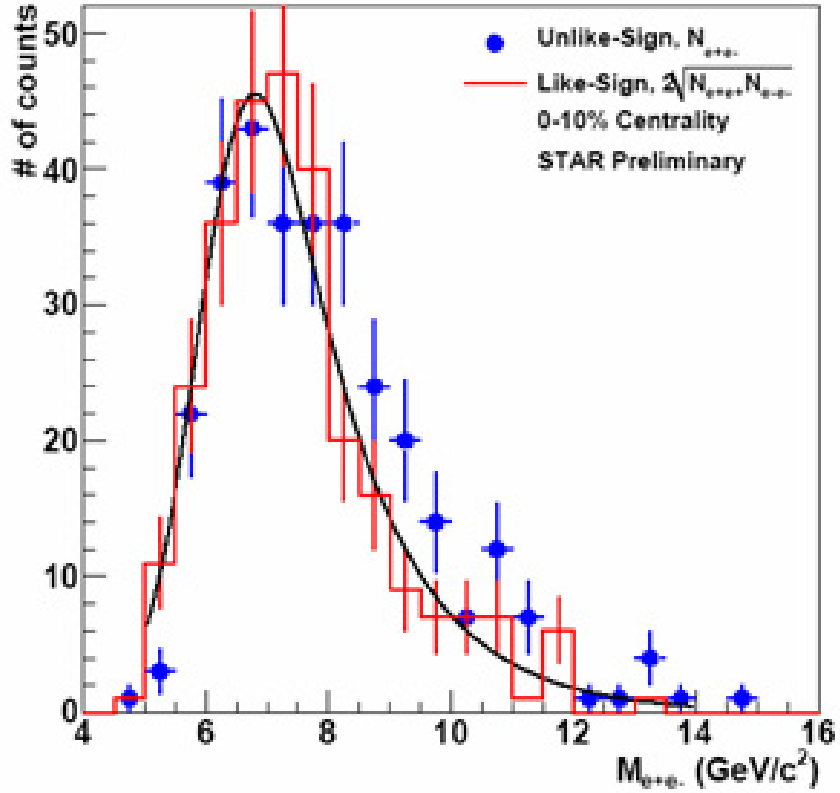


Figure 6.9. The unlike-sign di-electron spectrum for 0-10% central events is shown as the blue circles. The sum of the like-sign spectrums is shown as the red histogram. The solid line is a fit to the like-sign background.

from the fit.

6.2.2 Υ yield

To determine the $\Upsilon(1S + 2S + 3S)$ yield, we subtract the integral of the Drell-Yan and $b\bar{b}$ yield in the mass window of $8 < m < 12 \text{ GeV}/c^2$. The pure counts in the like-sign subtracted histogram should not depend on the ratio of the various Υ states so the result will be mostly unbiased. The statistical uncertainty in the Υ yields comes directly from the fit, however, as Minuit will calculate the statistical uncertainty and

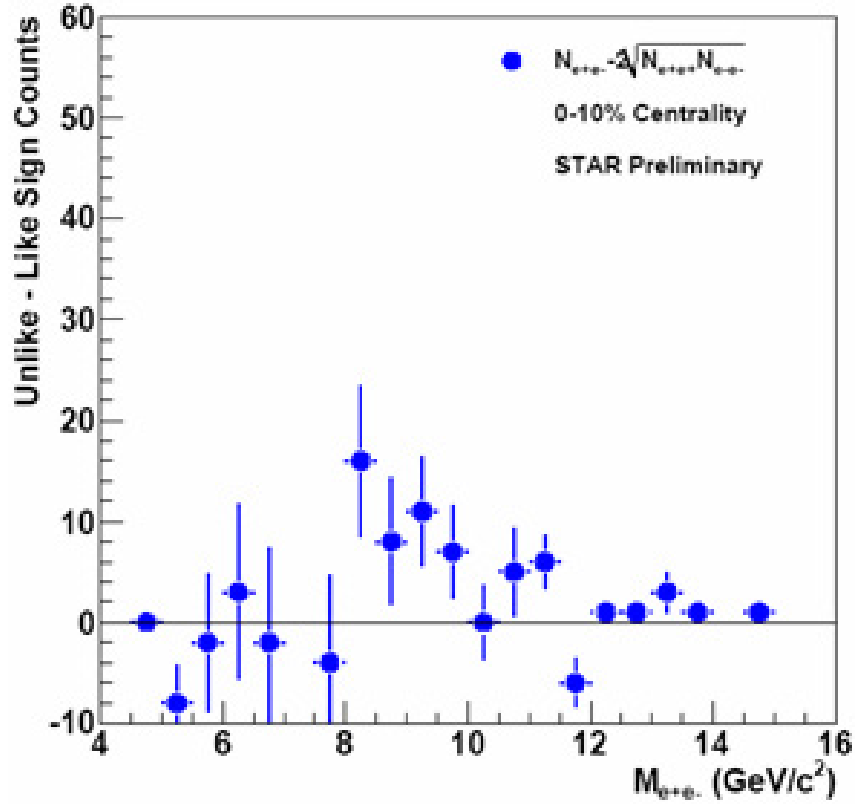


Figure 6.10. The unlike-sign subtracted background for 0-10% central events.

properly take into account the correlations between the yield of the Drell-Yan and $b\bar{b}$ continuum compared to the Υ yield. To determine the systematic uncertainty of this method, it was repeated with only the $\Upsilon(1S)$ mass-peak, which is the most extreme assumption of what the possible physics there could be. This fit results in a different yield for the Drell-Yan and $b\bar{b}$ background, which in turn will give a different yield for the number of Υ 's.

The data were divided into two centrality bins, 0-10% and 0-60%. It is assumed that if there is a QGP effect on the Υ yield, it would be stronger in the more central collisions. In Table 6.3 the raw yields for both centrality bins are listed. The signifi-

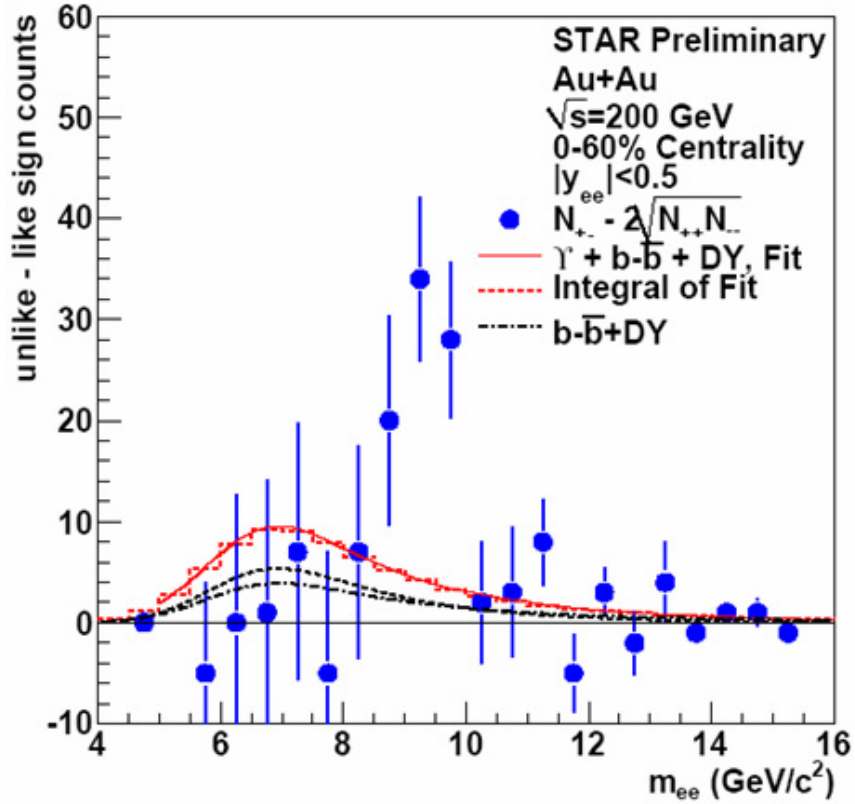


Figure 6.11. The di-electron spectrum from 0-60% fit with the assumption that there was no Υ 's in this data-set. The fit had a χ^2/DOF of 5.6, indicating this scenario is unlikely.

cance of the signal is 4.6 in 0-60% and 3.3 in 0-10%. However, this signal is the yield of the $\Upsilon(1S + 2S + 3S) + \text{Drell-Yan} + b\bar{b}$. The significance of the Υ signal extracted from of these values will have to be less.

The first question that needs to be asked is whether we could adequately explain the measured di-electron spectrum with only the Drell-Yan and $b\bar{b}$ background. In short, do we see an Υ signal in this data? This fit is shown in Figure 6.11, where the parameters for the Drell-Yan and $b\bar{b}$ background were identical to those used in 6.1.1 with the exception that the width and thickness of the erf come from the fit

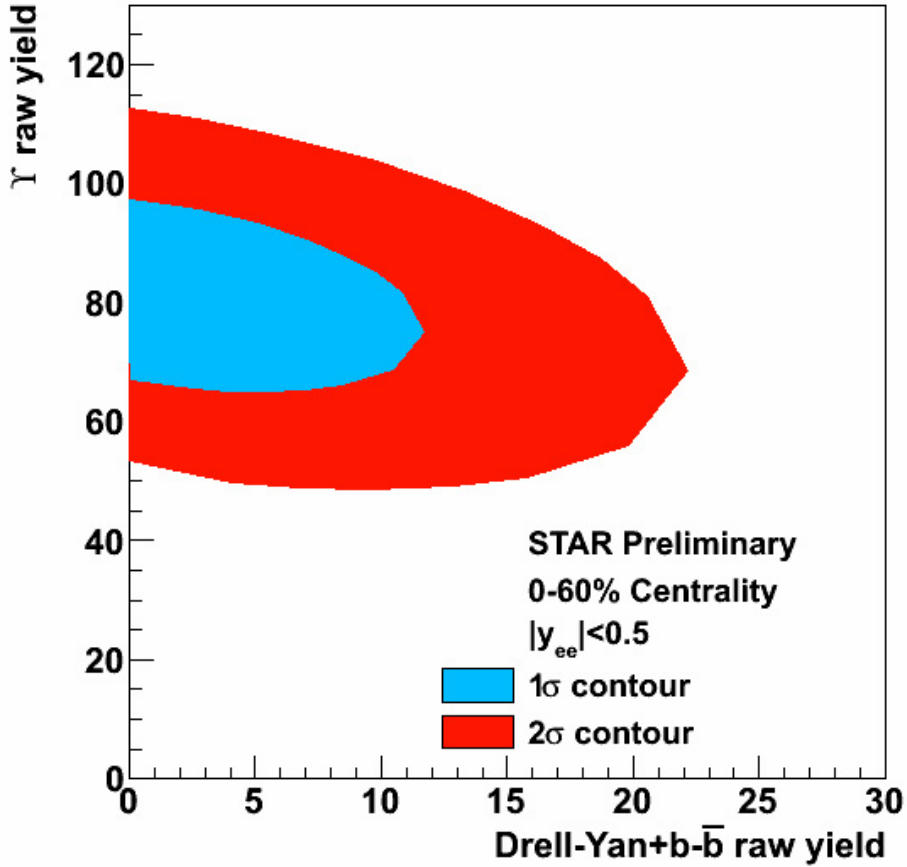


Figure 6.12. The correlation between the raw $\Upsilon(1S + 2S + 3S)$ yield and the raw Drell-Yan and $b\bar{b}$ yield in 0-60% centrality from the 2007 data-set. The Υ yield is calculated directly from the fit.

shown in Figure 6.7. The Υ yield was forced to zero. In this case, since there were only two free parameters, the Drell-Yan and the $b\bar{b}$ yields were both allowed to be free parameters. The resulting fit had a χ^2/DOF of 5.6, indicating that this scenario is unlikely. This can also be seen in the correlation between the raw Υ yield and the yield of Drell-Yan and $b\bar{b}$ shown in Figure 6.12. In answer to our first question, we did see evidence of Υ in 0-60% centrality in our 2007 data run.

The total $\Upsilon(1S + 2S + 3S)$ efficiency is 0.0668 if we combine the results from embedding with the data-driven PID results. Using this value, the $\Upsilon(1S + 2S + 3S)$

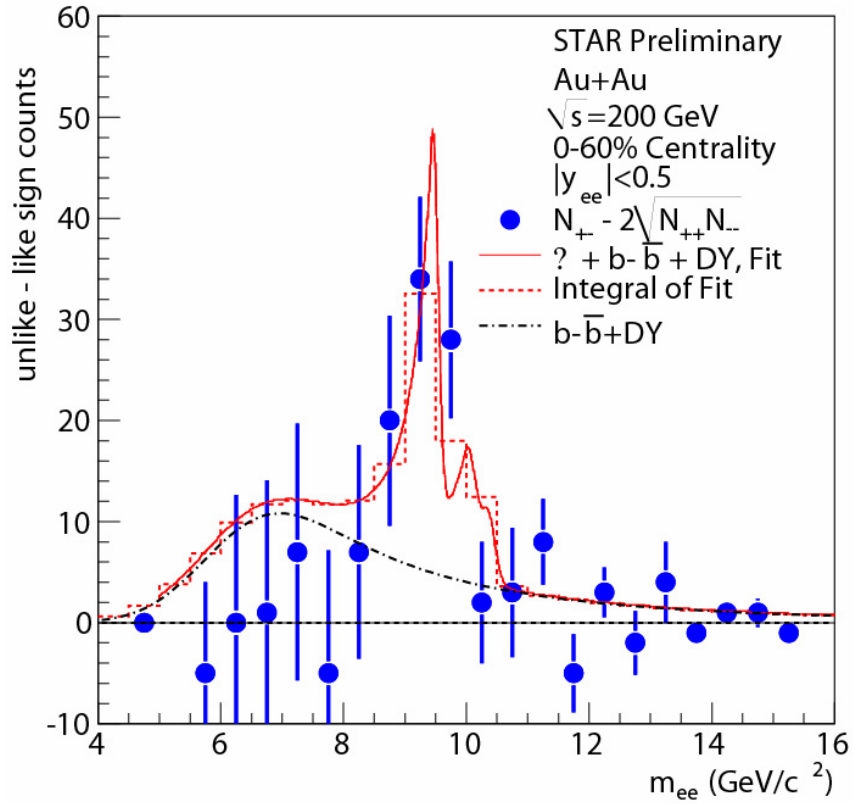


Figure 6.13. The like-sign spectrum as shown in Figure 6.8 fit with a functional form that had two free-parameters, the total yield of the $\Upsilon(1S + 2S + 3S)$ and the total yield of the Drell-Yan and $b\bar{b}$ continuum.

yields in Table 6.3, the cross-section from Chapter 3, and the N_{bin} as calculated in 5.1.1 we get the following R_{AA} results.

$$R_{AA}(0 - 60\%) = 0.80 \pm 0.34(stat.)$$

$$R_{AA}(0 - 10\%) = 0.67 \pm 0.42(stat.)$$

This can be seen in Figure 6.16. While we can definitely say that we have made a measurement of $\Upsilon(1S + 2S + 3S)$ in this Au+Au data-set, we can not claim anything further. Given the statistics, we can make a case that suppression or non-suppression are both possible scenarios. However, this analysis was repeated with better statistics

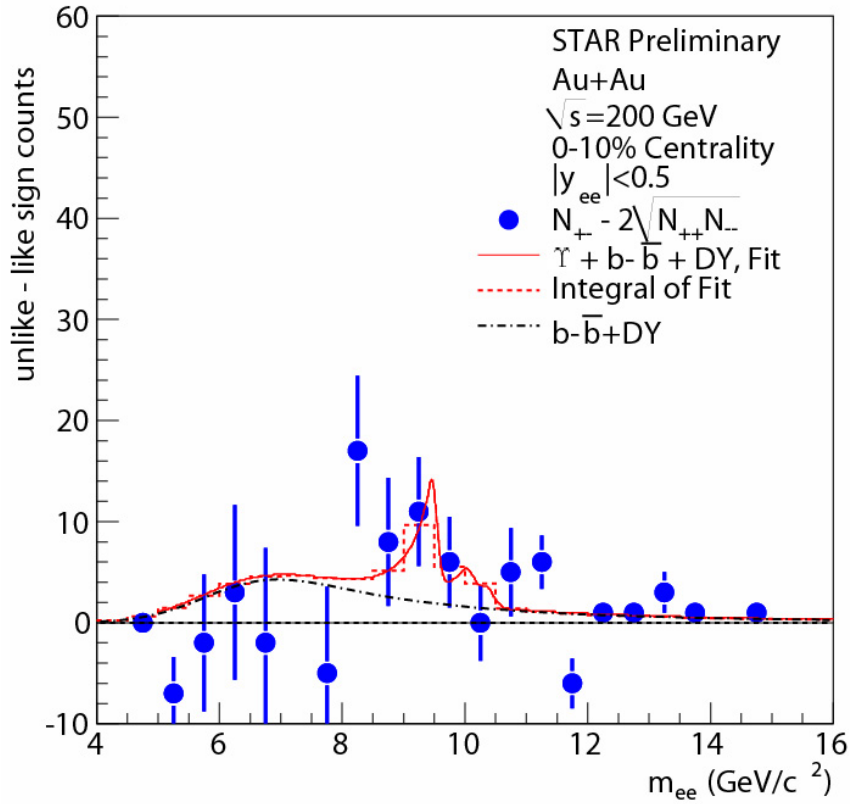


Figure 6.14. The like-sign spectrum as shown in Figure 6.10 fit with a functional form that had two free-parameters, the total yield of the $\Upsilon(1S + 2S + 3S)$ and the total yield of the Drell-Yan and $b\bar{b}$ continuum.

and in more depth for the 2010 Au+Au data set. These results will be discussed starting in 5.2.

6.3 Υ in Au+Au: Results from 2010

6.3.1 Υ yield and R_{AA}

The results for the four centrality bins in question are shown in Figures 6.17–6.20.

The summary of their results can be found in Table 6.4.

Table 6.3. The results in this table are from the the 2007 run. Total number of counts in the unlike-sign (N_{+-}), like-sign positive (N_{++}), and like-sign negative (N_{--}) di-electron invariant mass distributions in the region between $8 < m < 12 \text{ GeV}/c^2$. The background, B , is calculated as the sum of the two like-sign distributions and the signal, S , is the background subtracted unlike-sign distribution. The distributions for this numbers are shown in Figure 6.7–6.10. The $\Upsilon(1S + 2S + 3S)$ yield as extracted by the fits shown in Figures 6.13 and 6.14 are also shown.

	0-60%	0-10%
N_{+-}	276 ± 16	119 ± 10
N_{++}	100 ± 10	41 ± 6
N_{--}	79 ± 9	31 ± 6
B	179 ± 13	72 ± 8
S	97 ± 21	47 ± 14
$\Upsilon(1S + 2S + 3S)$	64 ± 16	21 ± 11

Table 6.4. The results in this table are from the the 2010 run. Total number of counts in the unlike-sign (N_{+-}), like-sign positive (N_{++}), and like-sign negative (N_{--}) di-electron invariant mass distributions in the region between $8 < m < 12 \text{ GeV}/c^2$. The background, B , is calculated as the sum of the two like-sign distributions and the signal, S , is the background subtracted unlike-sign distribution. The significance is the significance of the signal, S , which is the sum of the $\Upsilon(1S + 2S + 3S)$ and the Drell-Yan and $b\bar{b}$ continuum yields.

	0-60%	0-10%	10-30%	30-60%
N_{+-}	640 ± 25	243 ± 16	267 ± 16	130 ± 11
N_{++}	149 ± 12	74 ± 9	58 ± 8	17 ± 4
N_{--}	181 ± 13	66 ± 8	75 ± 9	34 ± 6
S	310 ± 31.1	103 ± 19.6	134 ± 20.0	79 ± 13.4
Significance	10.0	5.3	6.7	5.9
$\Upsilon(1S + 2S + 3S)$	196.6 ± 35.8	51.5 ± 25.5	91.3 ± 22.6	48.1 ± 15.5
Υ Significance	5.5	2.0	4.0	3.1

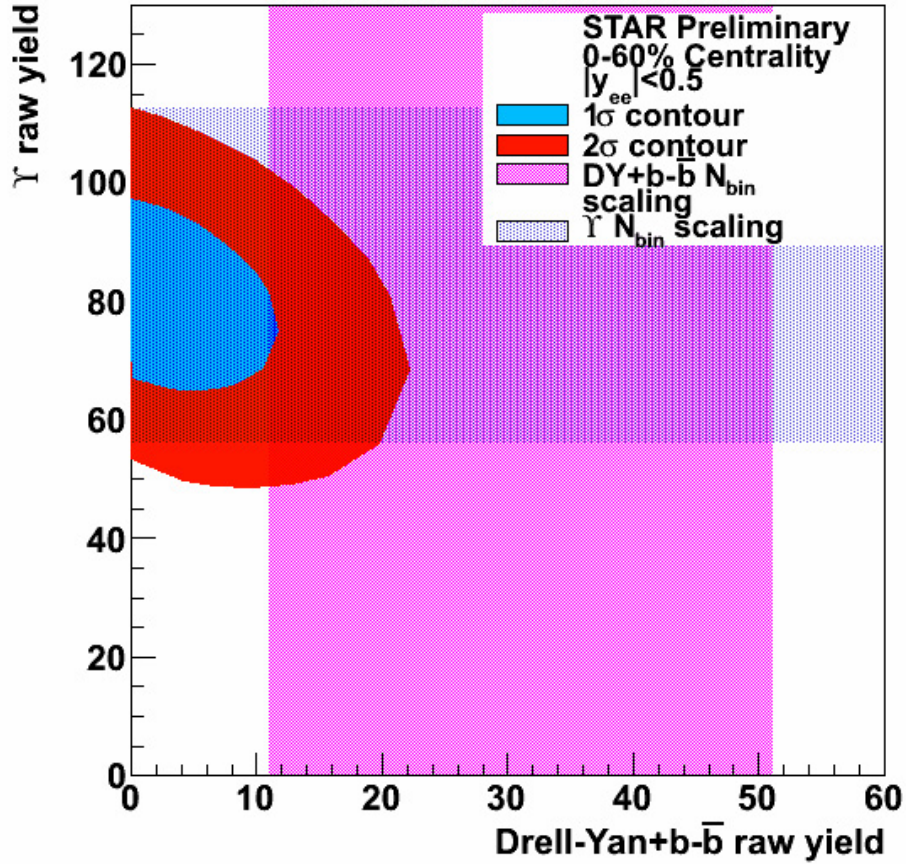


Figure 6.15. This is Figure 6.12 with the additional bands showing what we would expect for the yields of the $\Upsilon(1S + 2S + 3S)$ and the Drell-Yan and $b\bar{b}$ background if we simply scaled the $p + p$ results from Chapter 3 by N_{bin} . This shows that we are consistent with an $R_{AA}^{\Upsilon+DY+b\bar{b}} = 1$. However the uncertainty is large enough that almost any suppression model is not excluded.

The $\Upsilon(1S + 2S + 3S)$ yield was extracted from the unlike-sign subtracted invariant mass spectrum in the same fashion as in Section 6.2.2. The $\Upsilon(1S + 2S + 3S)$ yield is the result of the integral of the Drell-Yan and $b\bar{b}$ background subtracted from the unlike-sign subtracted invariant mass spectrum. The statistical uncertainty of the yield is the percentage uncertainty from the fit multiplied by the calculated yield. The uncertainty was calculated in this manner in order to properly account for the correlation between the Υ yield and the continuum yield.

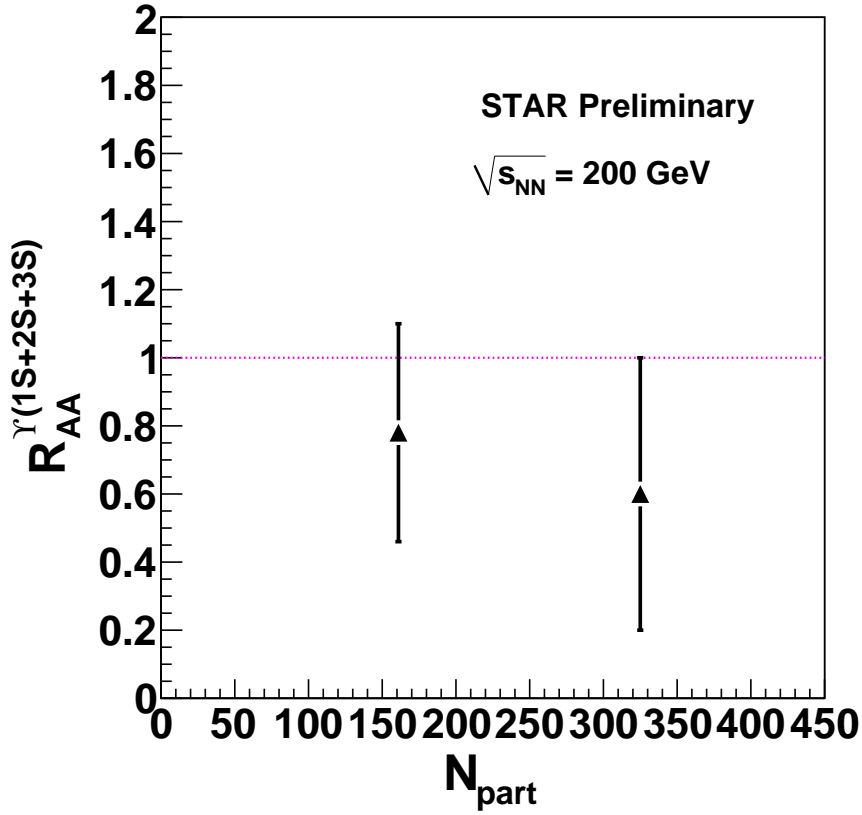


Figure 6.16. Shown here is the R_{AA} from the 2007 data set. The error bars are statistical only. The point on the right for 0-10% centrality is a subset of the point for 0-60% centrality.

Using the N_{mbAA} and N_{bin} results from Table 5.4, the PID efficiency calculated in Section 5.2.1 and the trigger and tracking efficiency from embedding the R_{AA} values versus centrality listed in Table ?? the R_{AA} of $\Upsilon(1S + 2S + 3S)$ versus centrality are listed in Table 6.3.2.

6.3.2 Systematics

One advantage to using R_{AA} as a measurement is that most of the systematics cancel, assuming that the $p + p$ and Au+Au results were both taken with the same

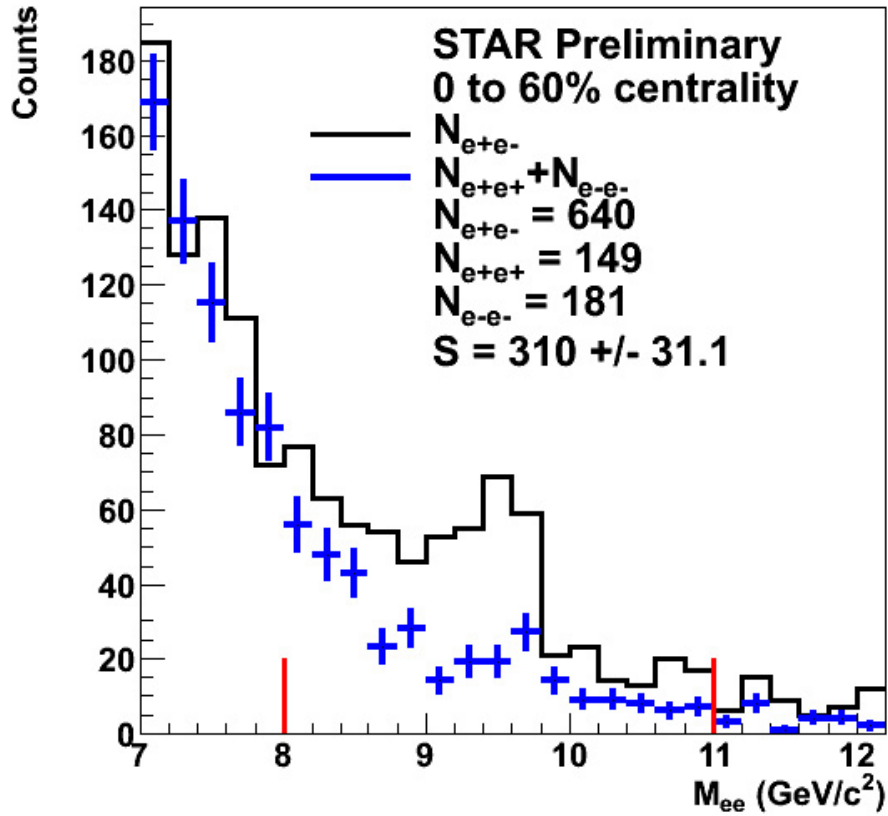


Figure 6.17. The unlike-sign di-electron spectrum for 0-60% central events is shown as the blue circles. The sum of the like-sign spectra is shown as the red histogram.

detectors, which is true in our case. The total systematic uncertainty for our $p + p$ cross-section is listed in Table 6.1.2. The major sources of systematics from that table that do not cancel with systematics in our Au+Au results are the uncertainty in the luminosity and the uncertainty in the BBC efficiency. The two added in quadrature give a $p + p$ systematic uncertainty of 11%. This systematic uncertainty is common to all of the centrality bins, as is the 38% statistical uncertainty from that analysis.

Of the other systematic uncertainties listed in Table 6.1.2, several may contribute to the R_{AA} systematic uncertainty, though they were neglected for this thesis. The same tracking software was used for both analyses, so the uncertainty due to the track

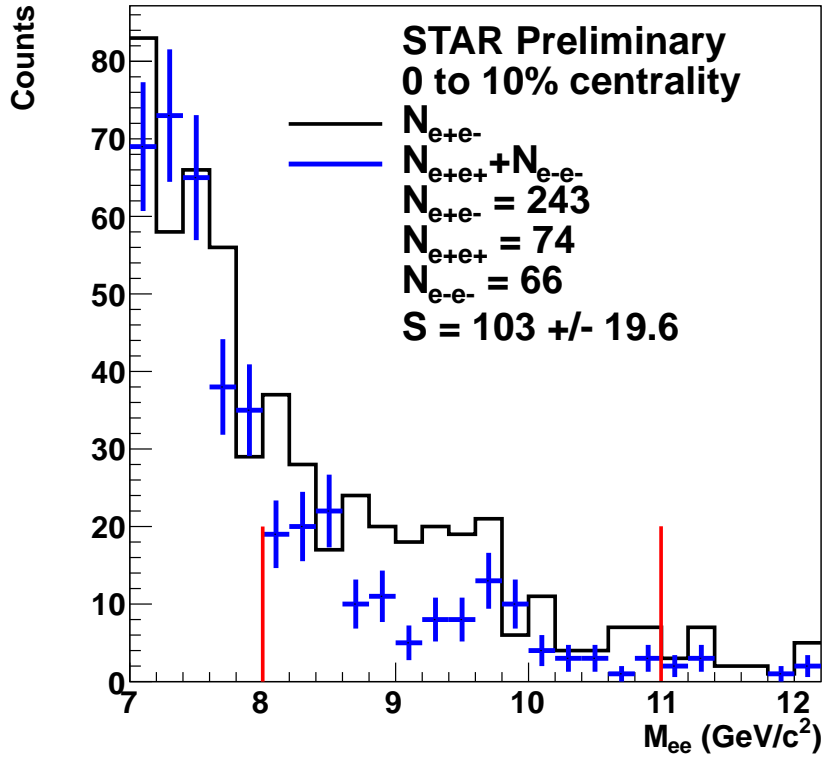


Figure 6.18. The unlike-sign di-electron spectrum for 0-10% central events is shown as the blue circles. The sum of the like-sign spectra is shown as the red histogram.

finding algorithm and associated resolution should be the same. However, the space-charge calibrations for the Au+Au environment versus the $p + p$ environment may be different and this should be investigated. A different vertexer was used for each analysis, but with a vertex finding efficiency nearly at 100% for Υ triggered events, the effect on the Υ yield is very small. The same calibration methods for dE/dx ($n\sigma_{electron}$) were used for both analyses, so the difference between the two should be small. The BEMC is the same for both analyses, so most of the systematics due to this should cancel (E/p and trigger), however the triggers had a different configuration that will contribute to the total systematics. The largest of the systematics in the

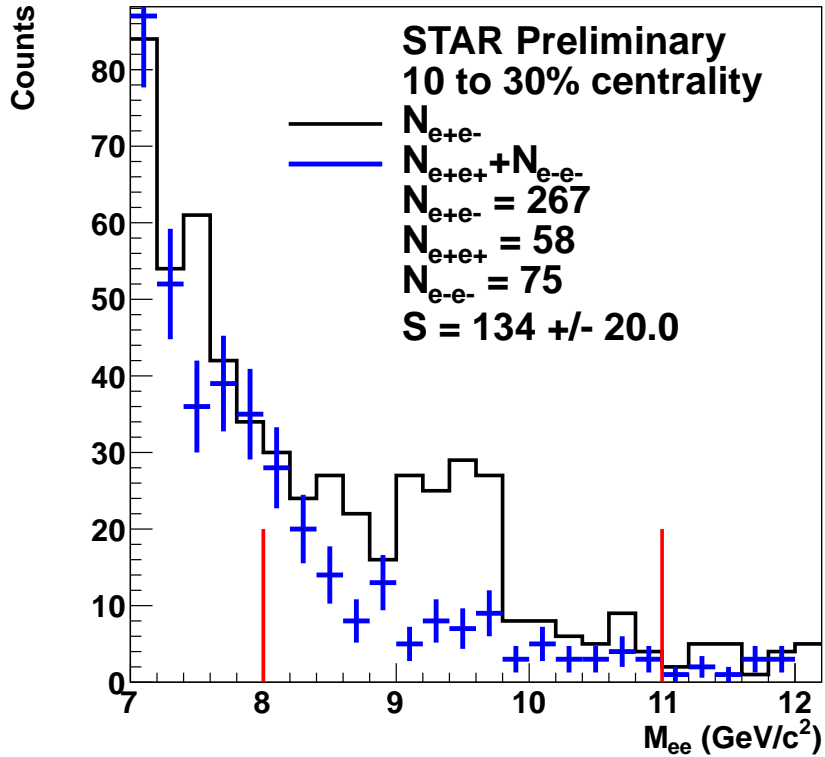


Figure 6.19. The unlike-sign di-electron spectrum for 10-30% central events is shown as the blue circles. The sum of the like-sign spectra is shown as the red histogram.

$p + p$ analysis was the HT threshold. This should mostly cancel with the HT threshold in the Au+Au analysis. However, the threshold of > 16 DSM-ADC from the $p + p$ analysis and > 18 DSM-ADC from the Au+Au analysis occur in slightly different places in the underlying Υ distribution as shown in Figure 4.2

The additional systematics from the Au+Au analysis are the systematics due the centrality definition and the uncertainty in the line-shape as a result of the underlying physics. In the 0-60% centrality region, the trigger efficiency was very near 100%, so within this region we do not need to worry about the efficiency of the trigger with respect to centrality. A weighting scheme would be required were the analyses to

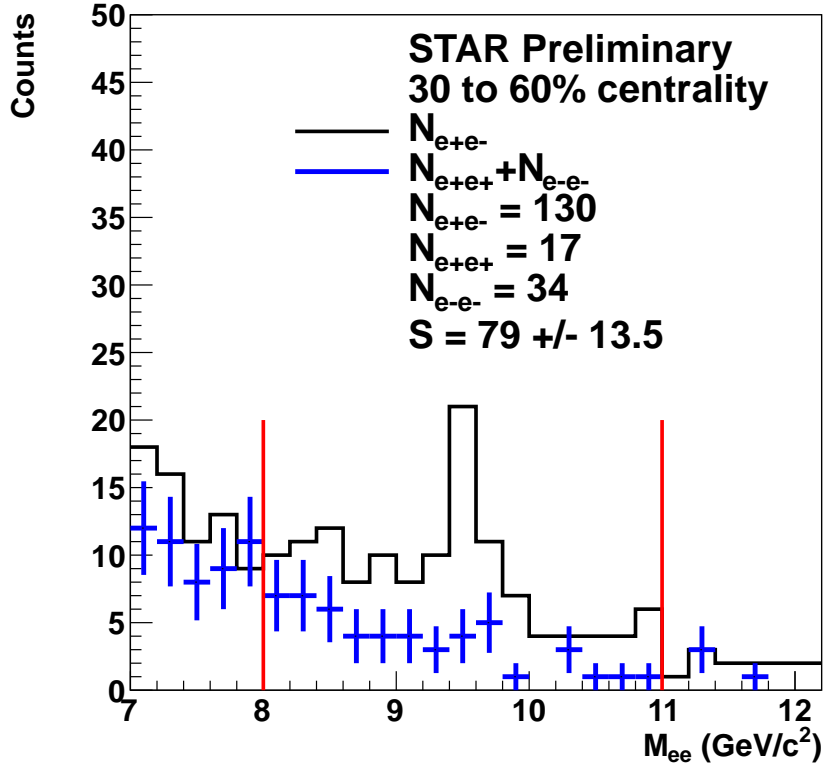


Figure 6.20. The unlike-sign di-electron spectrum for 30-60% central events is shown as the blue circles. The sum of the like-sign spectra is shown as the red histogram.

be extended to more peripheral events. There is an uncertainty in N_{bin} , as listed in Tables 5.4 and 6.3.2, which is specific to each centrality data point. There is the uncertainty in N_{part} , listed in Table 6.3.2.

The line-shape uncertainty can be broken into two parts: the uncertainty in the Drell-Yan and $b\bar{b}$ yield and the uncertainty in the efficiency. The uncertainty in the Drell-Yan and $b\bar{b}$ yield is determined by refitting the invariant mass spectra with only the $\Upsilon(1S)$ state with the Drell-Yan and $b\bar{b}$. Due to their higher masses, the $\Upsilon(2S)$ and $\Upsilon(3S)$ states have a higher L0 trigger efficiency. However, since we determine the yield of the $\Upsilon(1S + 2S + 3S)$ together, we need an estimate of the efficiency of

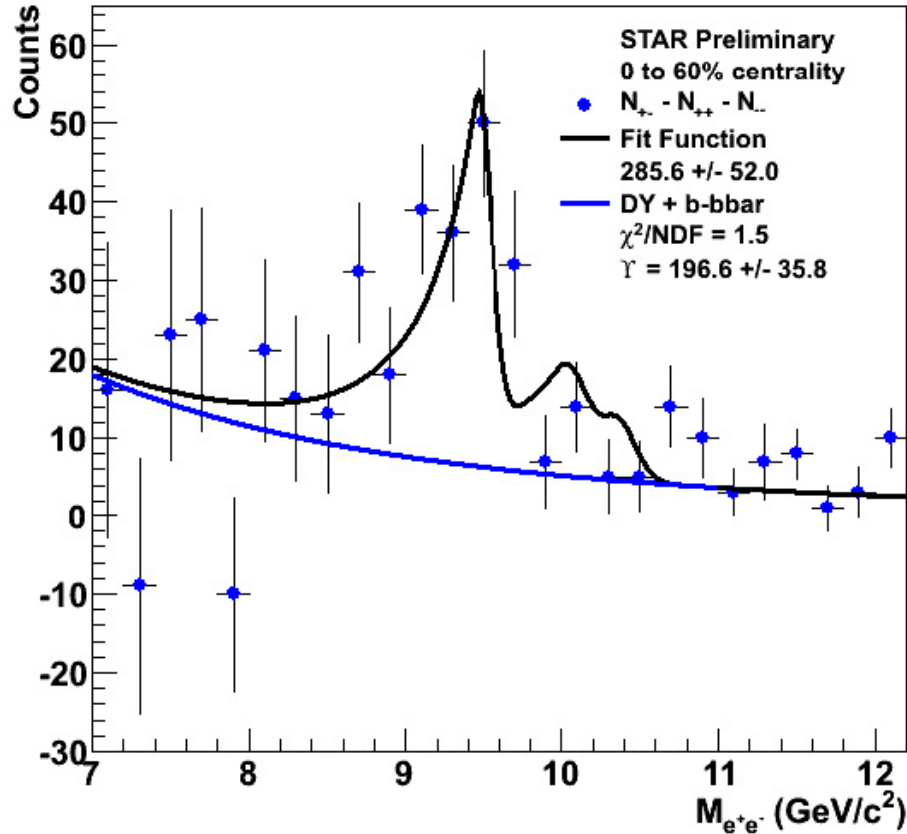


Figure 6.21. The unlike-sign subtracted di-electron spectrum for 0-60% central events is shown with the line-shape fit.

the total yield which requires knowledge of the ratio of the three states. For this analysis, we used the efficiency difference between the $\Upsilon(1S + 2S + 3S)$ and having only the $\Upsilon(1S)$ state. The difference in the total efficiency on the Υ yield due to combination of the trigger efficiency, and the change of efficiency due to the mass integral was determined from simulation to be 5%. The mass integral efficiency is important because we count the number of Υ 's with reconstructed masses between 8 and 12 GeV/c^2 . But, due to the Brehmstrahlung tail and detector resolution, some of the $\Upsilon(1S)$ yield has a reconstructed mass of $m < 8 \text{ GeV}/c^2$. The results are shown in Figure 6.25.

Table 6.5. Systematics for the 2010 analysis. The first row is the total Υ yield if we assume that only the $\Upsilon(1S)$ survives. The second row is the percent uncertainty of this effect and including the 5% difference in the efficiency. The third row is the percent uncertainty due to N_{bin} .

	0-60%	0-10%	10-30%	30-60%
$\Upsilon(1S)$ yield	150.8	45.8	67.8	36.1
Total %	-0.18	-0.06	-0.21	-0.20
unc N_{bin}	± 0.069	± 0.029	± 0.065	± 0.17
Sys. Unc.	+0.069/-0.193	+0.029/-0.096	+0.065/-0.220	+0.170/-0.262

Table 6.6. The first four rows of each centrality are all the values need to calculate R_{AA} . The fifth row is the calculation of R_{AA} given these values, only using the uncertainty from the Au+Au analysis. Since the $p+p$ uncertainties apply to all points, it is useful to break them out separately. The sixth row has the $p+p$ uncertainties added in quadrature. The results are displayed in Figure 6.25

	0-60%	0-10%
$\Upsilon(1S + 2S + 3S)$	196.6 ± 35.8	51.5 ± 25.5
ϵ_{all}	0.079	0.075
N_{mbAA}	4.49×10^9	7.09×10^8
N_{bin}	393 ± 27	962 ± 28
R_{AA}	$0.52 \pm 0.09(\text{stat.})_{-0.10}^{+0.04}(\text{sys.})$	$0.37 \pm 0.18(\text{stat.})_{-0.04}^{+0.01}(\text{sys.})$
R_{AA}	$0.52 \pm 0.20(\text{stat.})_{-0.12}^{+0.07}(\text{sys.})$	$0.37 \pm 0.22(\text{stat.})_{-0.06}^{+0.04}(\text{sys.})$
	10-30%	30-60%
$\Upsilon(1S + 2S + 3S)$	91.3 ± 22.6	48.1 ± 15.5
ϵ_{all}	0.079	0.078
N_{mbAA}	1.57×10^9	2.21×10^9
N_{bin}	493 ± 32	138 ± 24
R_{AA}	$0.55 \pm 0.14(\text{stat.})_{-0.12}^{+0.04}(\text{sys.})$	$0.74 \pm 0.24(\text{stat.})_{-0.19}^{+0.13}(\text{sys.})$
R_{AA}	$0.55 \pm 0.23(\text{stat.})_{-0.13}^{+0.07}(\text{sys.})$	$0.74 \pm 0.35(\text{stat.})_{-0.21}^{+0.15}(\text{sys.})$

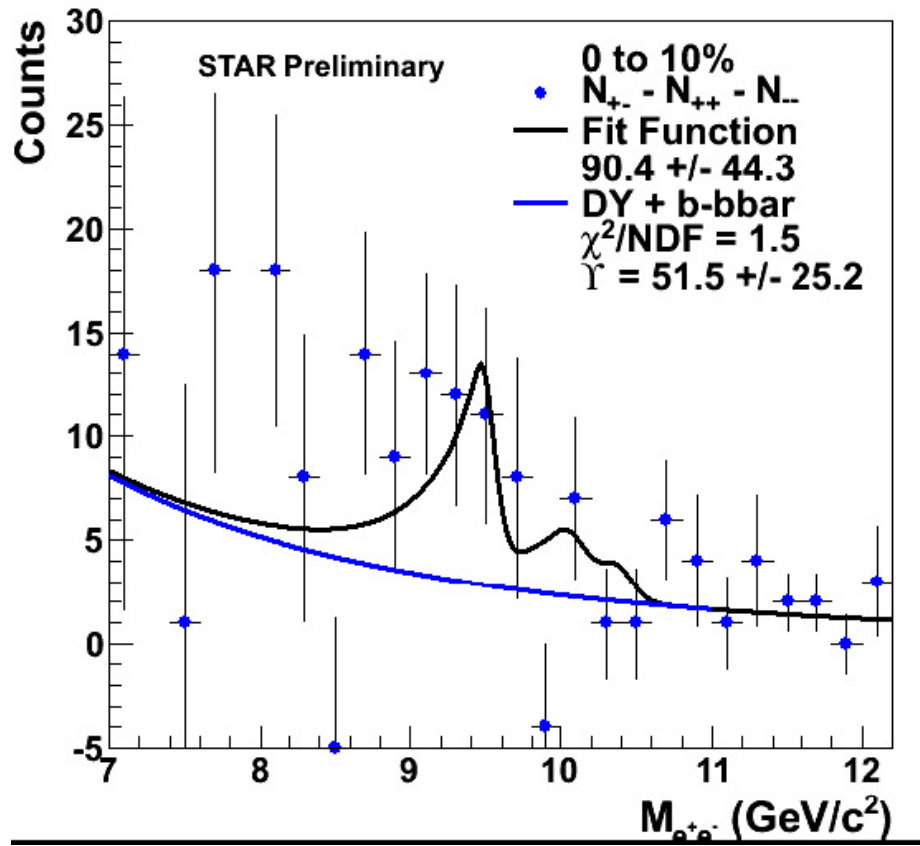


Figure 6.22. The unlike-sign subtracted di-electron spectrum for 0-10% central events is shown with the line-shape fit.

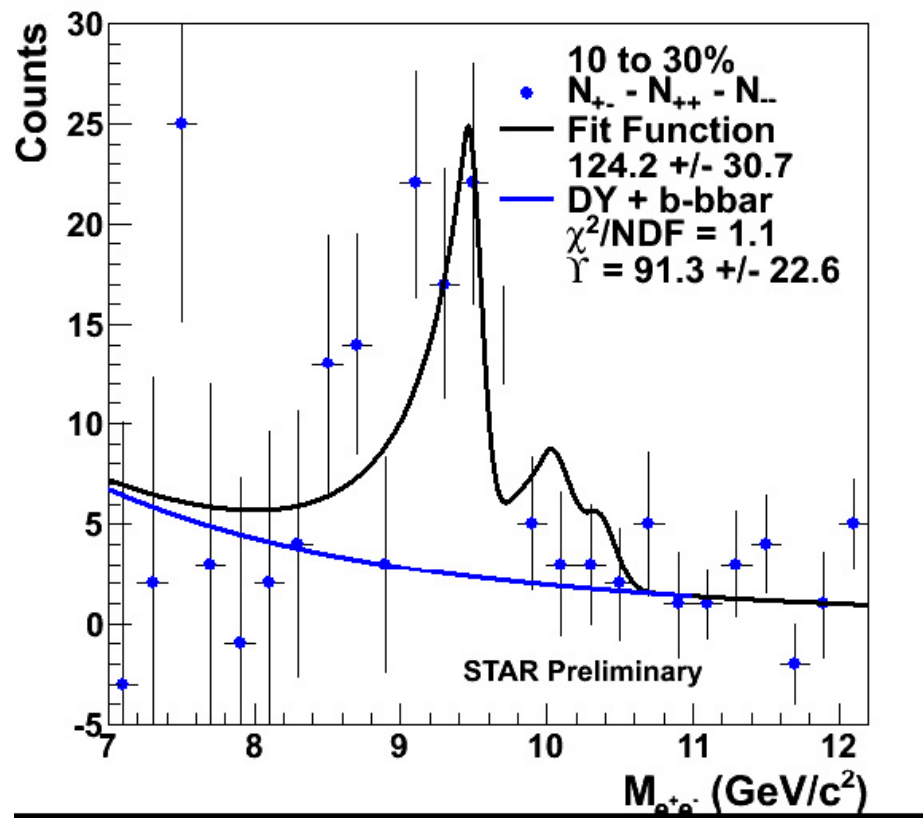


Figure 6.23. The unlike-sign subtracted di-electron spectrum for 10-30% central events is shown with the line-shape fit.

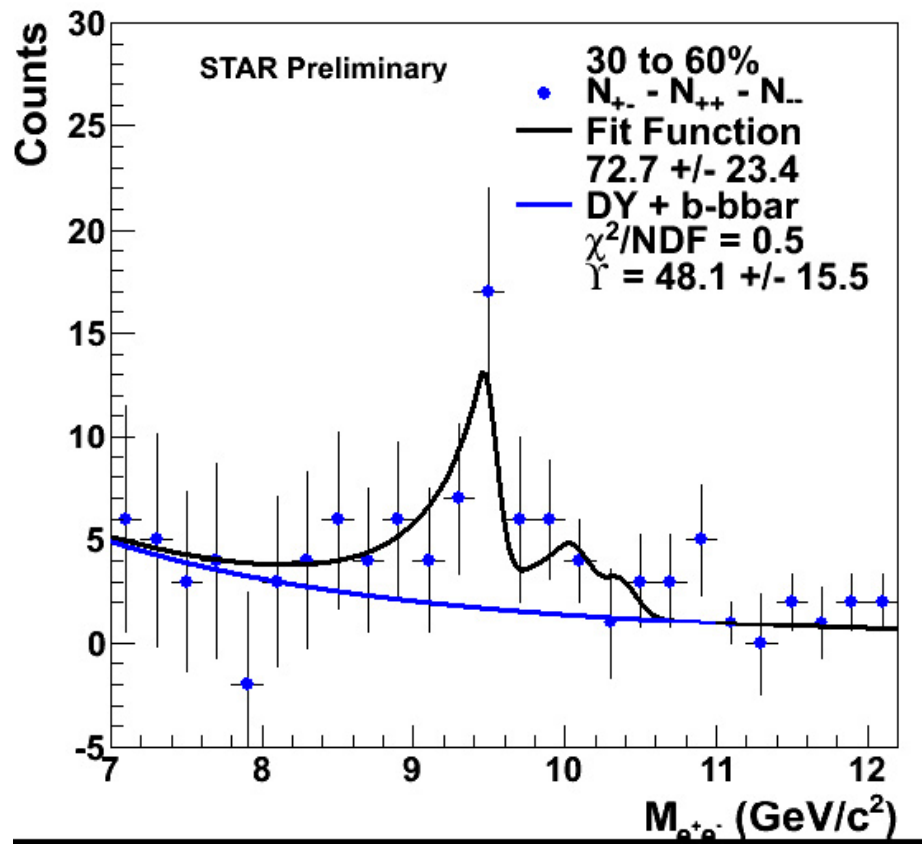


Figure 6.24. The unlike-sign subtracted di-electron spectrum for 30-60% central events is shown with the line-shape fit.

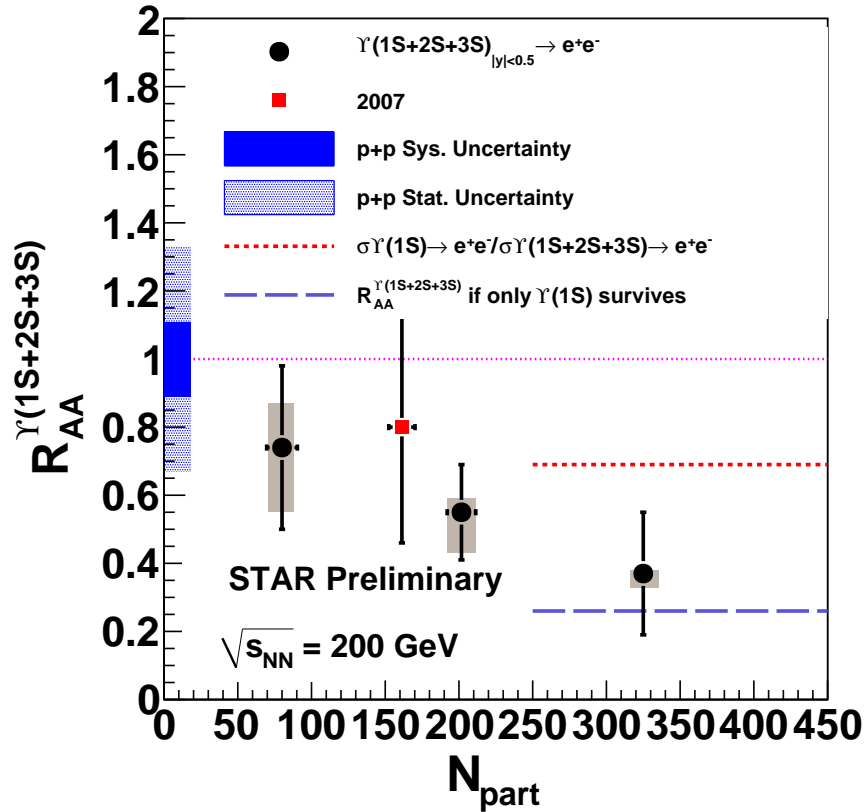


Figure 6.25. R_{AA} for $\Upsilon(1S + 2S + 3S)_{|y| < 0.5}$ versus centrality. The solid black points are the Υ results from Tabletab:RAA2010. The red solid square is the value for 0-60% centrality from Section 6.2. The solid blue box is the systematic uncertainty from the p+p cross-section, resulting from the uncertainty in the luminosity and the trigger efficiency. The grey boxes around the three Υ points are the systematic uncertainties of those points resulting from the uncertainty in N_{bin} and the $\Upsilon(1S + 2S + 3S)$ line-shape. The red dotted line is the ratio of the total cross-section of $\Upsilon(1S)/\Upsilon(1S + 2S + 3S)$. The purple dashed line is the ratio of only the direct $\Upsilon(1S)$ cross-section over the total $\Upsilon(1S + 2S + 3S)$ cross-section.

Chapter 7

Discussion

7.1 Experiment

More than 25 years after quarkonia suppression was suggested to be a signature of the QGP, we are now at the point where we can measure Υ suppression as well as J/ψ suppression, both at RHIC and at the LHC. Our results, shown in Figure 6.25, show that $R_{AA}^{\Upsilon(1S+2S+3S)}$ is suppressed. In the most central bin, R_{AA} is 3σ away from 1 after adding the $p+p$ statistical and systematic uncertainty in quadrature. However, the ratio of the direct $\Upsilon(1S)$ cross section over the $\Upsilon(1S+2S+3S)$ total cross section is 0.26 [92] and the ratio of the direct $\Upsilon(1S)$ cross section to the total is 0.50 [92] as measured by CDF at $\sqrt{s} = 1.96$ TeV. Even though this is tens times larger than \sqrt{s} at RHIC, it is already well above the production threshold for the various $b\bar{b}$ states. This means that using the CDF measurement to determine the ratio of the cross sections of the various $b\bar{b}$ states at RHIC is appropriate because while we expect the cross sections for all of them to increase as a function of \sqrt{s} , we do not expect the

Table 7.1. Quarkonium Dissociation Temperature relative to T_c [20].

State	$J/\psi(1S)$	$\chi_c(1P)$	ψ'	$\Upsilon(1S)$	$\chi_b(1P)$	$\Upsilon(2S)$	$\chi_b(2P)$	$\Upsilon(3S)$
T_d/T_c	2.10	1.16	1.12	> 4.0	1.76	1.60	1.19	1.17

ratio of their cross sections to change much. The ratio of the direct to the indirect production of the $\Upsilon < 1$ means is that measuring $R_{AA} \Upsilon(1S + 2S + 3S) < 1$ or even $R_{AA} \Upsilon(1S) < 1$ does not indicate that the $\Upsilon(1S)$ state is suppressed. It does indicate that the higher order $b\bar{b}$ states such as the $\Upsilon(3S)$ or the χ_b are suppressed. Many studies have calculated a dissociation temperature for the quarkonia states, such as those shown in Table 7.1 from Ref. [20]. In this section, we will compare our results to those measured by PHENIX and CMS.

However, we have to be careful when interpreting experimental data as sequential melting temperatures do not necessarily indicate sequential suppression. For example, an uncorrelated $b\bar{b}$ pair can become a $\Upsilon(1S)$ or $\Upsilon(2S)$ meson. In the past, the dissociation temperature has been listed as $X \times T_c$, it is best if we use real temperature units for the dissociation temperature because the meaning (and value) of T_c is ambiguous [93]. Recent theory studies suggest that none of the $b\bar{b}$ states would survive at a temperature greater than 450 MeV, and that the $c\bar{c}$ states would not survive above 250 MeV [93]. Further improvement on both the theory and experimental end may allow us to converge on a specific temperature for the matter produced at a particular $\sqrt{s_{NN}}$. As experimentalists, what we would like to see on the theory side is a model that includes the latest lattice-based complex potentials that include color screening, Landau damping and threshold enhancement. We want these models to have a realistic collision geometry, where there is a variation in energy density (temperature)

between the center and edge of the material and some sort of 3D time evolution. We would like the models to include quarkonium formation time effects, feed-down and realistic bottomonium spectra. We would like to see the model predictions of R_{AA} versus centrality, rapidity and p_T and include a lower limit on the integrated R_{AA} .

To further quantify our results versus centrality, we fit the results with two assumptions: a constant with respect to centrality and an equation that assumes a linear dependence on centrality. The fits can be seen in Figure 7.1. If we assume a constant dependence, we find that $R_{AA} \Upsilon(1S + 2S + 3S) = 0.52 \pm 0.1$ and if we assume a linear dependence, we find that $R_{AA} \Upsilon(1S + 2S + 3S) = (0.85 \pm 0.28) + (-0.0015 \pm 0.012) N_{part}$. However, both of them have reasonable χ^2/DOF , which indicates that we cannot make a definitive statement about the centrality dependence at this time.

One question to ask is whether a consistent picture is being formed. In Figure 7.2 the results from this thesis are compared to PHENIX results taken at the same $\sqrt{s_{NN}}$ and also at midrapidity. They are similar, however the exact quantity being measured is not identical in both cases. The PHENIX analysis does not try to separate the Drell-Yan or $b\bar{b}$ background from their result. We have measured that about 25% of the midrapidity dielectron yield in the mass region between 8 and 12 GeV/ c^2 is from the Drell-Yan and $b\bar{b}$ continuum [4]. Since the Drell-Yan continuum should not be modified by a colored medium, the inclusion of this could bias R_{AA} towards 1. The PHENIX results have a smaller rapidity range, though the difference between the two should be minimal. The centrality selection is also slightly different: 0-60% versus 0-100%. But this is also an extremely minimal effect as the vast majority of the heavy-ion Υ cross section comes from the most central collisions. Neither analysis has tried

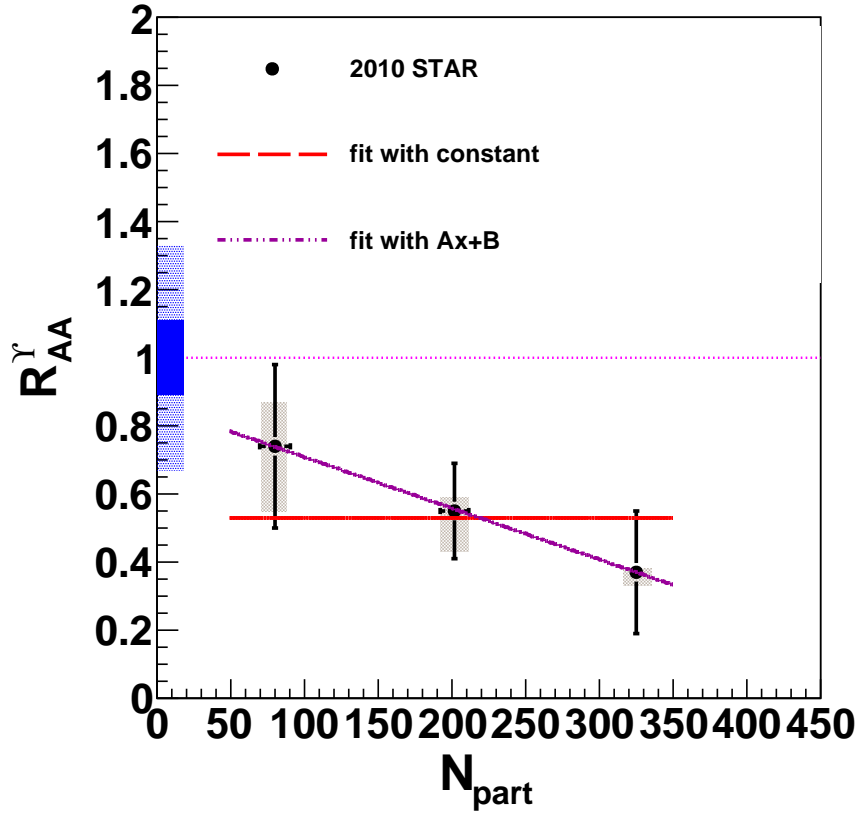


Figure 7.1. The points are from Figure 6.25. They are fit with a constant, in dashed red, and a linear function, in dotted purple.

to correct for feed-down or for CNM. PHENIX reports an R_{AA} less than 0.64 at 90% confidence level, compared to our 2010 result of $R_{AA} = 0.52 \pm 0.20(\text{stat.})_{-0.12}^{+0.07}(\text{sys.})$, which is equivalent to stating that we report that R_{AA} is less than 0.85 at 90% confidence.

The other heavy-ion Υ result we can compare to is the CMS result shown in Figure 7.3 [27]. This result was taken at $\sqrt{s_{NN}} = 2.76$ TeV, more than ten times the $\sqrt{s_{NN}}$ of RHIC. We do not necessarily expect the same result in both systems because several factors that make the systematics for Υ clean at RHIC are less easy to disentangle at CMS. For instance, if we look back at Figure 2.3, at CMS we are in

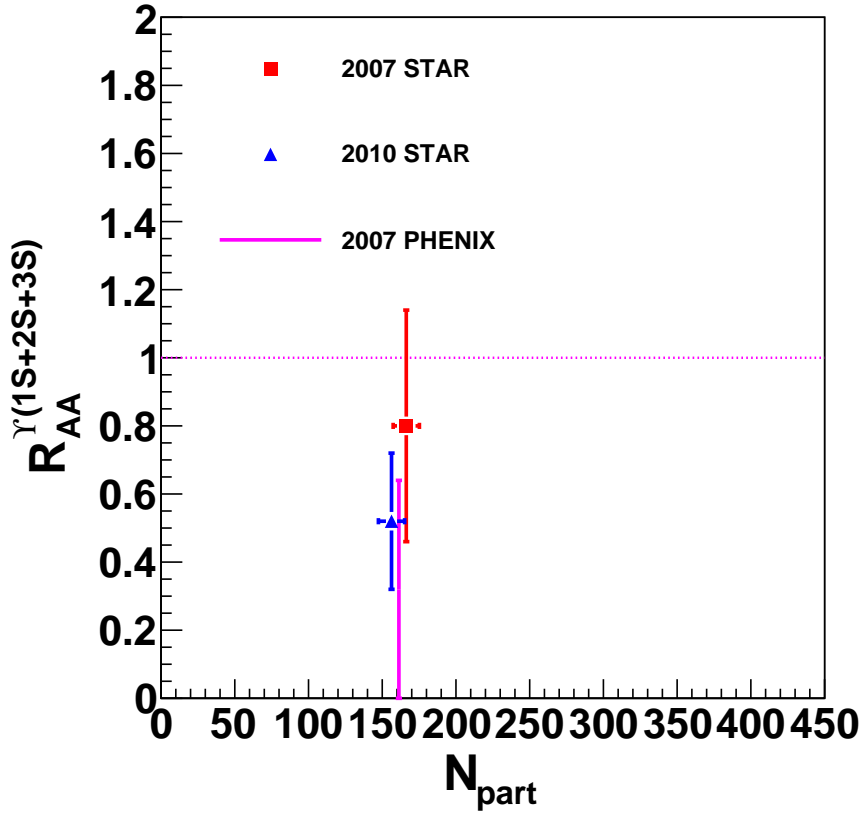


Figure 7.2. The red square is the 0-60% R_{AA} for $\Upsilon(1S + 2S + 3S)_{|y|<0.5} \rightarrow e^+e^-$ from the 2007 run, the blue triangle is the same point from the 2010 run. The purple line shows the 0-100% $R_{AA}^{\Upsilon(1S + 2S + 3S)+DY+b\bar{b}}$ for the $\Upsilon(1S + 2S + 3S)_{|y|<0.35} \rightarrow e^+e^-$ result from PHENIX run 2007 at 90% CL [26].

the shadowing region so one would expect some suppression just due to CNM. The CMS analysis is similar to the analysis in this thesis in that they do not attempt to correct for CNM by dividing R_{AA} by R_{pA} (or R_{dA}) as done by the SPS to show that the suppression of J/ψ in heavy ion collisions is “anomalous” [2].

Another factor is that recombination will be higher at the LHC than at RHIC for the Υ family as the $\sigma_{b\bar{b}}$ increases with energy. At $\sqrt{s_{NN}} = 200$ GeV the charm cross section is calculated as $256^{+400}_{-140} \mu b$ from a FONLL calculation and $284^{+381}_{-134} \mu b$ from a NLO calculation, and the bottomonium cross section is $1.87^{+0.99}_{-0.67} \mu b$ [32]. At the

Table 7.2. Branching ratios of the $\Upsilon(nS) \rightarrow e^+e^-$ [30] and the total cross sections from a NLO CEM model [32].

Υ State	BR (%)	$\sigma(\text{nb})$
$\Upsilon(1S)$	2.38 ± 0.11	6.60
$\Upsilon(2S)$	1.91 ± 0.16	2.18
$\Upsilon(3S)$	2.18 ± 0.21	1.32

LHC, the bottomonium cross section is calculated to increase to $\sim 50 \mu b$ at 2.76 TeV and $\sim 100 \mu b$ at the full heavy ion energy of 5.5 TeV [94]. So, while recombination of the $b\bar{b}$ states will have a larger effect at the LHC than at RHIC, this effect will be less than the recombination of the $c\bar{c}$ states at RHIC assuming that the only factor in this effect is the total heavy quark cross section.

The CMS result is for the inclusive $\Upsilon(1S)$ however the ratio of the $\Upsilon(1S)$ yield in the dilepton channel to the $\Upsilon(1S + 2S + 3S)$ in the dilepton channel is roughly 0.69, which means that $R_{AA} \Upsilon(1S + 2S + 3S)$ is dominated by the $\Upsilon(1S)$. The Υ branching ratio to electrons [30] and the cross sections from a NLO CEM calculation at $\sqrt{s} = 200$ GeV [32] are listed in Table 7.2. The branching ratio of $\Upsilon(nS) \rightarrow \mu^+\mu^-$ is very similar and there is no reason to expect that the ratios of the cross sections of the various Υ states will change with \sqrt{s} . CMS has also reported on a relative suppression of the $\Upsilon(2S + 3S)$ with respect to the $\Upsilon(1S)$ [95]. This relative suppression is: [95].

$$\frac{\Upsilon(2S + 3S)/\Upsilon(1S)[PbPb]}{\Upsilon(2S + 3S)/\Upsilon(1S)[pp]} = 0.31_{+0.19}^{-0.15} (\text{stat.}) \pm 0.03 (\text{sys.}) \quad (7.1)$$

This indicates that $R_{AA} \Upsilon(1S + 2S + 3S) \sim 0.69 \times R_{AA} \Upsilon(1S)$ at $\sqrt{s_{NN}} = 2.76$ TeV assuming that the $\Upsilon(2S)$ and $\Upsilon(3S)$ are completely suppressed ($R_{AA} = 0$). The

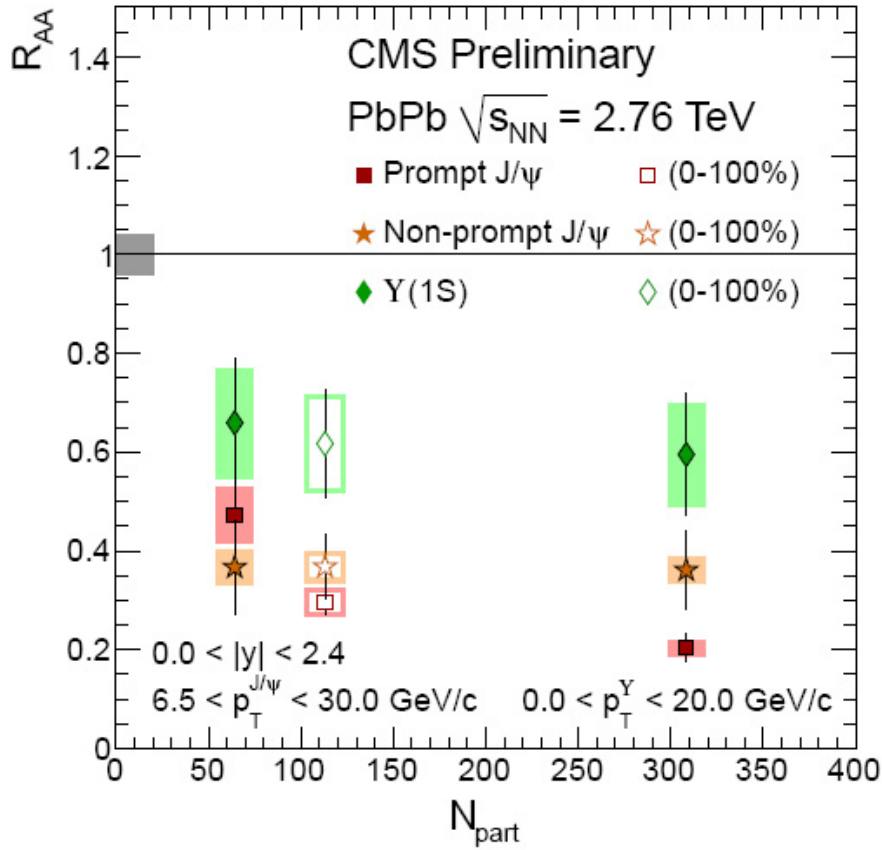


Figure 7.3. CMS R_{AA} results for inclusive $\Upsilon(1S)$ and the prompt and non-prompt J/ψ . The solid points are a subset of the open points [27]. The decay used to reconstruct them is $\Upsilon(J/\psi) \rightarrow \mu^+\mu^-$ and $|y_\Upsilon| < 2.4$.

kinematic regions of the Υ in STAR and CMS are different, which could result in different R_{AA} even if the medium effect on the $\Upsilon(1S + 2S + 3S)$ states is the same in both systems as we expect dependence on Υ_{p_T} and Υ_y . Suppression is calculated to be less at forward and backward rapidity and to decrease with increasing p_T [28]. The CMS results from Figure 7.3 are compared to the STAR results from Section 6.3 in Figure 7.4.

Experimentally, all these results are consistent within their large systematic and statistical uncertainties and more importantly indicate that we see suppression. We

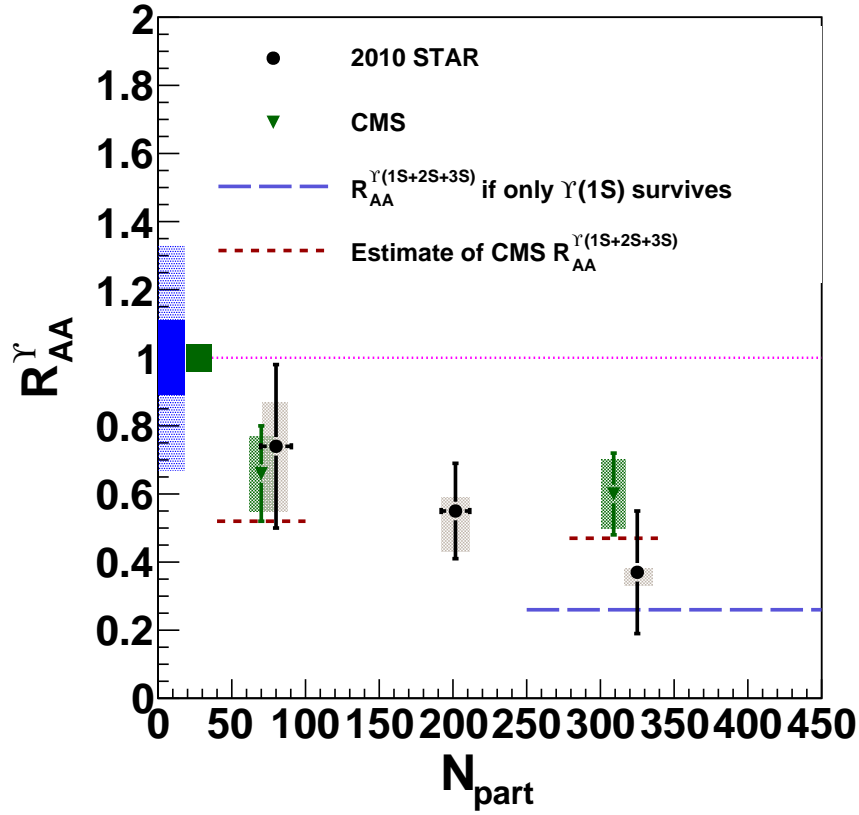


Figure 7.4. CMS R_{AA} results [27] in green triangles. The STAR results from 2010 are in black. The blue boxes are the $p + p$ normalization for the STAR point, the solid green box is the $p + p$ normalization for the CMS points. The red small dashed lines indicate an estimate for the CMS $R_{AA}^{\Upsilon(1S + 2S + 3S)}$ result given Equation 7.1. The large purple dashed line indicates an estimate for $R_{AA}^{\Upsilon(1S + 2S + 3S)}$ if only the $\Upsilon(1S)$ state survives, based on the relative cross sections of the direct and indirect Υ 's

cannot yet determine the dependence of R_{AA}^{Υ} versus $\sqrt{s_{NN}}$, centrality, p_T or y .

However, this should be the goal of Υ -based heavy ion studies in the next few years.

Another goal would be to quantify the CNM effects, so that we can determine how much of the measured R_{AA} is anomalous, if any. In order to do this, STAR has made a measurement of $R_{dA} = 0.78 \pm 0.28$ (stat.) ± 0.20 (sys) [96, 97]. The underlying baseline $p + p$ for this measurement is the same measurement discussed in Chapter

Table 7.3.

	0-60%	0-10%
R_{AA}	0.52 ± 0.09 (stat.) $^{+0.04}_{-0.10}$ (sys.)	0.37 ± 0.18 (stat.) $^{+0.01}_{-0.04}$ (sys.)
R_{AA}/R_{dA}	0.67 ± 0.13 (stat.) $^{+0.11}_{-0.16}$ (sys.)	0.47 ± 0.23 (stat.) $^{+0.07}_{-0.08}$ (sys.)
	10-30%	30-60%
R_{AA}	0.55 ± 0.14 (stat.) $^{+0.04}_{-0.12}$ (sys.)	0.74 ± 0.24 (stat.) $^{+0.13}_{-0.19}$ (sys.)
R_{AA}/R_{dA}	0.71 ± 0.19 (stat.) $^{+0.11}_{-0.18}$ (sys.)	0.95 ± 0.32 (stat.) $^{+0.21}_{-0.28}$ (sys.)

4. It is important to note that the d +Au analysis used the same topological trigger discussed in Section 5.1 with the same thresholds, but the SVT had been removed from inside STAR so this analysis was the first analysis with the reduced material budget. Another important thing to note is that the yield of the $\Upsilon(1S + 2S + 3S)$ in d +Au was determined by a simple counting method and thus contains some counts due to the Drell-Yan and $b\bar{b}$ background. The statistical and systematic uncertainty due to the d +Au analysis were 9% and 14%, respectively. If we assume that none of the systematic uncertainties in the d +Au analysis cancels with our Au+Au analysis, we can calculate as R_{AA}/R_{dA} shown in Table 7.3. In the most central bin, this ratio is $R_{AA} = 0.47 \pm 0.23$ (stat.) $^{+0.07}_{-0.08}$ (sys.), which still indicates suppression that cannot be accounted for by CNM effects. However, even though the uncertainty due to the $p + p$ analysis cancels out in this ratio, the uncertainties of the Au+Au and d +Au result added in quadrature indicate that this point is only 2.2σ away from $R_{AA} = 1$.

7.2 Theory

In order to understand what the measured values of R_{AA} mean, it is important to compare to theoretical predictions. One new development has been the extension of traditional viscous hydrodynamics cases where the local momentum-space anisotropy

of the plasma is large. This means that each individual hydrodynamic cell can have a pressure and/or spatial anisotropy [28]. This treatment is given the label ‘‘aHydro’’. A calculation for the $\Upsilon(1S)$ case at CMS with $\sqrt{s_{NN}} = 2.76$ TeV in the measured kinematic range is shown in Figure 7.5, with our $\Upsilon(1S + 2S + 3S)$ results. This calculation combined the aHydro treatment with a $\Upsilon(1S)$ binding potential with both a real and imaginary part. Since we expect the temperature to increase as a function of $\sqrt{s_{NN}}$, we would expect this prediction to give a lower value of R_{AA} than what would be measured at $\sqrt{s_{NN}} = 200$ GeV. Also, since we are measuring $\Upsilon(1S + 2S + 3S)$ at STAR rather than $\Upsilon(1S)$ and $R_{AA} \Upsilon(1S + 2S + 3S) < R_{AA} \Upsilon(1S)$, our result will be lower by about 50% ($R_{AA} \Upsilon(1S) \sim 0.5$ if all higher order states are suppressed with an R_{AA} of zero and $R_{AA} \Upsilon(1S + 2S + 3S)$ should be 0.26 under the same assumption) than if we measured the $\Upsilon(1S)$ state alone. However, since most models predict a dissociation temperature for the higher mass $b\bar{b}$ states on the order of T_c and that of the $\Upsilon(1S)$ as much higher, there should not be a huge difference between $R_{AA} \Upsilon(1S)$ at $\sqrt{s_{NN}} = 2.76$ TeV and 200 GeV. Which is what we see experimentally in Figure 7.4 where the red-dashed lines underneath the CMS points indicate our best estimate given their experimental results for what the CMS $R_{AA} \Upsilon(1S + 2S + 3S)$ measurement will be. Within the experimental uncertainty, we see that this assumption is true, which validates comparing to this particular model despite the difference in $\sqrt{s_{NN}}$.

The next theory comparison is from a transport model from Reference [29]. In this model, they solve the Schroedinger equation under both assumptions: $V=F$ and $V = U$, where F is the free energy and U is the internal energy. The question of which is

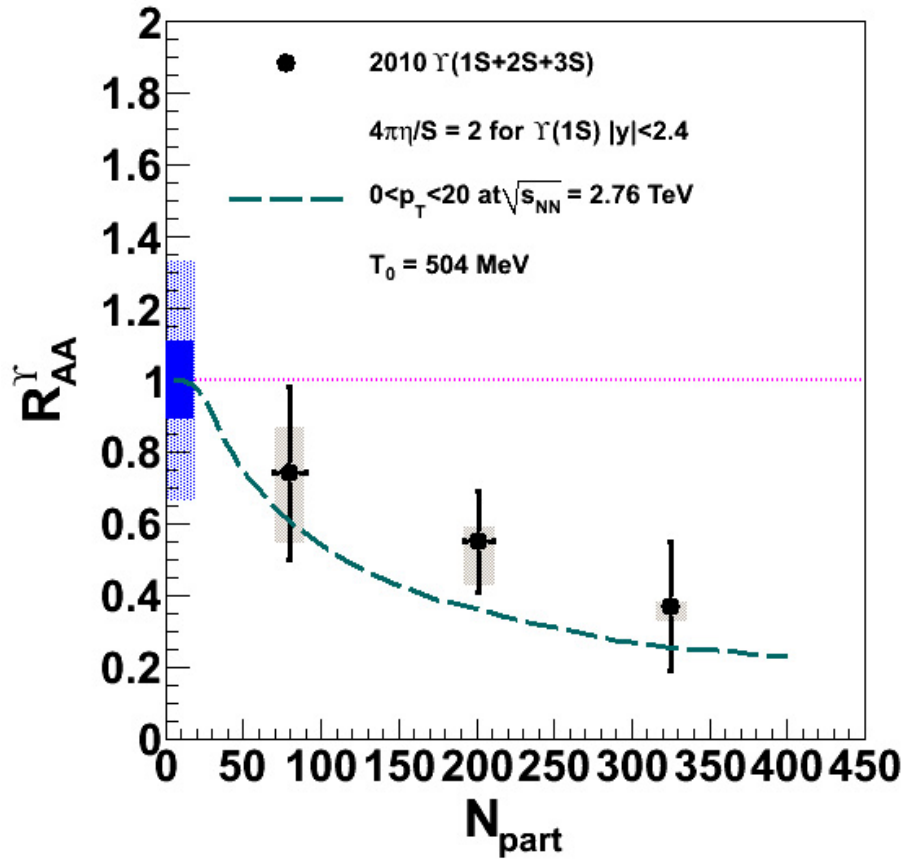


Figure 7.5. The blue dashed line is a calculation from [28] assuming a central temperature of $T_0 = 504$ MeV. The black points are our $\Upsilon(1S + 2S + 3S)$ analysis from 2010.

the proper energy to use is still open. The choice of whether the potential should be the free energy or the internal energy depends on the timescale for the dissociation of the $b\bar{b}$ pair. If the Υ dissociates quickly, it does not interact with the medium much before the dissociation and so the internal energy is an appropriate choice. If it dissociates slowly, the heavy quarks exchange energy with the medium and thus the free energy is more appropriate [29]. This particular model is of interest because their calculations were done assuming $\sqrt{s_{NN}} = 200$ GeV, unlike the previous comparison. They do not report on their kinematic variables, however they do take feed-down

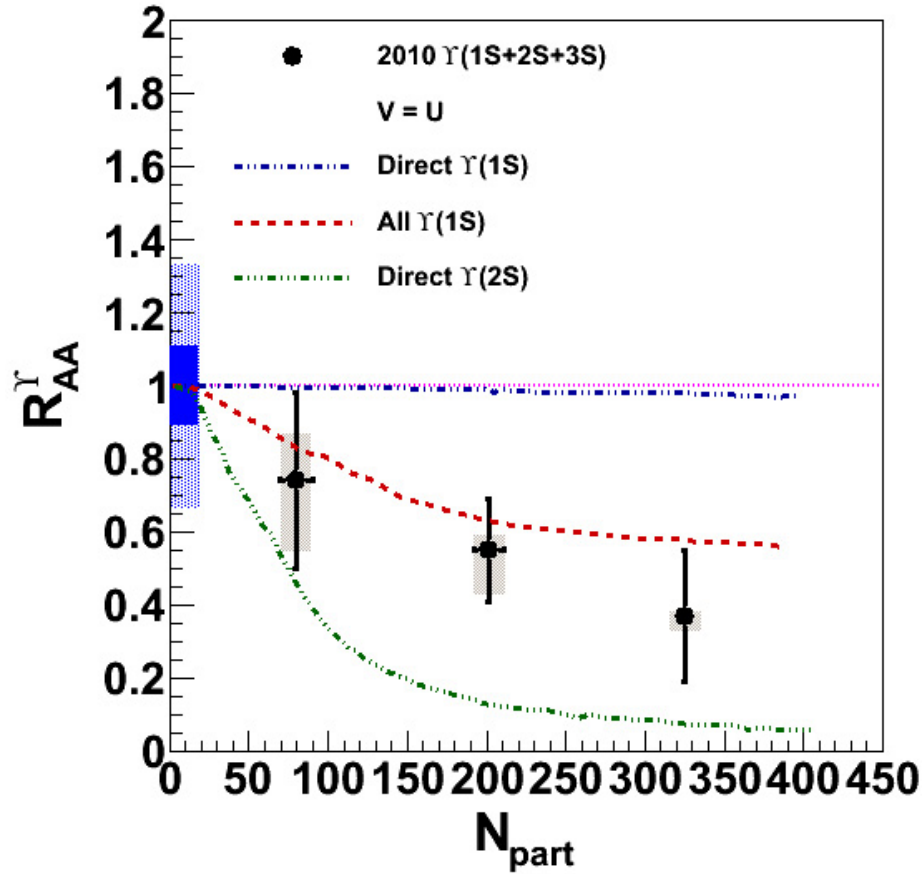


Figure 7.6. This is the case where the potential was set to the internal energy ($V = U$). The blue dot-dashed line is the calculation for the directly $\Upsilon(1S)$. The red dashed line is the R_{AA} for the total $\Upsilon(1S)$. And the green dot-dashed line is the R_{AA} for the direct $\Upsilon(2S)$ [29]. Our 2010 points are in black.

into account in their calculations. Since nearly 50% of the $\Upsilon(1S)$ state comes from the decay of higher order states [92], this is a very important consideration. They do make the simplification that there is no difference between the $\Upsilon(2S)$ and $\Upsilon(3S)$ states, which given dissociation temperatures for these two states are similar in other calculations, this assumption seems reasonable. Comparison of our data to their calculation of $V = U$ can be seen in Figure 7.6 and $V = F$ can be seen in Figure 7.7. The two calculations have very different shapes at low N_{part} so it may be possible to distinguish between the two given better statistics. This calculation does not

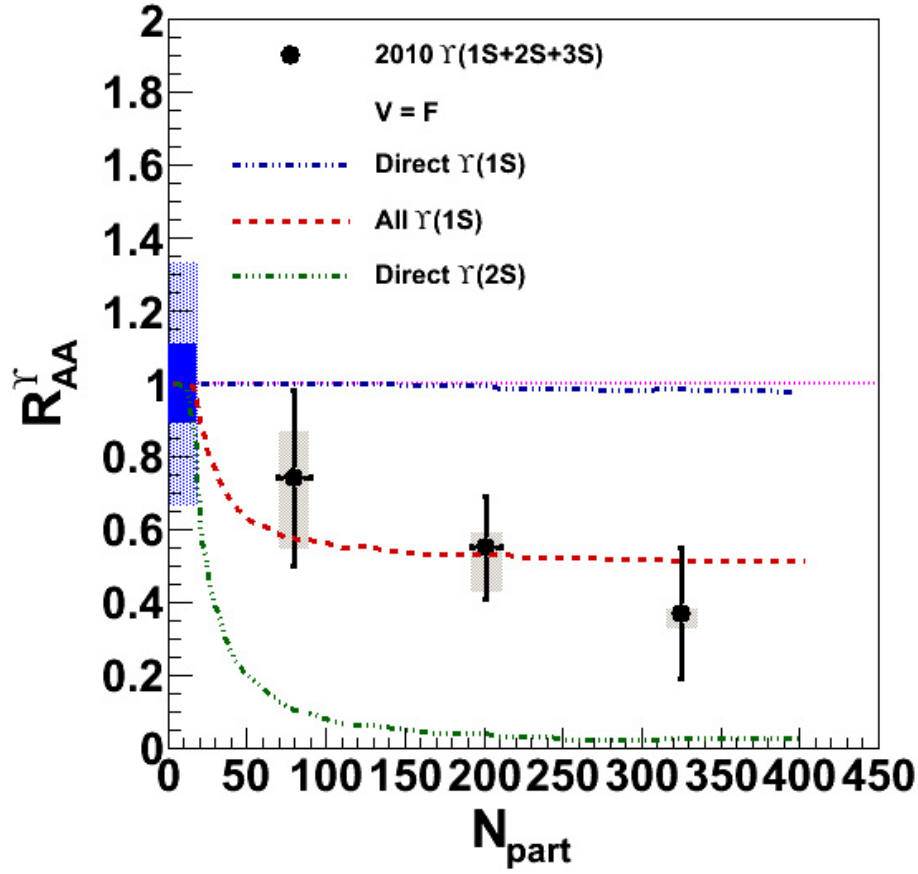


Figure 7.7. This is the case where the potential was set to the Free energy ($V = F$). The blue dot-dashed line is the calculation for the directly $\Upsilon(1S)$. The red dashed line is the R_{AA} for the total $\Upsilon(1S)$. And the green dot-dashed line is the R_{AA} for the direct $\Upsilon(2S)$ [29]. Our 2010 points are in black.

take the collision geometry into consideration. Υ mesons that are created near the surface of the QGP fireball should have a much higher probability of surviving simply because they may not interact much with the medium. This is one of the reasons that we do not see $R_{AA} \sim 0$ for any hadron, even the light hadrons with relatively low binding energies. This is an important macroscopic effect that it will be necessary to disentangle in order to better interpret our R_{AA} measurements. Unfortunately there is no systematic uncertainty on this particular calculation, though in some respects one can take the calculations with the two different potential choices as systematics.

What have we learned in the last few years? We can say that we definitely see some Υ suppression in the most central collisions. However, what we see is consistent with a picture where the $\Upsilon(1S)$ state is not suppressed, but where some of the higher order states are suppressed. This is what was expected from models based on lattice QCD calculations which assert that quarks are deconfined in a high-temperature colored medium. Models of Υ suppression by hadronic comovers show that this effect is negligible [3], which helps to lower the systematics of the Υ measurement. The Υ suppression story is very similar across STAR, PHENIX and even CMS with an $\Upsilon(1S + 2S + 3S)$ R_{AA} of ~ 0.5 . If we return to the idea that quarkonia suppression due to Debye Screening is an unambiguous signal of the QGP, we have not yet adequately controlled all pieces of the puzzle and so this probe cannot be used to state this conclusively. However, current models, which assert quark deconfinement at their heart, and our data are in good agreement, with the caveat that the uncertainties in both are large and so both further measurements and further model refinements are necessary. However, we cannot rule out models predicting suppression due to color deconfinement. The amount of suppression we see at RHIC is larger than what can be explained by CNM effects, as we can see in our ratio of R_{AA}/R_{dA} . Further measurements to better look at the relative suppression of the Υ family could allow us to make a model dependent measurement of the temperature formed in the collisions at RHIC and at the LHC.

Chapter 8

Conclusion

8.1 Υ cross-section

We measured the $\Upsilon(1S+2S+3S) \rightarrow e^+e^-$ cross section at midrapidity, $|y_{ee}| < 0.5$, in $p+p$ collisions at $\sqrt{s} = 200$ GeV to be $(\mathcal{B} \times d\sigma/dy)^{1S+2S+3S} = 114 \pm 38$ (stat. + fit) $^{+23}_{-24}$ (syst.) pb. Calculations done in the Color Evaporation Model at NLO are in agreement with our measured cross section. Calculations in the Color Singlet Model underestimate our cross section by $\approx 2\sigma$. Our result is consistent with the trend as a function of \sqrt{s} based on data from other experiments. We report a combined continuum cross section of the Drell-Yan plus $b\bar{b} \rightarrow e^+e^-$, measured in the kinematic range $|y_{ee}| < 0.5$ and $8 < m_{ee} < 11$ GeV/ c^2 , of $(\sigma_{\text{DY}} + \sigma_{b\bar{b}}) = 38 \pm 24$ pb. This STAR measurement was used as a baseline for studying cold nuclear matter effects in $d+\text{Au}$ collisions. It was also used as a base line for the study of hot nuclear matter effects in $\text{Au}+\text{Au}$ collisions discussed in the latter part of this thesis. With the increased luminosity expected in latter runs, a better determination of the cross

section, its p_T dependence and a separation of the 2S and 3S states will be possible. The projected luminosity upgrades to RHIC should increase the Υ yield to ≈ 8300 in $p + p$ and ≈ 11200 in Au+Au collisions during one RHIC year [32]. The increased statistics will greatly reduce the uncertainty in the determination of the continuum cross section and will allow a thorough study of the bottomonium sector by resolving the 2S and 3S states. It will also help us determine a differential R_{AA} .

8.2 ΥR_{AA}

We measured the $\Upsilon(1S+2S+3S) \rightarrow e^+e^-$ cross section at midrapidity, $|y_{ee}| < 0.5$ yield in Au+Au collisions at $\sqrt{s_{NN}} = 200$ GeV from 9.4×10^8 minimum-bias triggers from 2007 and 6.85×10^9 minimum-bias triggers. For both runs we calculated the R_{AA} in 0-60% centrality to be 0.80 ± 0.34 (stat.) and 0.52 ± 0.20 (stat.) $^{0.07}_{-0.12}$ (sys.) including the uncertainty in the $p + p$ analysis. These measurements are in agreement, despite the changes to the detector geometry and the trigger. In 0-10% centrality, R_{AA} is 0.37 ± 0.22 (stat.) $^{0.04}_{-0.12}$ (sys.), a full 3σ away from $R_{AA} = 1$ indicating $\Upsilon(1S + 2S + 3S)$ suppression in the most central collisions. The ratio of R_{AA}/R_{dA} in 0-10% centrality is 0.47 ± 0.23 (stat.) $^{0.07}_{-0.08}$ (sys.) which is only 2σ away from 1. There is evidence for anomalous suppression of $\Upsilon(1S + 2S + 3S)$ at $\sqrt{s_{NN}} = 200$ GeV.

Bibliography

- [1] T. Matsui and H. Satz, *Physics Letters B* **178**, 416 (1986).
- [2] NA50, M. C. Abreu *et al.*, *Phys. Lett.* **B477**, 28 (2000).
- [3] Z. Lin and C. Ko, *Physics Letters B* **503**, 104 (2001).
- [4] STAR Collaboration, B. I. Abelev *et al.*, *Phys. Rev. D* **82**, 012004 (2010).
- [5] http://en.wikipedia.org/wiki/File:Standard_Model_of_Elementary_Particles.svg
.
- [6] S. Bethke, *Eur. Phys. J.* **C64**, 689 (2009), [0908.1135].
- [7] O. Kaczmarek and F. Zantow, *Phys. Rev. D* **71**, 114510 (2005).
- [8] STAR, M. M. Aggarwal *et al.*, 1007.2613.
- [9] F. Karsch, *Nucl. Phys.* **A698**, 199 (2002), [hep-ph/0103314].
- [10] P. Huovinen, P. Kolb, U. Heinz, P. Ruuskanen and S. Voloshin, *Physics Letters B* **503**, 58 (2001).
- [11] P. Braun-Munzinger, K. Redlich and J. Stachel, nucl-th/0304013.
- [12] R. Snellings, *New Journal of Physics* **13**, 055008 (2011), [1102.3010].
- [13] PHENIX Collaboration, S. S. Adler *et al.*, *Phys. Rev. C* **75**, 024909 (2007).
- [14] STAR, J. Adams *et al.*, *Nucl. Phys.* **A757**, 102 (2005), [nucl-ex/0501009].
- [15] PHENIX Collaboration, A. e. a. Adare, *Phys. Rev. Lett.* **98**, 172301 (2007).
- [16] S. J. Brodsky and J.-P. Lansberg, *Phys. Rev. D* **81**, 051502 (2010).
- [17] P. Artoisenet, J. M. Campbell, J. P. Lansberg, F. Maltoni and F. Tramontano, *Phys. Rev. Lett.* **101**, 152001 (2008), [0806.3282].
- [18] N. Brambilla *et al.*, *Eur. Phys. J.* **C71**, 1534 (2011), [1010.5827].
- [19] P. Petreczky, C. Miao and A. Mocsy, *Nuclear Physics A* **855**, 125 (2011),
Proceedings of the 4th International Conference on Hard and Electromagnetic
Probes of High-Energy Nuclear Collisions - HP2010.

- [20] L. Kluberg and H. Satz, 0901.3831.
- [21] J. P. Lansberg, International Journal of Modern Physics A **21**, 3857 (2006).
- [22] STAR Collaboration, J. S. C. C. A. Whitten, AIP Conference Proceedings **980**, 390 (2008).
- [23] M. Beddo *et al.*, Nuclear Instruments and Methods in Physics Research Section A: Accelerators, Spectrometers, Detectors and Associated Equipment **499**, 725 (2003), The Relativistic Heavy Ion Collider Project: RHIC and its Detectors.
- [24] M. Anderson *et al.*, Nuclear Instruments and Methods in Physics Research Section A: Accelerators, Spectrometers, Detectors and Associated Equipment **499**, 659 (2003), The Relativistic Heavy Ion Collider Project: RHIC and its Detectors.
- [25] R. Vogt, Calculations vs sqrt(s) in [32], calculations vs rapidity and for Drell-Yan shown in RHIC-II Science Workshop, 2005 <http://rhic-science.bnl.gov/heavy/doc/April05Meeting/> .
- [26] E. T. Atomssa, Nuclear Physics A **830**, 331c (2009), Quark Matter 2009 - The 21st International Conference on Ultrarelativistic Nucleus-Nucleus Collisions.
- [27] B. W. f. t. C. collaboration, arXiv 1107.2895, * Temporary entry *.
- [28] M. Strickland, 1106.2571. 1106.2571
- [29] Y. Liu, B. Chen, N. Xu and P. Zhuang, Phys.Lett. **B697**, 32 (2011), [1009.2585].
- [30] C. Amsler *et al.*, Physics Letters B **667**, 1 (2008), Review of Particle Physics.
- [31] A. Martin, R. Roberts, W. Stirling and R. Thorne, The European Physical Journal C - Particles and Fields **4**, 463 (1998), 10.1007/s100529800904.
- [32] A. D. Frawley, T. Ullrich and R. Vogt, Phys. Rept. **462**, 125 (2008), [0806.1013].
- [33] J. C. Maxwell, (1873).
- [34] S. Weinberg, Phys. Rev. Lett. **19**, 1264 (1967).
- [35] S. L. Glashow, Nuclear Physics **22**, 579 (1961).
- [36] A. Salam and J. C. Ward, Physics Letters **13**, 168 (1964).
- [37] M. Gellmann, Physics Letters **8**, 214 (1964).
- [38] V. E. Barnes *et al.*, Phys. Rev. Lett. **12**, 204 (1964).
- [39] S. L. Glashow, J. Iliopoulos and L. Maiani, Phys. Rev. D **2**, 1285 (1970).
- [40] J. E. Augustin *et al.*, Phys. Rev. Lett. **33**, 1406 (1974).

- [41] M. Kobayashi and T. Maskawa, Progress of Theoretical Physics **49**, 652 (1973).
- [42] S. W. Herb *et al.*, Phys. Rev. Lett. **39**, 252 (1977).
- [43] CDF Collaboration, F. e. a. Abe, Phys. Rev. Lett. **74**, 2626 (1995).
- [44] D0, S. Abachi *et al.*, Phys. Rev. Lett. **74**, 2422 (1995), [hep-ex/9411001].
- [45] D. J. Gross and F. Wilczek, Phys. Rev. Lett. **30**, 1343 (1973).
- [46] E. D. Bloom *et al.*, Phys. Rev. Lett. **23**, 930 (1969).
- [47] J. Adams *et al.*, Nuclear Physics A **757**, 102 (2005), First Three Years of Operation of RHIC.
- [48] C. R. Allton *et al.*, Phys. Rev. D **66**, 074507 (2002).
- [49] Z. Fodor and S. D. Katz, ArXiv e-prints (2009), [0908.3341].
- [50] P. Braun-Munzinger and J. Stachel, 1101.3167.
- [51] T. DeGrand, R. L. Jaffe, K. Johnson and J. Kiskis, Phys. Rev. D **12**, 2060 (1975).
- [52] P. Braun-Munzinger, I. Heppe and J. Stachel, Physics Letters B **465**, 15 (1999).
- [53] D. Molnár and S. A. Voloshin, Phys. Rev. Lett. **91**, 092301 (2003).
- [54] S. Salur, Nuclear Physics A **830**, 139c (2009), Quark Matter 2009 - The 21st International Conference on Ultrarelativistic Nucleus-Nucleus Collisions.
- [55] STAR Collaboration, C. Adler *et al.*, Phys. Rev. Lett. **90**, 082302 (2003).
- [56] S. Salur, 0910.2081.
- [57] W.-M. Yao *et al.*, Journal of Physics G **33**, 1+ (2006).
- [58] Y. Zhang, 1106.6078.
- [59] Y. L. Dokshitzer, V. A. Khoze and S. I. Troian, J. Phys. **G17**, 1481 (1991).
- [60] Y. L. Dokshitzer and D. E. Kharzeev, Physics Letters B **519**, 199 (2001).
- [61] S. Digal, P. Petreczky and H. Satz, Phys. Rev. D **64**, 094015 (2001).
- [62] R. Gavai *et al.*, Int. J. Mod. Phys. **A10**, 3043 (1995), [hep-ph/9502270].
- [63] Y. Burnier, M. Laine and M. Vepsinen, Journal of High Energy Physics **2008**, 043 (2008).
- [64] R. Vogt and S. Gavin, Nuclear Physics A **525**, 693 (1991).

- [65] M. Harrison, T. Ludlam and S. Ozaki, Nuclear Instruments and Methods in Physics Research Section A: Accelerators, Spectrometers, Detectors and Associated Equipment **499**, 235 (2003), The Relativistic Heavy Ion Collider Project: RHIC and its Detectors.
- [66] D. Das, The European Physical Journal C - Particles and Fields **62**, 95 (2009), 10.1140/epjc/s10052-009-0937-y.
- [67] R. Reed and the STAR Collaboration, Journal of Physics G: Nuclear and Particle Physics **37**, 94052 (2010).
- [68] R. Reed, Nuclear Physics A **855**, 440 (2011), Proceedings of the 4th International Conference on Hard and Electromagnetic Probes of High-Energy Nuclear Collisions - HP2010.
- [69] W. Llope, Nuclear Instruments and Methods in Physics Research Section B: Beam Interactions with Materials and Atoms **241**, 306 (2005), The Application of Accelerators in Research and Industry - Proceedings of the Eighteenth International Conference on the Application of Accelerators in Research and Industry (CAARI 2004).
- [70] STAR, J. Kiryluk, hep-ex/0501072.
- [71] STAR Collaboration, J. Adams *et al.*, Phys. Rev. Lett. **91**, 172302 (2003).
- [72] STAR, A. Rose, nucl-ex/0307015.
- [73] R. Reed *et al.*, Journal of Physics: Conference Series **219**, 032020 (2010).
- [74] F. S. Bieser *et al.*, Nuclear Instruments and Methods in Physics Research Section A: Accelerators, Spectrometers, Detectors and Associated Equipment **499**, 766 (2003), The Relativistic Heavy Ion Collider Project: RHIC and its Detectors.
- [75] (CDF Collaboration), D. Acosta *et al.*, Phys. Rev. Lett. **88**, 161802 (2002).
- [76] T. Sjostrand, 0809.0303.
- [77] CDF, R. Field and R. C. Group, hep-ph/0510198.
- [78] G. Moreno *et al.*, Phys. Rev. D **43**, 2815 (1991).
- [79] F. Jin and for the STAR Collaboration, Journal of Physics G: Nuclear and Particle Physics **36**, 064051 (2009).
- [80] M. L. Miller, K. Reygers, S. J. Sanders and P. Steinberg, Ann. Rev. Nucl. Part. Sci. **57**, 205 (2007), [nucl-ex/0701025].
- [81] R. Vogt, Heavy Ion Phys. **9**, 339 (1999), [nucl-th/9903051].
- [82] CMS Collaboration, S. e. a. Chatrchyan, Phys. Rev. Lett. **106**, 212301 (2011).

- [83] J. Robles, Ph. D. thesis, UC Davis, in preparation. .
- [84] STAR, W. Xu, 1106.6020.
- [85] and M. Abreu et al., The European Physical Journal C - Particles and Fields **14**, 443 (2000), 10.1007/s100520000373.
- [86] J. Gaiser, Ph.D. thesis, Stanford University [Report No. SLAC-R-255, Appendix F, p. 178] .
- [87] K. Ueno *et al.*, Phys. Rev. Lett. **42**, 486 (1979).
- [88] J. K. Yoh *et al.*, Phys. Rev. Lett. **41**, 684 (1978).
- [89] S. Childress *et al.*, Phys. Rev. Lett. **55**, 1962 (1985).
- [90] T. Yoshida *et al.*, Phys. Rev. D **39**, 3516 (1989).
- [91] C. Kourkouvelis *et al.*, Physics Letters B **91**, 481 (1980).
- [92] (CDF Collaboration), T. Affolder *et al.*, Phys. Rev. Lett. **84**, 2094 (2000).
- [93] A. Mocsy.
- [94] E. L. Berger and R. Meng, hep-ph/9308372.
- [95] CMS Collaboration, S. e. a. Chatrchyan, Phys. Rev. Lett. **107**, 052302 (2011).
- [96] R. Reed and the STAR Collaboration, Journal of Physics G: Nuclear and Particle Physics **37**, 094052 (2010).
- [97] H. Liu, Nuclear Physics A **830**, 235c (2009), Quark Matter 2009 - The 21st International Conference on Ultrarelativistic Nucleus-Nucleus Collisions.